SAAO
South African Astronomical Observatory

Developing Instrumentation and Software for Rapid Follow-up and Characterisation of near-Earth Asteroids

South African Astronomical Observatory
Cape Town
South Africa

Thesis presented for the fulfilment of the requirements for the degree of

Master of Science (MSc) in Astronomy

Department of Astronomy

University of Cape Town

Author:
Thobekile Sandra Ngwane

Student Number:
NGWTHO012

Supervisors:
Dr. Nicolas Erasmus and Professor Paul Groot

April 22, 2025

Abstract

Near-Earth Asteroids (NEAs), a subset of minor bodies in the Solar System, result from resonant interactions with major planets, particularly Jupiter, leading to their escape from the main asteroid belt. The International Astronomical Union's Minor Planet Center(MPC)[1] database, as of December 2024, lists approximately 37,000 discovered NEAs, with an average daily discovery rate of 10 from dedicated survey programs like Catalina Sky Survey (CSS), the Panoramic Survey Telescope and Rapid Response System (PanSTARRS), and the Asteroid Terrestrial-impact Last Alert System (ATLAS).

This project uses the robotic observing capabilities of the South African Astronomical Observatory's 1-meter telescope, Lesedi, equipped with the Mookodi instrument. Observations are scheduled in robotic mode using automated Python scripts, enabling rapid follow-up of newly discovered NEAs, often within the same night of detection. This rapid response is essential, as smaller asteroids (< 300 metres)—a significantly understudied group— quickly dim as they move away from Earth, making precise measurements challenging. Since the start of this project in February 2023, approximately 230 Near-Earth Asteroids (NEAs) have been successfully observed in robotic mode, with an average absolute magnitude (H-magnitude) of 24.4. This magnitude corresponds to asteroid sizes ranging from 32 to 78 metres, depending on an assumed albedo of 0.05 to 0.30. Approximately 75% of these asteroids have a diameter (D) of less than 100 metres. Among the observed NEAs, 15 have been classified as potentially hazardous asteroids (PHAs).

The findings presented in this study are based on multi-filter photometry and astrometric measurements collected as part of the program. The astrometric data significantly contributes to the Minor Planet Center's (MPC) orbital refinement and the observed Near-Earth Asteroids (NEAs) designation. Photometric observations using g, r, and i filters enable the extraction of $g - r$ and $r - i$ colours, which approximate the spectral slope. These colours aid in determining the most likely taxonomic type (S, C, X, D, Q, or V-types in this project) of the observed NEAs, as defined by the Bus-DeMeo Classification Scheme. This provides insight into their composition. Using the collected data, the compositional distribution of the small NEA population was determined and compared with previous studies investigating a larger size population.

[1] `https://www.minorplanetcenter.net/`

Acknowledgements

This MSc project was made possible through the generous support of the MasterCard Foundation Scholars Program at the University of Cape Town (UCT). Their commitment to empowering young researchers from Africa through education and mentorship has not only facilitated this academic journey but has also been instrumental in shaping my development as a researcher and leader. The resources, opportunities, and encouragement provided by the program have allowed me to pursue my passion for astronomy.

To my supervisors, Dr. Nicolas Erasmus and Professor Paul Groot, I am immensely grateful for the opportunity to work on this project that started as a hobby in my undergraduate days. Your guidance, insights, and encouragement throughout this journey have been invaluable, and I appreciate the time and effort you dedicated to my growth as a researcher.

I would also like to thank the South African Astronomical Observatory (SAAO) staff for their kindness, and support, making me feel at home during my time there. Your willingness to assist and share your expertise has enriched my experience in countless ways.

To the UCT Astronomy Department, thank you for fostering an intellectually stimulating environment and for your support throughout this journey. A special thanks to my fellow students at UCT and SAAO—your camaraderie, coffee runs, and engaging conversations have made this experience all the more enjoyable.

Above all, I am deeply grateful to God for His guidance, strength, and blessings throughout this journey.

Lastly, my deepest appreciation goes to my family for their unwavering love, encouragement, and belief in me. Your constant support has been my anchor, and I am forever grateful.

Plagiarism Declaration

I affirm that I understand the nature of plagiarism and declare that this dissertation represents my own ideas, words, and work. All sources used or referenced have been properly acknowledged and cited.

Thobekile Ngwane

February 2025

Contents

Introduction

Asteroids are a type of minor planet - rocky, metallic, or carbonaceous bodies with no atmosphere that orbit the Sun like planets. They are mainly found in the main asteroid belt found between Mars and Jupiter. Asteroids vary significantly in size, composition, and shape, with diameters ranging from a few metres to hundreds of kilometres (Bottke et al. 2005). There are billions of small asteroids in the belt in addition to an estimated 1.1 to 1.9 million larger asteroids with a diameter of more than 1km, (Mainzer et al. 2011). The Main Belt is thought to have originated in the early Solar System during its formation about 4.6 billion years ago (Morbidelli et al. 2009). The asteroid belt initially contained enough material to form a planet, but the gravitational influence of Jupiter prevented this material from merging into a larger body and also caused much of it to be ejected from the region during the Solar System's evolution. Instead, the material remained as numerous smaller bodies, resulting in the asteroid belt we observe today (Minton and Malhotra 2009). These asteroids are therefore remnants from the early Solar System, and studying them can provide clues to the early history of our Solar System's evolution.

Near-Earth Asteroids (NEAs) are a class of minor planets in our Solar System that have escaped from the main asteroid belt due to resonance interactions with major planets like Jupiter (Morbidelli et al. 2002, Smith 2020). As of this writing, the Minor Planet Center (MPC)[2] database, maintained by the International Astronomical Union (IAU), contains records of approximately 37,000 known NEAs that have been discovered so far. On average, 10 new NEAs are discovered daily[3], primarily through specialized asteroid discovery survey programs such as the Catalina Sky Survey (CSS; Larson et al. 1998), the Panoramic Survey Telescope and Rapid Response System (Pan-STARRS; Chambers et al. 2016), and the Asteroid Terrestrial-impact Last Alert System (ATLAS; Tonry et al. 2018). Given that NEAs have orbits that may cross Earth's path, future impacts are inevitable. While Impacts by small (<10 m) NEAs are relatively harmless, a subset known as 'Potentially Hazardous Asteroids' (PHAs) - those exceeding 140 metres in diameter and passing within 0.05 au of Earth's orbit – pose significant impact threats. Those in between that are large enough can cause significant localised damage, but are not necessarily classified as PHAs. Without detection and intervention measures, the eventual impact of a PHA is statistically inevitable.

Recent studies have shown that comet and asteroid collisions are responsible for at least 210 verified impact craters on Earth, (Kenkmann and Artemieva 2021, James et al. 2022) and therefore the NEA population is particularly interesting to investigate further. Additionally, it is estimated that, on average, one meteoroid (another name for a very small asteroid) ranging in size from three to four metres explodes in Earth's atmosphere each

[2] https://minorplanetcenter.net/
[3] https://cneos.jpl.nasa.gov/stats/site_all.html

year (Devillepoix et al. 2019). While asteroid impacts can be detrimental to life on Earth and have caused mass extinction events (Alvarez et al. 1980), they are also believed to have contributed minerals to Earth (Bottke et al. 2006, Brenan and McDonough 2009).

Impacts from large asteroids (i.e. >1 km), such as those capable of causing mass extinction events, are extremely rare, occurring on average once every 0.5 million years[4] (Devillepoix et al. 2019). In contrast, smaller asteroids (<1 km) are far more abundant and, although less catastrophic globally, are more likely to impact Earth during humanity's existence. However, despite their smaller size, these asteroids can still cause significant local damage, as seen with the Chelyabinsk meteor, which released substantial energy, resulting in powerful explosions and regional destruction (Brown et al. 2013). Therefore, it is also critical to keep monitoring and gaining a deeper understanding of smaller asteroids to prepare ourselves for these more likely future impacts. Although the majority of large ($> 1km$) near-earth asteroids (NEAs) have been identified, numerous smaller asteroids remain undetected (Harris and D'Abramo 2015). Encouragingly, the detection rate of NEAs with estimated diameters under 300 metres has significantly increased over the past decade.

Figure 1 shows the discovery statistics of NEAs for the year 2023, illustrating the distribution of NEAs discovered based on their absolute magnitude (H magnitude), which is a proxy for size. The distribution centres around an H magnitude ~ 25, which corresponds to a median size of about 37 metres in diameter, assuming an albedo of 0.15. The histogram shows 1,774 NEAs, representing 61.05 % of the total discovered population for the year 2023, have diameters smaller than 50 metres. However, despite the growing number of smaller NEAs being detected, their physical characteristics, such as taxonomic type, remain poorly understood. Therefore, it's crucial to keep up with follow-up observations to study these smaller asteroids. This helps both protect Earth from potential impacts and better understand the small NEA population.

[4] `https://impact.ese.ic.ac.uk/ImpactEarth/ImpactEffects/`)

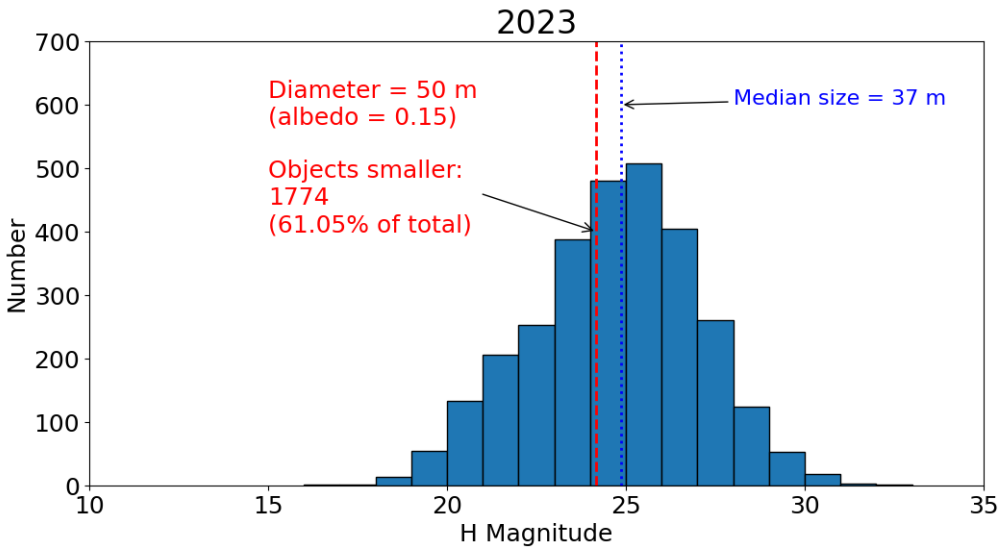

Figure 1: Histogram illustrating the distribution of absolute magnitude (H magnitude) for asteroids discovered in 2023. The x-axis represents the H magnitude, while the y-axis shows the number of asteroids for each magnitude range with H magnitude acting as an indicator of asteroid size. The blue dashed line marks the median size of the discovered asteroids, which is approximately 37 metres in diameter. The red dashed line represents a diameter of 50 metres, assuming an albedo of 0.15. Asteroids to the right of this line are smaller than 50 metres in diameter. The histogram shows that 1,774 asteroids, representing 61.05 % of the total NEAs discovered, have diameters less than 50 metres.

Studying smaller asteroids presents several challenges due to their fast motion and rapid changes in brightness as they pass Earth. These objects are often visible for only a brief period after discovery, necessitating immediate follow-up observations to collect valuable data. Traditional observing strategies are frequently too slow to respond effectively, highlighting the need for automated, rapid-response systems. To address this and the main topic of this thesis, the South African Astronomical Observatory's (SAAO) 1-meter telescope Lesedi, equipped with the Mookodi instrument, is used for rapid and automated follow-up observations of newly discovered NEAs. These observations are queue-scheduled for automatic execution and same-night follow-up, crucial for capturing data before the asteroids quickly fade from view.

The SAAO also hosts the third of four ATLAS nodes (Tonry et al. 2018), each discovering a new NEA every few days, along with other transient astronomical events. Many of these discoveries, especially small NEAs, lose brightness rapidly as they move away from Earth, leaving a limited window for follow-up. With an ATLAS node on site, the observatory is uniquely positioned for same-night follow-up observations on asteroids identified by

ATLAS. Since the campaign began in February 2023, numerous newly discovered NEAs have been observed, including some potentially hazardous asteroids (PHAs). This work highlights the advantages of automation and rapid response in maximising observational opportunities. Results obtained from multi-filter photometry and astrometric measurements contributed to refining asteroid orbits and analysing their colours.

Chapter 1 of this thesis discusses the South African Astronomical Observatory (SAAO) and explores the taxonomic classification of asteroids. Chapter 2 outlines the research methodology, detailing the telescopes and instruments used for observations, the implementation of the NEA follow-up program within the SAAO's Intelligent Observatory (IO) Project, and the automated observing requests and robotic observation system. This chapter also covers the data extraction processes and the use of photometric colours and machine learning for taxonomic classification. Chapter 3 presents the research outcomes, including asteroid taxonomic probabilities used to assign possible types based on spectra from the Bus-DeMeo classification scheme (DeMeo et al. 2009), a detailed discussion of photometric colours, and potential future applications of the work. The final chapter, Chapter 4, presents an overview of the research findings and proposes future developments, particularly focusing on strengthening the rapid follow-up capabilities for newly discovered Near-Earth Asteroids at SAAO facilities.

1 Background

1.1 The South African Astronomical Observatory's Site

The South African Astronomical Observatory's (SAAO) main observing site is located near Sutherland, a town in the Northern Cape province of South Africa shown in Figure 2. SAAO is positioned at an altitude of 1,800 metres in the Roggeveld Mountains. The site is characterized by its semi-arid climate and minimal light pollution, crucial for astronomical observations. The observatory's array of telescopes, including the Southern African Large Telescope (SALT), takes advantage of these favourable conditions, making it a suitable site for various astronomical observations.

Figure 2: Map showing the location of the South African Astronomical Observatory (SAAO) headquarters in Cape Town (33.9353° S, 18.4773° E) relative to its primary observing site in Sutherland (32°22'32.9"S, 20°48'38.9"E), approximately 400 km away. Both locations are marked with arrows above.

Figure 3 shows two key telescopes for this project at the SAAO: the Asteroid Terrestrial-impact Last Alert System – Sutherland (ATLAS-STH, Tonry et al. 2018) and the 1-m Lesedi telescope (Worters et al. 2016). These telescopes play a crucial role in detecting and monitoring Near-Earth Asteroids (NEAs) from Southern Africa, as will be discussed

in this thesis. ATLAS-STH is part of an international network dedicated to the early detection of NEAs, using its wide-field survey capabilities to identify potential asteroid threats before they approach Earth. This system's rapid detection capabilities are critical for early warning and risk assessment. The combination of ATLAS-STH and Lesedi located in the same observatory, offers a unique advantage by reducing the time between detection and follow-up of NEA's. This rapid response capability is important for timely impact risk assessment, especially for small asteroids whose brightness quickly fades as they move away from Earth.

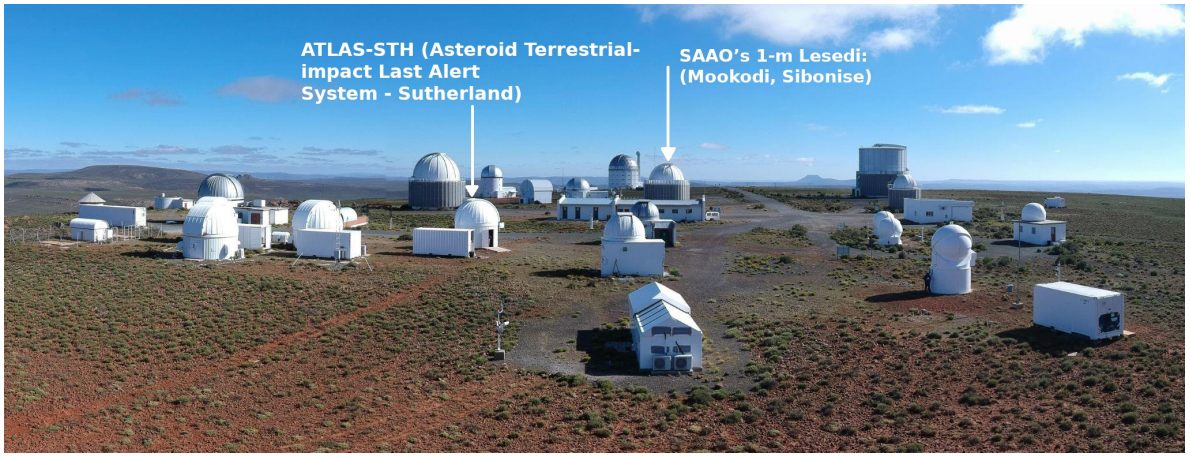

Figure 3: Key telescopes at the SAAO Sutherland observing site used in this project: ATLAS-STH (Asteroid Terrestrial-impact Last Alert System – Sutherland) and SAAO's 1-m Lesedi telescope. These telescopes play a crucial role in the rapid detection, observation, and follow-up of Near-Earth Asteroids (NEAs).

1.2 Minor Bodies and Near-Earth Asteroids

Around 4.6 billion years ago, the collapse of a massive cloud of gas and dust marked the beginning of our Solar System. Most of the material concentrated at the centre, forming the Sun, and smaller portions merged to form the planets. The strong gravitational forces exerted by Jupiter are thought to have prevented the formation of a planet in the Mars-Jupiter region by disrupting the accretion of planetary material (Morbidelli et al. 2009). Instead, this material formed the main asteroid belt, a vast region that spans approximately between 2.1 to 3.3 astronomical units (au) from the Sun, as illustrated in Figure 4. Within this belt, millions of asteroids vary in size from a few metres to several hundred kilometres across (Bottke et al. 2005). These objects are regarded as remnants of the early Solar System, providing information on the building blocks necessary for planetary formation (Raymond and Nesvorný 2022). In addition, asteroids have potential

as space resources, with some types, such as M-type (metallic) asteroids (see Section 1.4), possibly containing valuable elements and minerals.

Asteroids, often called minor planets, orbit the Sun throughout the Solar System and are not classified as planets. Near-Earth Asteroids (NEAs), which form the central focus of this project, are defined as asteroids whose orbits bring them within 1.3 astronomical units (au) of the Sun. It is anticipated that NEAs typically exists for about 10 million years (Granvik et al. 2018) before colliding with a terrestrial planet, the Sun, or being gravitationally expelled from the Solar System.

NEAs are classified into distinct types according to their orbital characteristics. There are four primary types of NEAs, three of which are illustrated in Figure 5. The four main types are:

- Aten Asteroids – Earth-crossing asteroids with semi-major axes smaller than 1 au
- Apollo Asteroids – Earth-crossing asteroids with semi-major axes larger than 1 au
- Amor Asteroids – Earth approaching asteroids with orbits that lie between the Earth and Mars
- Atiras - These have orbits inside the Earth's orbit

NEAs can be classified as potentially hazardous asteroids (PHAs) based on their probability of closely approaching Earth. PHAs are defined by a minimum orbit intersection distance (MOID) with Earth of less than 0.05 au (19.5 lunar distances) (Perna et al. 2015) and an absolute magnitude of 22 or brighter—where absolute magnitude (H) represents the apparent brightness of an asteroid if it were placed at a standard distance of 1 au from both the Sun and the observer, with a phase angle of zero degrees. This corresponds to a diameter of at least 140 metres (Mainzer et al. 2011). These objects are large enough to cause severe damage if they impact Earth, and their proximity makes them particularly relevant for observation.

Historical events, such as the impact that led to the extinction of the dinosaurs (Alvarez et al. 1980), emphasise the dangers posed by asteroid impacts. More recent incidents, including the 1908 Tunguska explosion (Krinov 1960; Longo 2007) and the 2013 Chelyabinsk event (Popova et al. 2013), where a meteor exploded in Earth's atmosphere over Russia, further highlight the need to study and monitor NEAs. In the Tunguska event, a small asteroid or comet fragment exploded in Earth's atmosphere, flattening millions of trees and causing a massive shock wave.

Asteroids have been the subject of many space missions. Robotic missions like NASA's OSIRIS-REx (Lauretta et al. 2021) and Japan's Hayabusa2 (Watanabe et al. 2019) successfully collected and returned samples from asteroids like Bennu and Ryugu, providing

critical data on the conditions of the Solar System's formation. Additionally, NASA's Double Asteroid Redirection Test(DART) mission (Cheng et al. 2023, Chabot et al. 2024) successfully demonstrated planetary defence by impacting the moonlet of asteroid Didymos with a kinetic impacter, altering its trajectory and showcasing the potential to protect Earth from future asteroid impacts.

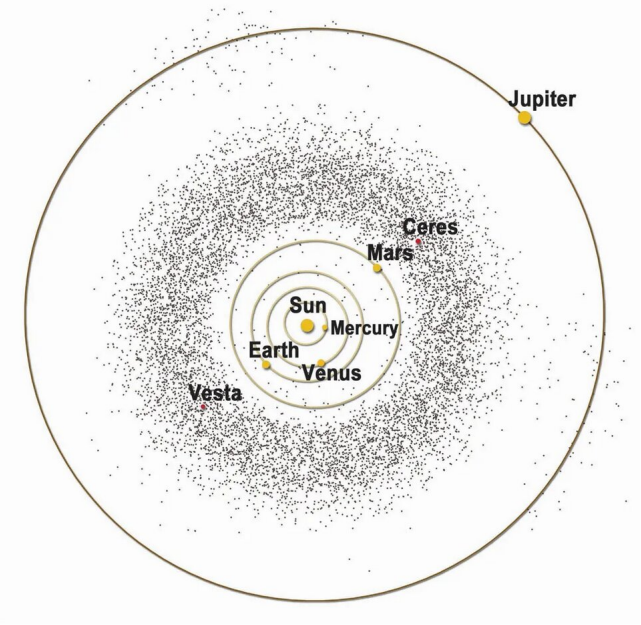

Figure 4: Distribution of asteroids in the main asteroid belt and Trojan asteroids along Jupiter's orbit, with the inclusion of Near-Earth Asteroids (NEAs) illustrating their paths around the Sun, between Mars and Jupiter. Source: `http://www.solstation.com/stars/asteroid.htm`

1.3 Asteroid Discovery

The majority of asteroids are discovered through optical observations using ground-based telescopes, which scan the night sky for objects that move relative to the fixed background of stars. Small asteroids can be faint and fast-moving when they come close to Earth, therefore sensitive telescopes with wide sky coverage are required for detecting these objects. The dedicated sky surveys like the Panoramic Survey Telescope and Rapid Response System (PanSTARRS; Chambers et al. 2016) and the Catalina Sky Survey (CSS; Larson et al. 1998) use automated telescopes to detect asteroids. Recently, space telescopes like

the Near-Earth Object Wide-Field Infrared Survey Explorer (NEOWISE[5]; Mainzer et al. 2011) have further contributed to asteroid discovery by scanning the infrared portion of the electromagnetic spectrum, which helps identify previously unknown objects. Once a potential asteroid is identified, follow-up observations are conducted to determine its orbit accurately.

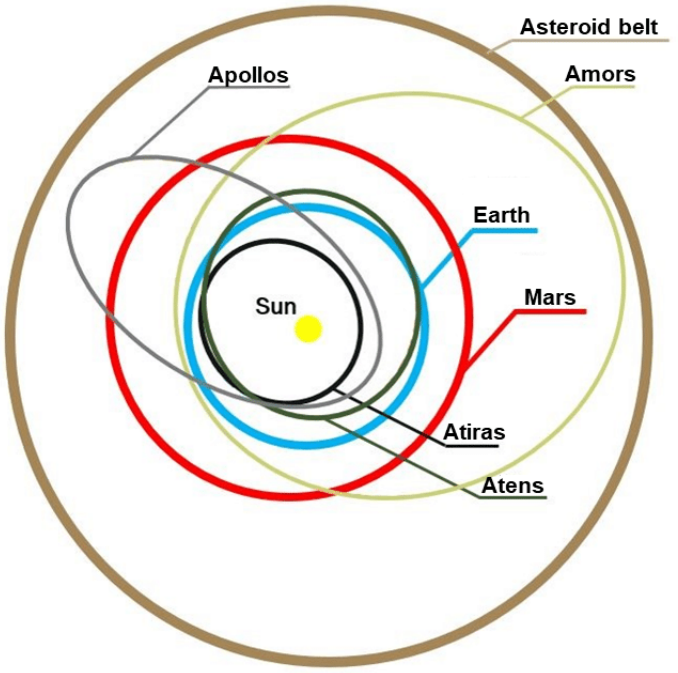

Figure 5: Shows the four main orbits of Near-Earth Asteroids (NEAs) based on orbital paths: Atira, Atens, Apollos and Amours. Source: `https://astronomy.swin.edu.au/cosmos/n/Near+Earth+Asteroids`.

Looking ahead, the upcoming Vera C. Rubin Observatory Legacy Survey of Space and Time (LSST)[6] (formerly the Large Synoptic Survey Telescope, LSST; Collaboration et al. 2020) is anticipated to significantly increase the number of Near-Earth Asteroid (NEA) discoveries through its wide-area, deep-sky surveys (Jones et al. 2020). This observatory will produce an extensive dataset that will allow astronomers to detect, track, and characterize even more NEAs, thus enhancing our understanding of their distribution and potential threats to Earth. Figure 6 shows the cumulative number of discovered NEAs from 1980 to date.

The continuous improvement in telescope technology and the increase in the number

[5] `https://science.nasa.gov/mission/neowise/`
[6] `https://www.lsst.org/`

of sky surveys have significantly increased the detection of NEAs, leading to steadily increasing discovery rates in recent years. More than 2,000 NEAs have been found each year since 2020. The diameter of discovered NEAs ranges from a few metres to kilometres as shown in Figure 6. Notably, the majority of newly discovered NEAs are smaller in size. However, particular attention is directed toward those with diameters less than 1 kilometre but greater than 140 metres, as these have the potential to impact Earth and cause significant harm despite their relatively modest size.

The Minor Planet Center (MPC)[7] which operates under the support of the International Astronomical Union (IAU), is responsible for cataloguing and managing data related to minor planets, including asteroids and comets. It is responsible for collecting precise positional data of all the asteroids that have been discovered, aiding in determining their accurate orbits.

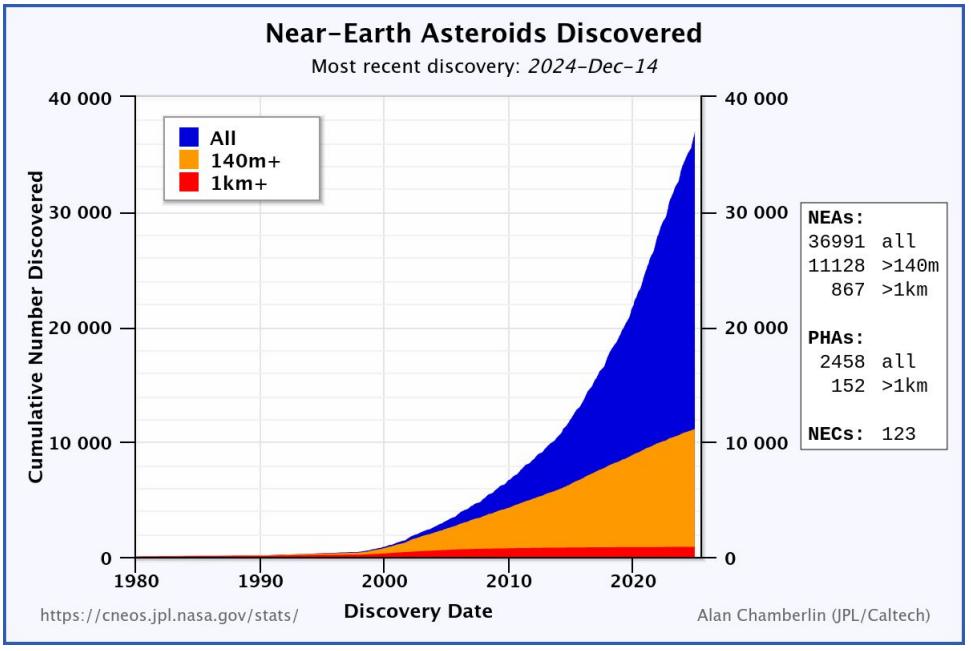

Figure 6: Plot illustrating the cumulative number of discovered Near-Earth Asteroids (NEAs). It includes totals for all NEAs, as well as those specifically larger than approximately 140 metres and those larger than approximately 1 kilometre. Source: `https://cneos.jpl.nasa.gov/stats/totals.html`

Additionally, the MPC assigns provisional designations to newly discovered asteroids and, upon orbital confirmation, after independent follow-up, official designations, and sometimes names. This centre maintains a catalogue, periodically publishing circulars with

[7] `https://www.minorplanetcenter.net/iau/mpc.html`

updates on minor planets and providing ephemerides for predicting their positions. Collaborating with observatories, astronomers, and space agencies worldwide, the MPC ensures the effective tracking and monitoring of minor planets, particularly those approaching Earth. The centre gathers astrometric observations from different observatories, enabling the determination of precise positions of asteroids and comets.

For this project, astrometric reports of the asteroids followed up on using the Lesedi telescope were submitted to the MPC. This submission process is important for refining the orbits of these NEAs, enabling more accurate predictions of their future positions to assess potential impact threats on Earth.

The Near-Earth Object Confirmation Page (NEOCP[8]), a service offered by the MPC, is a tool for monitoring recently discovered Near-Earth Asteroids (NEAs). The NEOCP lists unconfirmed objects awaiting orbital validation through follow-up observations. Upon detection, an asteroid is assigned a provisional designation along with astrometric data, including its position and motion. This information is made available to observatories worldwide for validation.

Observers use the NEOCP data to conduct follow-up observations, confirming the object's existence and refining its orbital parameters. Upon confirmation, the asteroid retains its provisional designation until it receives an official number and is subsequently transferred to the MPC's database. Accurate orbit determination of confirmed NEAs enables astronomers to project their future trajectories and assess potential impact risks to Earth. Such assessments are essential for the development of deflection strategies in the event of a predicted collision.

The Centre for Near-Earth Object Studies (CNEOS)[9], operated by NASA's Jet Propulsion Laboratory (JPL)[10], plays a vital role in monitoring and forecasting the orbits of NEAs. CNEOS focuses on refining impact risk assessments for potentially hazardous objects, improving the precision of these evaluations, and generating accurate orbital forecasts. Additionally, it provides essential resources for orbit computation and impact hazard assessment, enabling global preparedness for potential asteroid threats.

1.4 Taxonomic Classification of Asteroids

Asteroids are primarily categorised into different types based on their reflectance spectrum. In cases where spectral data is unavailable, classification can be inferred from colour and/or albedo as approximations, which are indicative of their surface compositions. Generally, smaller bodies have minor differences between their surface and internal

[8] https://cneos.jpl.nasa.gov/scout/intro.html
[9] https://cneos.jpl.nasa.gov/
[10] https://www.jpl.nasa.gov/

compositions, whereas larger asteroids often exhibit significant differences between their surface and internal structures (Elkins-Tanton et al. 2011).

Asteroids are primarily classified into three major types: C-type (Carbonaceous), S-type (Silicaceous), and M-type (Metallic). The majority of asteroids are C-type, characterized by dark surfaces with a reflectivity of 3% to 4%, indicating carbon-rich materials similar to coal. These asteroids consist mainly of silicates mixed with carbon compounds, making them chemically primitive and relatively unchanged since the formation of the Solar System. C-type asteroids are prominent in the outer regions of the asteroid belt (DeMeo and Carry 2013).

The second major group, S-type asteroids, has a higher albedo due to their silicate-rich, or stony composition (Bus and Binzel 2002). This composition suggests that S-types formed in a different environment, possibly closer to the Sun, where conditions favoured the formation of silicate minerals (Bottke et al. 2002).

A third, less common class is the M-type asteroids, which are primarily composed of metallic nickel-iron. These asteroids have high albedos and exhibit spectral features indicative of their metal content. It is believed that M-type asteroids originated from parent bodies large enough for their molten interiors to differentiate, with heavier metals sinking to the core. Subsequent collisions shattered these bodies, leaving behind metal-rich fragments (Gaffey 1976, Cloutis et al. 1990, Gaffey et al. 1993, Fornasier et al. 2010).

The classification of asteroids has evolved significantly over time. The Tholen classification system, developed by Tholen (1984, was one of the earliest and categorized asteroids based on visible wavelength spectra, introducing the major classes such as C-type, S-type, and M-type. The Small Main-Belt Asteroid Spectroscopic Survey (SMASS), developed by Schelte Bus, refined the Tholen taxonomy by incorporating more detailed spectral data and distinguishing additional subclasses within the original categories (Bus and Binzel 2002). The most recent and widely used classification scheme is the Bus-DeMeo classification, introduced by DeMeo et al. 2009. This system builds upon the SMASS taxonomy by integrating near-infrared spectral data, resulting in 24 distinct classes and providing deeper insights into asteroid compositions and their evolutionary histories.

Tholen classification

The first asteroid classification system was proposed by Tholen (1984. This system is primarily based on broadband spectra collected during the Eight-Colour Asteroid Survey (ECAS, Zellner et al. 1985) in the 1980s, encompassing wavelengths from 0.31 to 1.06 micrometres. It also incorporates albedo measurements and was initially founded upon a dataset of 978 asteroids. Tholen's classification consists of 14 distinct types, with most asteroids falling into one of three primary categories and several smaller subtypes. This system categorizes asteroids into three primary groups based on their spectral properties and albedo measurements:

- **C-group:** This group consists of dark, carbonaceous asteroids with low reflectivity. C-type asteroids, the most common within this category, are rich in carbon compounds and silicates. The C-group also includes subtypes like B-types, which are slightly brighter, and the rarer F-type and G-type asteroids.
- **S-group:** Comprising silicaceous or stony asteroids, this group features higher reflectivity due to their silicate-rich surfaces. S-type asteroids are abundant and include various subtypes such as V-types, which are associated with the asteroid Vesta and thought to originate from significant impacts on Vesta. Other subtypes include A-type, Q-type, and R-type asteroids.
- **X-group:** This overarching category is divided into P-types, which are dark and primitive with very low albedo; M-types, which are metallic with intermediate reflectivity; and E-types, which are bright and enstatite-rich.

SMASS Classification

In 2002, astronomers Schelte Bus and Richard Binzel introduced a more recent asteroid taxonomy, taken from the data of the Small Main-Belt Asteroid Spectroscopic Survey (SMASS) of 1,447 asteroids, which provided higher-resolution spectra compared to the earlier Eight-Colour Asteroid Survey (ECAS) mentioned in the Tholen classification. While SMASS observed a narrower range of wavelengths (0.44 to 0.92 micrometres) and didn't consider albedos, it resulted in 26 distinct asteroid types, aiming to align with the Tholen classification as closely as possible, considering the differing data.

The taxonomy comprises three major categories similar to the Tholen classification, including:

- The C-complex, encompassing carbonaceous objects, with the C-type as the "standard" non-B carbonaceous asteroid, the "brighter" B-type, Cb-type transitioning between C and B types, and Cg, Ch, and Cgh-types somewhat related to the Tholen G-type, with the h denoting hydrated.
- The S-complex, consisting of silicaceous (stony) objects, includes the common S-type asteroid and additional types such as A, Q, R, K, L, Sa, Sq, Sr, Sk, and Sl that bridge between S-type and other related classes.
- The X-complex, mostly composed of metallic objects, contains the primary X-type asteroids and transitional types like Xe, Xc, and Xk between X and other corresponding classes.

Bus-DeMeo Classification

The Bus-DeMeo classification was developed by Francesca DeMeo, Schelte Bus, and Stephen Slivan (DeMeo et al. 2009). This system categorizes asteroids based on their reflectance spectrum characteristics, using data from 371 asteroids measured over a wavelength range of 0.45 to 2.45 micrometres.

Building on the Tholen classification, the Bus-DeMeo taxonomy incorporates near-infrared spectral data, providing a more detailed understanding of asteroid compositions. This expanded system divides asteroids into 24 distinct classes introducing new types such as the Sv-type, as shown in Figure 7. The classification is based on a principal component analysis following the Small Main-Belt Asteroid Spectroscopic Survey (SMASS) taxonomy, which itself is derived from the Tholen classification.

Among the key classes in the Bus-DeMeo system are the B-type, V-type, and D-type asteroids. B-type asteroids, a subset of C-type, exhibit distinctive blue spectra and are believed to contain a high concentration of water and organic materials. V-type, or Vestoids, have a basaltic composition and are thought to originate from the crust of differentiated parent bodies, with Vesta, one of the largest asteroids in the main belt, being the primary source of this material (Binzel and Xu 1993). D-type asteroids are characterized by their very dark appearance, low albedo, and featureless red spectra. This refined classification system offers deeper insights into the diversity and origins of asteroids, contributing significantly to our understanding of the early solar system.

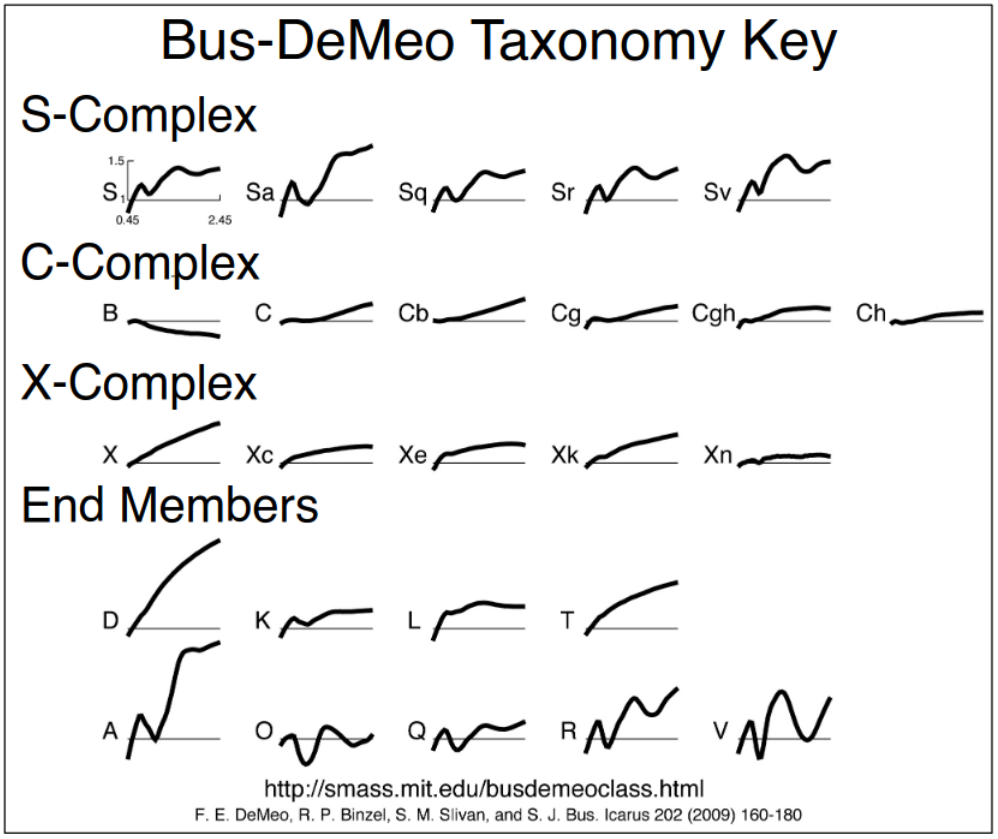

Figure 7: Shows all 24 taxonomic classes in the Bus-DeMeo classification scheme defined over the wavelength range of 0.45–2.45 μm, with the three main complexes S, C, and X. Source: `http://smass.mit.edu/busdemeoclass.html`

Classifying Near-Earth Asteroids (NEAs) helps us better understand their diverse characteristics and nature. The majority of NEAs are classified as C-type or S-type (Mommert et al. 2016). However, classifying small NEAs poses significant difficulties. Their faintness and rapid movement complicate the collection of detailed spectral data, leading to a lag in their comprehensive characterisation. While large NEAs benefit from extensive observation and more detailed classification, small NEAs often remain poorly characterized. This gap in data is further compounded by discrepancies observed between meteorites and the asteroids they represent. Meteorite samples collected on Earth sometimes do not align with the expected composition of their corresponding asteroids, which may be attributed to differences in sampling techniques, asteroid surface processes, or observational limitations. Addressing these challenges is important for enhancing our understanding of NEA composition

Several studies have investigated the distribution of taxonomic classes among Near-Earth

Asteroids (NEAs). Mommert et al. 2016 found that approximately 45% of their sample belonged to the S-complex type, though this proportion was lower than that of ordinary chondrites in meteorite fall statistics, suggesting a discrepancy between asteroid compositions and meteorite types. Similar findings were reported by Binzel et al. 2004, Erasmus et al. 2017, and Janse van Rensburg 2021 who observed higher fractions of S-type asteroids. This project seeks to further examine this trend, particularly the prevalence of S-types among NEAs, to gain a clearer understanding of their distribution.

2 Research Methodology

Various methods have been employed to observe and classify Near-Earth Asteroids (NEAs) by taxonomic type, primarily through spectroscopy and multi-band photometry. Spectroscopy is particularly effective for distinguishing asteroid types with distinct spectral features. For example, S-type asteroids typically exhibit silicate absorption bands, while C-type asteroids show flatter, featureless spectra (Popescu et al. 2019). Multi-band photometry, on the other hand, measures light intensity through a set of discrete filters. When these measurements cover a wide range of wavelengths, photometric colours can approximate the spectral slope of an asteroid's reflectance spectrum. This spectral slope provides critical information about an asteroid's surface composition and enables researchers to infer its taxonomic classification (Erasmus et al. 2018, Devogèle et al. 2019).

Spectroscopy provides higher spectral resolution and more detailed compositional insights, enabling precise identification of mineral compositions and surface properties. However, it requires longer observation times and typically larger telescopes, making it less practical for rapid survey work or observations of fainter objects. In contrast, multiband photometry offers practical advantages for large-scale surveys, allowing for the rapid classification of numerous asteroids simultaneously. This efficiency is demonstrated by near-infrared (NIR) photometric colour analyses from the MOVIS catalogue, which assign compositional types based on broad wavelength data (Popescu et al. 2018). Recent studies (Erasmus et al. 2019, Janse van Rensburg 2021, Hromakina et al. 2021) show that carefully chosen filter sets spanning ultraviolet, visible, and near-infrared wavelengths can effectively distinguish between asteroid types, even when their spectra exhibit similar features. Supporting this approach, the overlap between the SDSS g-, r-, and i-band filters and the reflectance spectra for asteroid types as shown in Figure 8 demonstrates how these filter sets enable efficient classification based on taxonomic features.

The advantages of spectroscopy include detailed compositional analysis and precise mineral identification, whereas photometry offers rapid data collection and requires less telescope time. These characteristics make photometric methods particularly well-suited for initial taxonomic classification and for observing newly discovered NEAs with small observational windows using modest (1-meter) telescopes. However, photometric methods do provide lower spectral resolution than spectroscopic observations. Additionally, as discussed in Section 1.3, observing small ($< 300\,m$) NEAs poses challenges regardless of the chosen method, as these objects tend to be faint and move rapidly during close approaches with Earth.

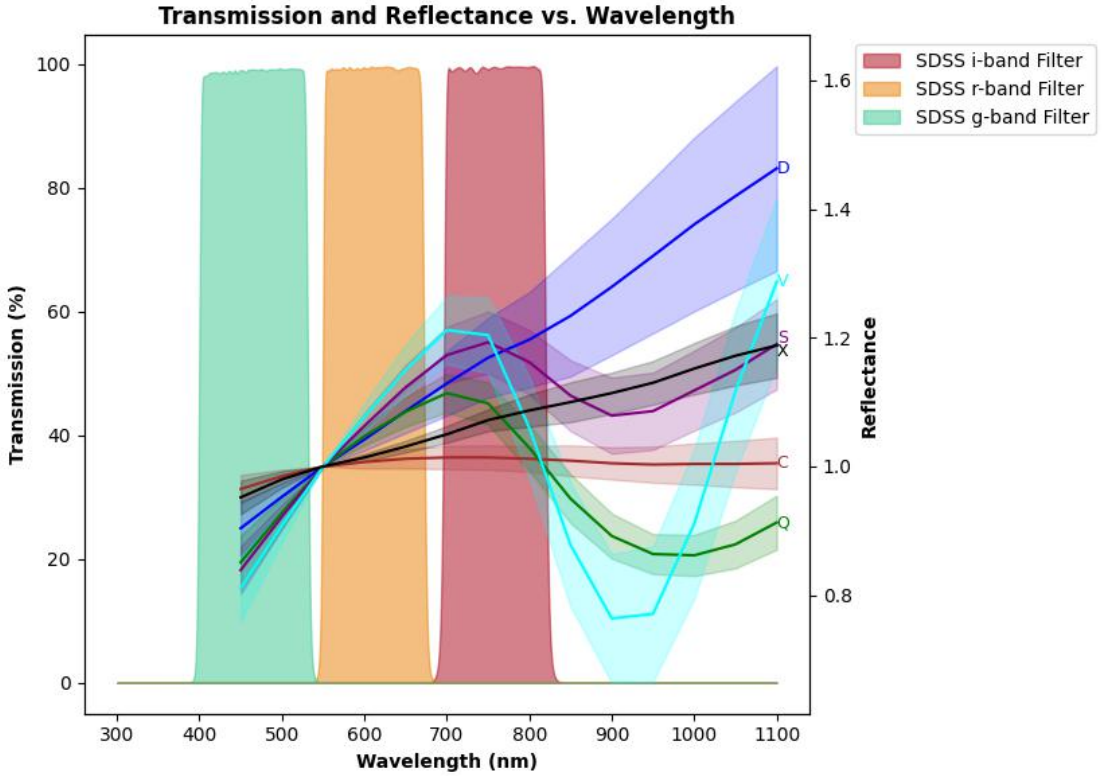

Figure 8: Transmission profiles of the SDSS g- (green), r- (orange), and i-band (red) filters on the Mookodi instrument are shown alongside the average reflectance spectra from the Bus-DeMeo taxonomic scheme asteroid taxonomic classes: S-type (purple), C- (red), X- (black), D- (blue), Q- (green), and V-type (cyan). The shaded regions represent the transmission ranges of the filters, while reflectance uncertainty bands for each taxonomic class are also displayed. The plot shows the spectral overlap between the filters on Mookodi and the characteristic features of the asteroid types. The $g' - r'$ and $r' - i'$ colours can measure the spectral slope allowing differentiation between the taxonomic classes displayed.

This project uses photometric observations to calculate colour indices for NEA classification. While this approach may not provide the fine compositional detail achievable through spectroscopy, it enables a broad survey of faint, small high H-magnitude NEAs that are under-represented in taxonomic datasets. The classification method was further refined using machine learning models trained on existing spectroscopic and photometric datasets from previous work (Janse van Rensburg 2021) to generate a decision boundary that determines the most probable classification based on an asteroid's position relative

to this decision boundary surface.

Observations were conducted using the Mookodi instrument mounted on the Lesedi telescope (Worters et al. 2016), a fully robotic system that enables remote operation at the SAAO's observing site. The Lesedi telescope is a key component of SAAO's Intelligent Observatory (IO) project (Potter 2021), an initiative designed to enhance the robotic capabilities of the observatory's telescopes and instruments for rapid response observations of transient events. In 2022, the Lesedi telescope and Mookodi instrument became the first telescope-instrument combination to be successfully integrated into the IO project, enabling automated queue-scheduled observations.

2.1 Telescope and Instrument

Lesedi

The Lesedi telescope features a 1-meter Ritchey-Chrétien design, built by APM Telescopes[11]. Its primary mirror operates at a focal ratio of f/8, complemented by field-correcting optics that ensure a flat focal plane. At the SAAO site, where the telescope operates, typical seeing conditions measure around 1.2 arcseconds, with the best nights rarely improving beyond 1 arcsecond. To match these conditions and achieve optimal resolution, the spatial sampling rate is set at approximately 0.6 arcsec/pixel at the detector.

The telescope's alt-azimuth mounting system incorporates two Nasmyth ports, designated as "left" and "right" when viewed from behind the stationary telescope, facing the rear of the primary mirror cell, as shown in Figure 9. Each port features identical corrector optics and an auto-guider system. A software-controlled, motorised tertiary mirror enables rapid switching between instruments on either port within seconds. Currently, the Mookodi instrument (Erasmus et al. 2024), a low-resolution spectrograph and multi-filter photometric imager used in this project, occupies the right-hand port, while Sibonise, a semi wide-field multi-filter photometric imager, is mounted on the left port.

The telescope's operational range allows for safe pointing at any elevation between 30 and 89 degrees above the horizon. When reaching its azimuth limit, the telescope automatically ceases tracking and can be redirected to a new target.

[11] https://www.apm-telescopes.net/de/

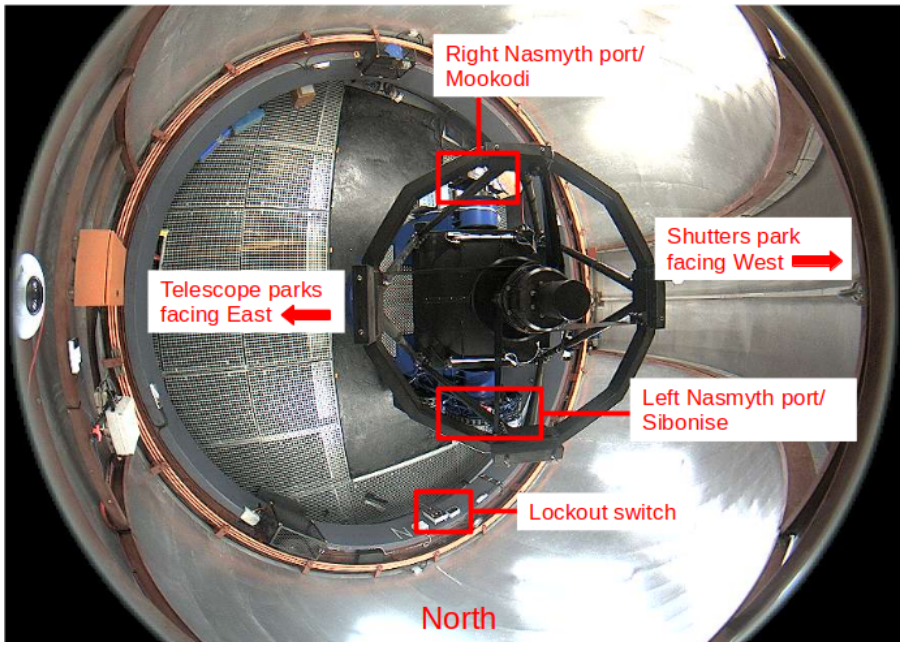

Figure 9: Annotated aerial view of the Lesedi telescope at the SAAO. The right Nasmyth port hosts the Mookodi instrument, while the left Nasmyth port is equipped with Sibonise. The telescope parks face East, and the dome shutters park faces West. A lockout switch is also visible, with the image-oriented toward the North. (Source:`https://topswiki.saao.ac.za/index.php/Lesedi`)

Mookodi

The Mookodi instrument, developed by the Astrophysics Research Institute of Liverpool John Moores University (LJMU), is a fully robotic low-resolution spectrograph and imager. Based on the Spectrograph for the Rapid Acquisition of Transients (SPRAT; Piascik et al. 2014), Mookodi features significant enhancements over its predecessor. While SPRAT uses a rectangular detector (26.6,mm × 6.6,mm, 1024,px × 255,px), Mookodi employs a square detector (13.3,mm × 13.3,mm, 1024,px × 1024,px). This upgrade, combined with two filter-slide mechanisms, enables Mookodi to function as both a spectrograph and a multi-filter photometric imager because of the additional inclusions of two filter-slide mechanisms that SPRAT does not have, allowing seamless transitions for rapid follow-up observations in robotic mode.

As shown in Figure 10, Mookodi's key components include a flat/arc lamp mirror, entrance slit, and grism, all mounted on electronically controlled pneumatic pistons. These components can be remotely retracted from the beam, converting the instrument into an imager within seconds. The grism serves as the dispersion element in spectroscopy mode, combining a transmission grating with prisms to disperse light while maintaining

a straight-through optical path. This design eliminates the need to reposition or realign optical components when switching between modes. Calibration frames can be efficiently acquired using an arc/flat lamp mirror, which directs light from calibration lamps below the instrument into the slit. The instrument employs an Andor iKon-M 934 (BEX2-DD) detector, featuring a 1024 × 1024 pixel array with 13 µm pixels.

In imaging mode, Mookodi provides a field of view of 10 arcmins × 10 arcmins with a plate scale of 0.59 arcsec/pixel (1 × 1 binning). The instrument is equipped with a Sloan Digital Sky Survey (SDSS) filter set (u, g, r, i, z), enabling multi-filter photometric imaging. Under high-gain, fast-readout conditions with 60-second exposures, it achieves a limiting magnitude of 20 in r and 19.5 in other bands (excluding the u band).

In spectroscopy mode, Mookodi operates across a wavelength range of 4000–8000 Å with a spectral dispersion of 3.86 Å/px. The instrument offers both narrow (2 arcsec) and wide (4 arcsec) slit options, achieving spectral resolutions from R = 360 at 4600 Å to R = 420 at 7600 Å. For a 16th-magnitude target with a 1000-second exposure, it achieves a signal-to-noise ratio (SNR) greater than 5, making it well-suited for rapid response to transient events. For this project, the spectroscopy mode is not used since auto-target acquisition for non-sidereal objects is not yet supported in robotic mode.

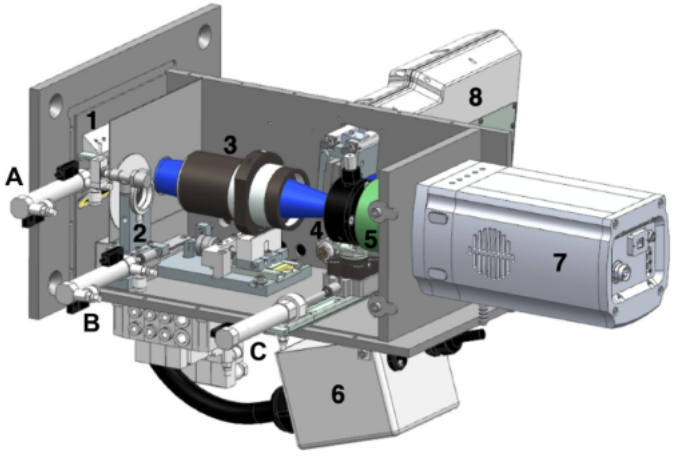

Figure 10: Shows the main parts of the instrument labelled as follows: (1) flat/arc lamp mirror; (2) spectrograph entrance slit; (3) collimator lens assembly; (4) VPH transmission grating and prism pair assembly (i.e., the grism); (5) re-imaging lens; (6) housing for the arc and flat lamp; (7) detector camera; and (8) filter slide housing. This is a view of the instrument's overview CAD render. (A), (B), and (C) are the labels of the pneumatic pistons that can operate the slit, the grism in/out of the beam, and the flat/arc lamp mirror, respectively. Source: Erasmus et al. 2024

2.2 The SAAO's Intelligent Observatory Project

The South African Astronomical Observatory (SAAO) initiated the "Intelligent Observatory" (IO) project (Potter 2021) to enhance rapid-response capabilities for transient observations. The project aims to integrate all SAAO telescopes and instruments into a unified system that enables flexible, real-time observation scheduling. This system allows astronomers to submit proposals at any time, choose between manual or automated telescope control, and have observations queued based on priority. The IO primarily focuses on time-domain and transient science, employing intelligent algorithms to monitor alert streams and automatically generate observation requests.

The Lesedi telescope and Mookodi instrument represent the first telescope-instrument combination integrated into the IO project. Their fully robotic operation makes them particularly suited for rapid follow-up observations of near-Earth asteroids. The system uses a customised version of the open-source Observatory Control System (OCS) software[12], originally developed by Las Cumbres Observatory (Brown et al. 2013) and adapted by the SAAO's IO team. An "asteroid watchdog" script (Shown in Appendix B) monitors the JPL scout webpage every 15 minutes for discoveries, which compiles real-time findings submitted to the Minor Planet Center (MPC). When the script identifies an observable target, it automatically sends an observing request to the SAAO's OCS, which then schedules observations for the Lesedi telescope in robotic mode. While the OCS can accept and schedule observation requests, sidereal tracking is specifically used for these observations. This approach is deliberate, as the pipeline (detailed in Section 2.3.2) relies on stable field stars as reference points. Non-sidereal tracking would cause the background stars to appear to move between frames, thereby compromising the pipeline's ability to perform reliable calibration and analysis.

2.3 Automated Observing Requests and Robotic Observation

2.3.1 Observing Strategy

The observing strategy involves a sequence of 1-minute exposure times. The sequence chosen includes clear, g, r, and i, repeating that sequence 3 times, with each follow-up observation estimated to take approximately 20 minutes. This duration encompasses a total exposure time of 12 minutes, consisting of 12 exposures at 1 minute each, along with an additional 2 minutes for target acquisition and filter slide dead-time (cycling filters of 12×5 seconds, totalling 1 minute). Each object is allocated 20 minutes for observations. Repeating the sequence more than three times would be impractical due to the fast motion of the asteroid across the sky, which could result in the object moving out of the field

[12] `https://observatorycontrolsystem.github.io/`

of view (FOV) before enough data could be collected. On the other hand, repeating the sequence only once would not provide sufficient colour data for accurate taxonomic classification.

Upon completion of the observation, the LCU reports back to the OCS, confirming that the observation was successfully executed. This triggers notifications to the PIs, who are then able to retrieve the data from the data repository. The PIs perform data reduction, extracting astrometric measurements from the collected frames. For this project, astrometric data was extracted from the observations and submitted to the MPC, joining similar contributions from the broader astronomy community and incorporated into their database for orbital refinement. This process involved manually tracking and selecting each asteroid as it moved across successive frames. The MPC uses this collective astrometry to determine orbital parameters, eventually assigning official designations to asteroids once sufficient observational data has been accumulated (typically several days after initial discovery). All submitted observations contributed directly to improving orbital parameter accuracy, with the Lesedi telescope subsequently acknowledged on official MPC designation pages once asteroids received formal designation. This community-contributed astrometry plays an essential role in the MPC's asteroid designation system. This designation enables the use of an existing Photometry Pipeline to extract calibrated photometry from the g, r, and i, data frames. The extracted photometric colours, along with the estimated asteroid taxonomy, contribute to ongoing research efforts. This streamlined process ensures that follow-up observations, data acquisition, and analysis are carried out efficiently for newly discovered NEAs.

2.3.2 The Automated Script to Check for New Discoveries

This automated script (see Appendix B) allows follow-up observations of NEAs through the SAAOs Observatory Control System (OCS). This script relies heavily on Python's astronomical libraries and tools, particularly `astropy`. The script uses multiple components to enable rapid follow-up of NEAs under different observational conditions. The script uses two main external services that provide essential astronomical data on newly discovered NEAs. The JPL Scout API which is is the primary source for real-time information about newly discovered NEAs, while the MPC API provides the precise orbital elements used to track the location of the asteroid. The main goal of this Python script is to identify observable NEAs from the JPL Scout page and send an automated observing request without any human intervention.

The NEOCP [13] monitor continuously checks for new potential targets, while the target filter applies observational constraints to ensure efficient use of telescope time. The primary observing constraints include a declination limit of 25 degrees. The field of view (FoV) is

[13] `https://cneos.jpl.nasa.gov/scout/intro.html`

set to 8 arcminutes, to ensure the object will fall within the detector's imaging area. The system specifically focuses on objects from certain surveys, accepting targets designated with prefixes 'A1' (ATLAS), 'P' (Pan-STARRS), 'C' (Catalina), 'ZT' (Zwicky Transient Facility), or 'xkos' from the Moonbase South Observatory. This survey-based selection ensures focus on reliable sources while filtering out potentially less reliable detections from other programs. The script continuously checks for observable targets every 15 minutes, and the automated observing requests are sent through SAAO's OCS after sunset using the required JSON format. The observation request is filled with all the necessary orbital elements and parameters obtained from the Minor Planet Centre.

The workflow (shown in Figure 11) begins by checking post-sunset conditions using `astropy` time calculations and evaluating lunar illumination conditions to make sure each observation occurs under the right conditions. At the start of this program, the magnitude limit (`mag limit`) was set at 19.5 to try to observe the faint objects. This was successful in that we were able to observe a lot of faint objects but they were too faint to extract reliable colours (see Section 2.5) needed to find their possible taxonomic types. The base `mag limit` was then set at 18.7, but this threshold is adjusted under different lunar phases. During new moon conditions, when lunar illumination is less than or equal to 0.1, the `mag limit` is extended by one full magnitude to 19.7 to detect fainter objects. For intermediate lunar phases, where illumination falls between 0.1 and 0.5 (crescent and half-moon conditions), the `mag limit` is increased by 0.5 to 19.2. When lunar illumination exceeds 0.5, typically full moon, the system maintains the pre set `mag limit` of 18.7. This decision was made to avoid overextending the observational capabilities and ensure that the observations produced reliable data. This observational strategy effectively maximizes the allocated telescope time and consistently produces reliable colours from these observations, enabling the classification of NEAs.

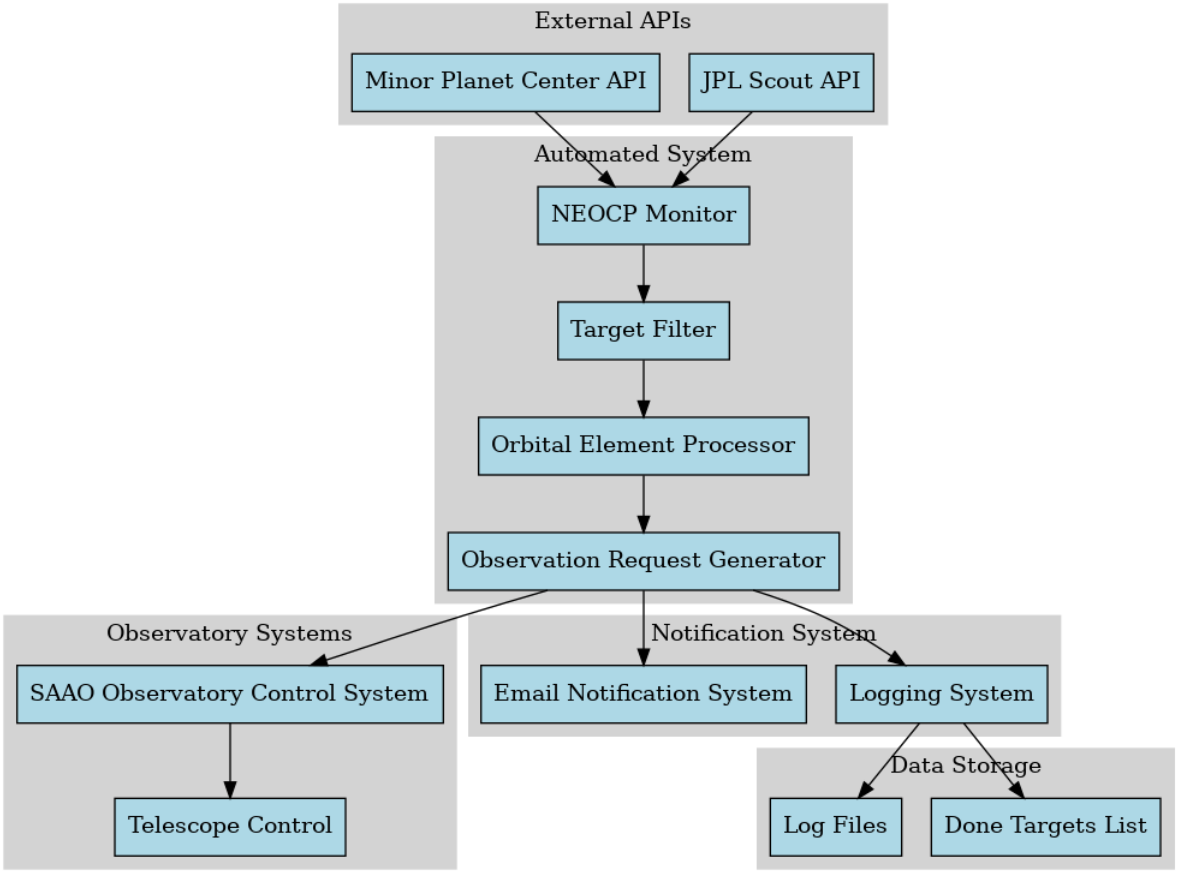

Figure 11: Overview of the Automated System for NEA Observations

After it collects potential targets to be observed from NEOCP, the script then retrieves the object's ephemeris before generating the observing request. These object ephemeris are the orbital inclination ("orbinc"), the longitude of the ascending node ("longascnode"), the perihelion ("argofperih"), the eccentricity ("eccentricity"), the mean distance ("meandist"), the mean anomaly ("meananom") and finally the epoch ("epochofel") as shown in the code in Appendix B. An email notification system keeps the PI's informed once the observation is done. This will involve retrieving the data and running it to the reduction to astrometry to the MPC and the PHOTOMETRYPIPELINE to extract colours for classifying the observed NEAs. This is the only part of the program that still needs human intervention. The script keeps a log of all the targets that have been observed in a database stored in `done_targets.txt`. This file is then used in the filtering process to avoid observing the same target again.

2.4 Astrometric and photometric data extraction

2.4.1 Reduction Pipeline

For this project, an SAAO-developed open source Python script[14] was used for the data reduction process of all images captured with the Mookodi instrument, specifically for bias and flat-field correction (see Appendix D). This is done before astrometric measurements are extracted from the clear-filter images, and photometric data from the g, r, and i-filter images. The script reads in directories containing the science, bias, and flat-field images. It first generates a master bias by stacking multiple bias frames which is then subtracted from each science image to remove any noise. Dark frame corrections were not applied as the Andor iKon-M 934's low dark current (0.01700 e^-/pixel/sec) results in negligible dark signal accumulation ($\sim$0.51 e^-/pixel) over the 30-second exposures, well below the readout noise floor.

The script then subtracts the bias from each flat-field image to produce a master flat, which takes into consideration pixel-to-pixel variations in detector sensitivity. For consistent photometric measurements, the resulting master flat is used to normalize the brightness throughout the image. After that, the reduced science images are created by dividing the bias-corrected images by the master flat, which makes sure that all pixel values are adjusted for sensitivity variations as well as noise. In order to prevent saturation, the script also cleans up the data by capping the pixel values to 2^{16} bits and setting any negative values to zero.

The script includes a check for the instrument's sky angle, which allows for the correction of image orientation, ensuring consistency with the actual sky field. This ensures that the reduced images are not only corrected for detector effects but also correctly oriented for subsequent analysis. This reduction process was important for this project, as it prepared the images for more accurate measurements when extracting astrometric data and photometric colours. Finally, a folder is created which contains the reduced images labeled with the prefix "MKred", indicating that the reduction process has been completed.

2.4.2 Overview of Asteroid Astrometry Extraction Script

This script (shown in Appendix C) processes asteroid observations captured in FITS format. It guides users through a folder of asteroid images, allowing them to manually identify the asteroid in each frame by hovering over it and pressing the spacebar. The selection can be refined multiple times until satisfied, then press Enter to confirm.

For each image, the script performs astrometric calibration using SAAO's local installation

[14] `https://topswiki.saao.ac.za/index.php/Mookodi#Data_Reduction_Pipelines`

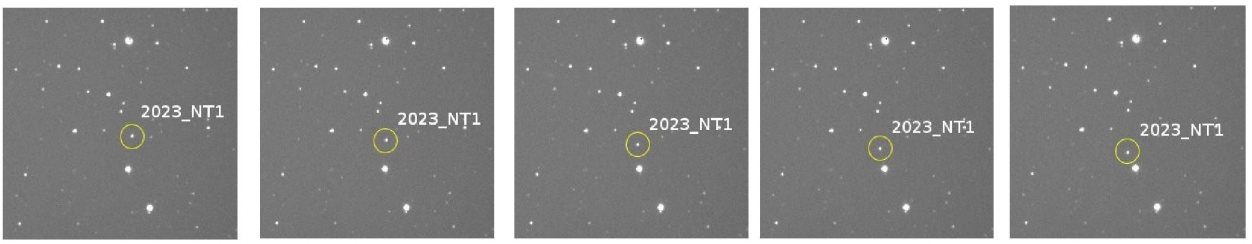

Figure 12: Shown is an example of 5 exposures in the clear filter of an NEA (2023 NT1) that is between 24 - 58 metres, observed when it was 0.262LD from the Earth. The yellow circle indicates the target near the centre of the field of view, with the background stars moving to the right of the page from the first to the last image.

of astrometry.net. It converts the user-selected pixel coordinates (x, y) into sky coordinates (RA, Dec) using the World Coordinate System (WCS) solution from astrometry.net. The script then extracts the mid-exposure time from the FITS headers and formats all the data into a submission file ($MPC\_submission.txt$) for the Minor Planet Centre. A key component is the $get\_calibrated\_mag\_function\_param$ function, which establishes a precise relationship between the instrumental magnitudes measured from the FITS images and their corresponding GAIA catalogue magnitudes. This calibration process begins by creating a scatter plot with error bars showing an initial linear fit between instrumental and GAIA magnitudes. The function then analyses the residuals, removing outliers that differ by more than one magnitude from the preliminary fit. Using this cleaned dataset, it computes a refined linear fit that more accurately maps instrumental magnitudes to catalogue values. Figure 13 shows both the preliminary and final calibration fits, with blue points (including error bars) representing the matched sources, and black lines showing the fits before (dashed) and after (solid) outlier removal. This approach enhances the accuracy of astrometric calibration, crucial for the precise association of detected sources with known objects.

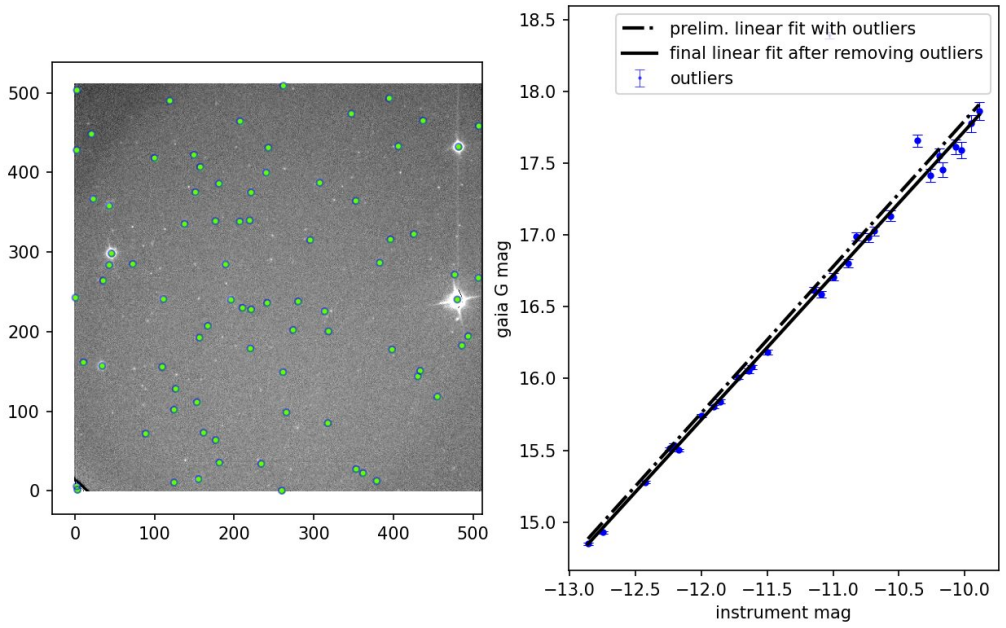

Figure 13: Shown is a scatter plot depicting the preliminary and final linear fits in the calibration process. The blue markers with error bars represent the instrument magnitudes of the detected sources against the corresponding GAIA catalogue magnitudes, revealing outliers in the initial fit. The black dashed line represents the preliminary linear fit, inclusive of outliers, while the blue markers signify the recalibrated data after removing outliers. The solid black line represents the final linear fit, showing the refined alignment between instrument and catalogue magnitudes.

The script relies heavily on astrometry.net (Lang et al. 2012), an open-source software suite that determines precise astrometric solutions for astronomical images. Written in C and Python, astrometry.net can analyse any astronomical image and output its pointing, scale, and orientation through a WCS solution. This solution maps the image's physical pixel coordinates (X, Y) to equatorial coordinates (RA, Dec) in the J2000 epoch. The software's ability to work with images from any telescope or scale makes it particularly valuable for asteroid astrometry, as it can reliably determine the position and orientation of moving objects across varied observing conditions.

2.4.3 Photometry Pipeline

The PHOTOMETRY PIPELINE (PP)[15] is an open-source Python software package used for the photometric calibration of asteroids that were followed up. It automates the process of photometric reduction, enabling the extraction of calibrated magnitudes from images across various filters, ensuring that the data collected is scientifically reliable for further analysis. It was developed by Michael Mommert (Mommert 2017) for automated photometric analysis of imaging data from small to medium-sized observatories and is available on PP's Github repository[16]. It uses Source Extractor and SCAMP to register and photometrically calibrate images based on catalogues that are available online; photometry is measured using Source Extractor aperture photometry. PP was designed for asteroid observations but can also be used on other images.

PP is designed primarily for extracting photometry of moving sources such as asteroids. However, it can also obtain photometric measurements for stationary sources like variable stars and extragalactic objects. It processes FITS files from small- to medium-sized telescopes, providing calibrated photometry with an accuracy of ≤ 0.05 magnitudes. Although PP can work with imaging data from any telescope, users must generate a configuration file that maps the telescope's header information to PP-specific keywords. A template, instructions, and examples are provided to assist in this setup.

PP operates on both Mac and Linux systems, with Ubuntu 16.04 being the recommended and tested platform. It consists of multiple Python scripts, each performing a dedicated function. The required Python modules include numpy[17], scipy[18], astropy[19], astroquery[20], matplotlib[21], Python Future[22], scikit-image[23], and pandas[24]. These scripts can be executed individually via the command line or in sequence with default input parameters using the pp_run command.

For this project, the pp_run command was run first and then 4 individual scripts were run separately to fine-tune input parameters, to get more accurate photometric extraction for each observation.

- `pp_photometry` – Extracts photometric data from FITS images.

[15] `https://photometrypipeline.readthedocs.io/en/latest/`
[16] `https://github.com/mommermi/photometrypipeline`
[17] `https://numpy.org/`
[18] `www.scipy.org`
[19] `https://www.astropy.org/`
[20] `https://github.com/astropy/astroquery`
[21] `https://matplotlib.org/`
[22] `https://python-future.org/`
[23] `https://scikit-image.org/`
[24] `http://pandas.pydata.org/`

- `pp_calibrate` – Calibrates the extracted photometry against known standards.
- `pp_distill` – Distills the photometric measurements into a final result, applying additional filtering and refinement.

In this project, the initial use of the *pp_run* command allowed for a streamlined extraction of photometry across multiple observations with default parameters. However, given the unique characteristics and varying brightness levels of smaller asteroids, a more tailored approach was necessary. The research team proceeded by rerunning each individual step—*pp_prepare*, *pp_register*, *pp_extract*, *pp_photometry*, *pp_calibrate*, and *pp_distill*—which enabled them to adjust the input parameters for each step. This customization allowed for the optimization of photometry extraction specific to the smaller asteroids, ensuring greater accuracy and reliability in the final results. The flexibility of executing the commands individually allowed the team to implement fine-tuning, which proved critical when dealing with objects that exhibited distinct observational challenges compared to larger asteroids.

2.5 Taxonomic Classification Using Photometric Colours

Figure 14 illustrates the methodology used in this study for these Near-Earth Asteroids (NEAs). The remainder of these can be found in Appendix A. These observations involved obtaining photometric data in g, r, and i filters, which allowed for the analysis of each target's spectral features. The combined photometric measurements provided insight into the asteroids' reflectivity across different wavelengths, contributing to their taxonomic classification.

This approach initiates with the use of the PHOTOMETRYPIPELINE[25], yielding three sets of observations corresponding to each filter (g, r, and i).In the initial analysis, pseudo magnitudes were computed by establishing median values for the g and r filters, as well as for the r and i filters, treating frames in these filters as if acquired simultaneously. However, this methodology introduces increased precision by incorporating weighted means. The weighted mean magnitude for each filter was calculated using:

$$\bar{m}_{\text{weighted}} = \frac{\sum_{i=1}^{n} m_i \cdot w_i}{\sum_{i=1}^{n} w_i} \tag{1}$$

where m_i represents individual magnitude measurements and w_i represents the weights. The weights were calculated as the inverse square of the magnitude uncertainties ($w_i = 1/\sigma_i^2$), giving greater importance to measurements with smaller errors. This weighting

[25] `https://photometrypipeline.readthedocs.io/en/latest/`

approach minimizes the influence of lower quality measurements on the final magnitude estimates.

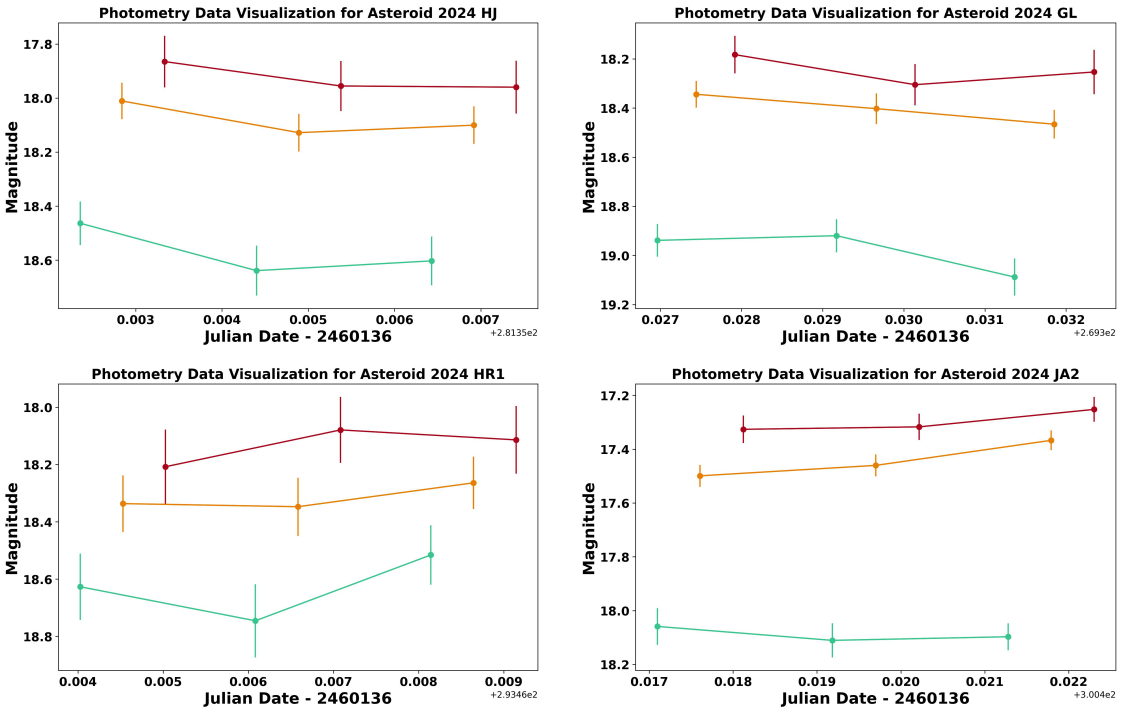

Figure 14: Shows four examples of the photometry data for asteroids 2024 HJ (top left), 2024 GL (top right), 2024 HR1 (bottom left), and 2024 JA2 (bottom right), showing their variation in magnitude over time in three different filters: g-filter (green), r-filter (orange), and i-filter (red). The magnitude represents the brightness of each asteroid, and the error bars in each data point indicate the uncertainties in the observed measurements. The images were taken in a repeating sequence of clear, g, r, i filters.

Subsequently, the weighted mean magnitudes and colour indices ($g - r$ and $r - i$) are computed using this approach, along with error values associated with the colour indices. This step ensures a more accurate representation of the observed data. The final stage of this methodology encompasses the computation of photometric colours as differences between the weighted mean magnitudes, $g - r$ and $r - i$. This contributes to enhanced accuracy in this analysis and aids in a more precise classification of asteroid types within the Bus-DeMeo scheme (DeMeo et al. 2009). Additionally, the inverse-squared magnitude errors are used to compute weighted mean magnitudes for every filter. To take into consideration the various degrees of uncertainty connected to each magnitude measurement in a filter (g, r, or i), the weighted means are computed.

3 Research Outcomes

3.1 Follow-up Observations

In this project, follow-up observations of newly discovered Near Earth Asteroids (NEAs) were conducted with two primary aims: to perform rapid follow-up observations shortly after their discovery and to probe the characteristics of the small NEA population (<300 m). Since the project's initiation in February 2023, a total of 230 NEAs were successfully observed, including 15 Potentially Hazardous Asteroids (PHAs). These were observed using the strategy outlined in Section 2.3. Around 380 automated observations were executed successfully of which 230 produced usable data. The remainder of the observations that were not successful were because of non-optimal observing conditions (e.g. thin cloud or exceptionally bad seeing), the asteroid being too faint to detect in the frames or the telescope was not pointing at the required RA and Dec at the time of the observations. This project builds on previous work by Janse van Rensburg 2021, in which 20 NEAs were successfully observed, including 14 classified as small NEAs (diameter < 300 m, H < 21). This highlights how an automated approach for this work can drastically increase the number of observed targets.

Table 1 summarises all the NEAs observed during this project, including direct links to the official Minor Planet Electronic Circulars (MPECs) for each target where the contributions of this project are officially recorded (see observatory code M28 for Lesedi on the MPECs). This table also shows the discovery dates of the corresponding discovery observatory, with corresponding observatory codes provided in Table 2. By using both the discovery date and the follow-up observation date by the Lesedi telescope, the time taken for follow-up observations is calculated and shown in the days in the 4th column of the table. Figure 15 shows the number of asteroids followed up on versus the time in days and it shows that 61% of these observations occurred within one day of discovery. This time was calculated as the interval between the discoverer's last observation and the first follow-up conducted by the Lesedi telescope. A faster response time is possible; however, it is limited by the timing of submissions by the discoverer to the Minor Planet Center (MPC).

One limitation of this project's follow-up strategy (see Section 2.3) is that asteroids must first be reported to the MPC. This influences the response time, as observations can only happen once the MPC officially registers the discovery. Even with this limitation, some targets were observed in significantly less time; approximately 10% were observed within three hours of discovery, with 2023 QN7 being the fastest at 57.4 minutes. These rapid observations were possible primarily because the NEAs were discovered by observatories geographically close to the Lesedi telescope, such as ATLAS-STH (M22), which shares the South African Astronomical Observatory (SAAO) site, and the Moonbase South Observatory (L87) at Hakos, Namibia, which is located at a relatively similar longitude and

latitude to Lesedi. Another contributing factor is that humans overseeing these discoveries often monitor them in semi-real-time and promptly submit observation data to the Minor Planet Center (MPC). For example, ATLAS benefits from its global network and time zone advantages: when ATLAS-STH observes at night, it is daytime in Hawaii, allowing operators to monitor and respond to ATLAS-STH discoveries during their Hawaii office hours.

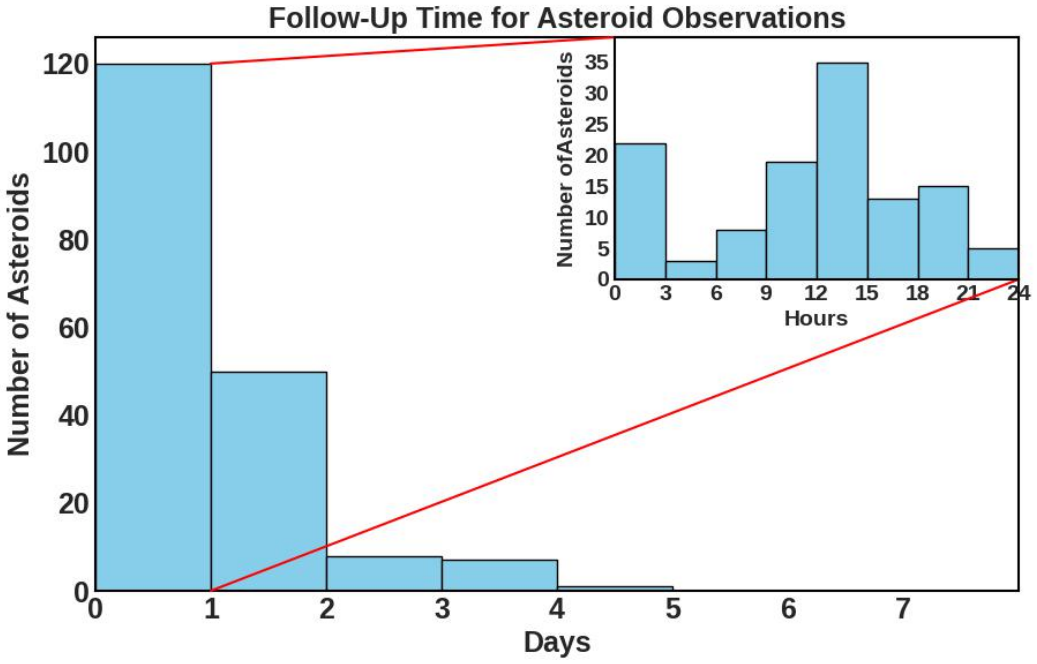

Figure 15: Shows histogram of the distribution of follow-up observation times for asteroids, measured in days after their initial discovery. The x-axis represents the time to follow up which is the difference between the last observation of the discoverer and the first follow-up observation of the Lesedi telescope versus the number of asteroids observed. Approximately 10% of the observations were done within the first 3 hours, with the most being done between 12 and 15 hours at 20%.

Additionally, the table presents the absolute magnitudes (H-magnitude) of the observed NEAs, which range from 19.4 to 28.7. The absolute magnitude values for all observed NEAs were obtained from NASA's JPL Horizons System[26]. The mean absolute magnitude for all the observed asteroids is $H = 24.9$ and a diameter of 25 m to 62 m depending on an assumed albedo of between 0.05 and 0.30. The H-magnitude values were used to estimate

[26] https://ssd.jpl.nasa.gov/horizons/app.html#/

the possible diameters of these objects using the Asteroid Size Estimator[27], which uses the Equation 2. This tool calculates an asteroid's size based on its absolute magnitude (H) and an assumed geometric albedo (a). For this study, diameters were estimated by averaging size values generated using albedos of 0.05 and 0.30. This approach was selected because these values represent the lower and higher limit albedos of a typical very dark C-type and very bright S-type asteroid, which are the most abundant asteroid classes.

The expression derived from the method outlined by Harris 1997, for diameter D in kilometres as a function of absolute magnitude (H-magnitude) and geometric albedo a is given by the following equation:

$$D = 10^{[3.1236 - 0.5 \log_{10}(a) - 0.2H]} \tag{2}$$

Where.

- D = Diameter in kilometres.
- a = Geometric albedo.
- H = Absolute magnitude.

The statement above assumes that an object is spherical and has a uniform surface (no variation in albedo). The value of a is typically assumed based on the spectral class of the asteroid, which corresponds to its composition—e.g., S-type asteroid albedos can range between approximately 0.17 and 0.22 (Binzel et al. 2004).

[27] `https://cneos.jpl.nasa.gov/tools/ast_size_est.html`

Table 1: **Summary of Targets with Completed Follow-up Observations**

NEA Name	MPEC Link	Disc[a]	Time Days[b]	V Mag	H Mag[c]	Approx Size[d] (m)	Orbit Type	Closest Approach Date	Closest Approach Distance (LD)	Skyrate (arcsec /hour)
2023 CK	https://www.minorplanetcenter.net/mpec/K23/K23C35.html	M22	0.07	Apollo	19.2	27.0	16	2023-Jan-30 07:54	0.274	554
2023 DP	https://www.minorplanetcenter.net/mpec/K23/K23D61.html	W68	0.69	Apollo	18.5	25.3	36	2023-Feb-21 10:29	5.65	1696
2023 DT	https://www.minorplanetcenter.net/mpec/K23/K23D65.html	W68	0.67	Apollo	19.4	22.7	120	2023-Feb-15 02:24	32.2	718
2023 ER	https://www.minorplanetcenter.net/mpec/K23/K23E65.html	M22	0.83	Amor	17.6	24.0	67	2023-Mar-09 21:38	2.73	904
2023 ET	https://www.minorplanetcenter.net/mpec/K23/K23E69.html	M22	1.05	Apollo	18.1	26.0	26	2023-Mar-11 07:51	1.34	524
2023 EY	https://www.minorplanetcenter.net/mpec/K23/K23E78.html	M22	0.87	Apollo	19.0	26.8	18	2023-Mar-17 11:35	0.623	355
2023 GG	https://www.minorplanetcenter.net/mpec/K23/K23G39.html	M22	0.11	Aten	None	23.4	91	2023-Apr-11 00:25	111	0
2023 HK2	https://www.minorplanetcenter.net/mpec/K23/K23HB5.html	M22	0.81	Apollo	18.7	20.4	345	2023-Apr-27 12:40	79.9	237
2023 HA8	https://www.minorplanetcenter.net/mpec/K23/K23J65.html	X74	3.57	Apollo	19.6	19.3	585	2023-May-04 10:08	157	192
2023 JN	https://www.minorplanetcenter.net/mpec/K23/K23J90.html	703	1.54	Apollo	19.2	26.2	25	2023-May-08 07:47	6.68	1650
2023 JT	https://www.minorplanetcenter.net/mpec/K23/K23J98.html	G96	0.59	Apollo	19.0	25.6	31	2023-May-07 17:25	8.16	1315
2023 JK	https://www.minorplanetcenter.net/mpec/K23/K23J87.html	F52	0.41	Apollo	20.0	24.8	46	2023-May-21 09:41	4.32	113
2023 KT	https://www.minorplanetcenter.net/mpec/K23/K23K79.html	G03	0.07	Apollo	20.1	28.4	9	2023-May-17 19:35	0.43	253
2023 KF	https://www.minorplanetcenter.net/mpec/K23/K23K60.html	F51	3.39	Amor	19.6	24.5	52	2023-May-26 09:46	17.8	549
1980 DX	No MPEC Link	W68	136	MBA	16.7	13.1	9950	None	None	28
2023 KV3	https://www.minorplanetcenter.net/mpec/K23/K23KH0.html	G96	0.70	Apollo	19.9	28.2	9	2023-May-29 08:43	1.24	1816
2023 KY3	https://www.minorplanetcenter.net/mpec/K23/K23KH3.html	703	0.95	Apollo	20.0	26.1	25	2023-May-25 22:28	6.87	1402
2023 KT3	https://www.minorplanetcenter.net/mpec/K23/K23KG8.html	T05	1.34	Apollo	17.2	23.7	78	2023-May-25 16:00	2.89	783
2023 KG4	https://www.minorplanetcenter.net/mpec/K23/K23KI1.html	I41	3.49	Apollo	19.9	26.4	23	2023-May-24 07:27	2.22	306
2023 KR3	No MPEC Link	L87	1.76	Outer MBA	19.5	17.6	1265	None	None	147
2023 KA4	https://www.minorplanetcenter.net/mpec/K23/K23KH5.html	F51	0.43	Apollo	19.8	24.8	47	2023-May-22 16:05	8.68	583
2023 LQ	https://www.minorplanetcenter.net/mpec/K23/K23L53.html	703	0.51	Amor	18.8	26.0	26	2023-Jun-12 03:41	7	3074
2015 DV315	https://www.minorplanetcenter.net/mpec/K23/K23MD0.html	M22	0.76	Amor	18.5	16.8	1850	2023-Oct-08 21:49	125	52
2023 MB4	https://www.minorplanetcenter.net/mpec/K23/K23MD1.html	M22	0.05	Apollo	19.1	25.4	35	2023-Jun-19 03:31	8.74	860
2023 MG6	https://www.minorplanetcenter.net/mpec/K23/K23N08.html	W68	1.68	Amor, PHA	18.1	20.4	350	2023-Jul-16 21:37	9.46	108
2023 MF6	https://www.minorplanetcenter.net/mpec/K23/K23N06.html	W68	1.65	Apollo	16.7	23.0	106	2023-Jul-02 12:40	8.68	1953
2023 MH6	https://www.minorplanetcenter.net/mpec/K23/K23N09.html	M22	0.87	Apollo	18.1	25.2	38	2023-Jun-29 03:35	1.74	812
2023 NA1	https://www.minorplanetcenter.net/mpec/K23/K23N52.html	G96	0.61	Amor	19.5	24.0	68	2023-Jul-08 09:15	21.5	1009
2023 NE1	https://www.minorplanetcenter.net/mpec/K23/K23N61.html	M22	1.90	Amor	18.3	23.9	71	2023-Jul-19 17:44	12.7	801
2023 NR1	https://www.minorplanetcenter.net/mpec/K23/K23N78.html	W68	0.76	Apollo	17.8	23.3	92	2023-Jul-22 00:42	2.91	161
2012 YF8	No MPEC Link	L87	0.15	Apollo	None	22.3	145	2023-Jul-01 22:52	18.9	0
2023 NQ1	https://www.minorplanetcenter.net/mpec/K23/K23N77.html	W68	1.51	Apollo	19.6	23.1	94	2023-Jul-06 22:28	18.5	347
2023 NP1	No MPEC Link	W68	1.58	MCA	19.4	20.3	360	2023-Jul-17 19:23	145	230
2023 NS	No MPEC Link	703	1.51	MCA	18.2	18.3	920	2023-Jul-16 09:50	151	317
2023 NT1	https://www.minorplanetcenter.net/mpec/K23/K23O01.html	M22	0.80	Apollo	17.4	25.1	41	2023-Jul-13 10:13	0.262	163
2023 OA	https://www.minorplanetcenter.net/mpec/K23/K23O12.html	F52	0.49	Apollo	18.7	26.5	21	2023-Jul-19 13:00	6.15	1616
2023 OV	https://www.minorplanetcenter.net/mpec/K23/K23O44.html	M22	0.90	Amor	18.3	18.9	695	2023-Jul-28 09:15	97.4	288
2023 OU3	https://www.minorplanetcenter.net/mpec/K23/K23O97.html	M22	0.09	Apollo	19.5	25.9	28	2023-Mar-22 02:25	113	391
2023 OV1	https://www.minorplanetcenter.net/mpec/K23/K23O75.html	M22	0.09	Apollo	19.4	25.4	35	2023-Jul-21 11:58	1.43	422
2012 YJ7	https://www.minorplanetcenter.net/mpec/K23/K23O69.html	W68	1.63	Apollo	17.6	22.5	134	2023-Jul-19 09:26	6.99	415
2023 OV3	https://www.minorplanetcenter.net/mpec/K23/K23O98.html	M22	1.98	Apollo	19.3	19.4	555	2023-Aug-16 07:21	67.8	188
2023 PF	https://www.minorplanetcenter.net/mpec/K23/K23P41.html	W68	0.54	Amor	18.7	22.6	127	2023-Aug-06 03:26	40.6	618
2023 PJ	https://www.minorplanetcenter.net/mpec/K23/K23P44.html	L87	0.79	Apollo	19.6	21.7	190	2023-Aug-25 21:06	62.8	252
2023 NB7	No MPEC Link	F51	15.2	MCA	19.6	19.4	545	None	None	61
2023 PR	https://www.minorplanetcenter.net/mpec/K23/K23P55.html	M22	0.76	Apollo	18.1	24.6	51	2023-Aug-06 12:43	6.07	1016
2023 PX	https://www.minorplanetcenter.net/mpec/K23/K23P66.html	L87	0.04	Aten	19.5	25.6	32	2023-Aug-15 23:30	12.9	932
2023 QB	https://www.minorplanetcenter.net/mpec/K23/K23Q11.html	M22	0.07	Apollo, PHA	17.3	20.8	290	2023-Aug-11 12:16	23.3	966
2023 QW	https://www.minorplanetcenter.net/mpec/K23/K23Q39.html	F51	0.57	Apollo	19.6	26.0	26	2023-Aug-23 14:37	4.20	724
2023 OZ12	No MPEC Link	F51	24.3	MBA	19.7	18.1	995	None	None	70
2007 RR17	https://www.minorplanetcenter.net/mpec/K23/K23QA7.html	W68	0.41	Amor	17.2	23.8	72	2023-Aug-26 15:54	8.31	1224
2023 QW3	https://www.minorplanetcenter.net/mpec/K23/K23QA3.html	F51	3.31	Apollo	19.8	23.9	69	2023-Aug-13 03:47	26.4	389
2023 QT7	https://www.minorplanetcenter.net/mpec/K23/K23R02.html	W68	0.57	Amor	19.8	21.6	195	2023-Aug-27 21:01	55.5	269
2023 QN7	https://www.minorplanetcenter.net/mpec/K23/K23QG1.html	M22	0.04	Aten	17.5	23.6	79	2023-Aug-24 20:42	4.21	1347
2023 QC7	https://www.minorplanetcenter.net/mpec/K23/K23QF2.html	W68	0.63	Apollo	17.6	23.2	98	2023-Aug-23 04:26	8.59	926
2023 RH	https://www.minorplanetcenter.net/mpec/K23/K23R27.html	G96	0.60	Apollo	18.2	25.5	33	2023-Sep-08 18:15	4.25	1810
2023 RN3	https://www.minorplanetcenter.net/mpec/K23/K23RB5.html	T05	2.28	Centaur	18.0	10.9	28000	None	None	15
2023 RF1	https://www.minorplanetcenter.net/mpec/K23/K23R55.html	M22	0.05	Apollo	17.3	25.8	29	2023-Sep-04 19:33	2.43	1927
2023 RR1	https://www.minorplanetcenter.net/mpec/K23/K23R63.html	G96	1.59	Amor	19.8	24.1	62	2023-Sep-16 10:37	35.7	309
2023 RC8	https://www.minorplanetcenter.net/mpec/K23/K23RJ3.html	F51	0.24	Aten, PHA	19.6	21.8	175	2023-Sep-05 09:36	61.1	478

2023 RS7	https://www.minorplanetcenter.net/mpec/K23/K23RI3.html	F52	0.31	Amor	20.4	24.3	58	2023-Sep-07 14:42	38.3	537
2023 RA8	https://www.minorplanetcenter.net/mpec/K23/K23RJ1.html	F51	1.56	Apollo	20.1	25.6	33	2023-Sep-20 10:07	15.4	612
2023 RH9	https://www.minorplanetcenter.net/mpec/K23/K23RK4.html	F51	0.43	Amor	20.3	23.6	79	2023-Sep-20 14:10	43.0	368
2023 RN6	No MPEC Link	F52	4.34	MCA	19.5	18.1	990	None	None	12
2023 RC8	https://minorplanetcenter.net/mpec/K23/K23RJ3.html	F51	0.24	Aten, PHA	19.6	21.8	175	2023-Sep-05 09:36	61.1	478
2023 RR7	https://www.minorplanetcenter.net/mpec/K23/K23RI2.html	F52	4.44	Aten	20.7	24.9	45			510
2023 RY7	https://minorplanetcenter.net/mpec/K23/K23RI7.html	L87	0.96	Apollo	19.0	25.6	31	2023-Sep-16 14:21	13.7	1281
2023 RW9	https://www.minorplanetcenter.net/mpec/K23/K23RL8.html	W68	0.83	Apollo	18.9	22.1	162	2023-Sep-11 05:34	39.8	827
2023 RO9	https://www.minorplanetcenter.net/mpec/K23/K23RL0.html	F52	0.57	Apollo	20.3	25.9	28	2023-Sep-17 19:48	13.1	1064
2021 VO	https://www.minorplanetcenter.net/mpec/K23/K23RN4.html	F52	0.34	Amor	19.9	21.3	225	2023-Oct-13 01:25	42.3	96
2023 RV9	https://www.minorplanetcenter.net/mpec/K23/K23RL7.html	M22	0.08	Amor	19.2	24.9	45	2023-Sep-18 11:38	10.1	920
2023 SJ	https://www.minorplanetcenter.net/mpec/K23/K23S50.html	703	1.64	Apollo	19.2	24.2	62	2023-Sep-21 11:23	16.844	1173
2023 SP	https://www.minorplanetcenter.net/mpec/K23/K23S61.html	W68	0.82	Apollo	19.7	19.7	470	2023-Sep-14 21:28	2.252	526
2023 SU	https://www.minorplanetcenter.net/mpec/K23/K23S65.html	F51	0.49	Amor	20.7	24.1	66	2023-Oct-31 16:11	20.734	81
2023 SG	https://www.minorplanetcenter.net/mpec/K23/K23S48.html	F51	1.65	Aten	20.3	26.6	21	2023-Sep-13 20:38	9.787	1000
2023 SE	https://www.minorplanetcenter.net/mpec/K23/K23S46.html	F52	1.66	Apollo	20.2	25.8	30	2023-Sep-13 11:26	8.687	834
2023 SB1	https://www.minorplanetcenter.net/mpec/K23/K23S79.html	703	0.58	Apollo	18.8	28.3	9	2023-Sep-19 18:43	1.215	2886
2023 ST	https://www.minorplanetcenter.net/mpec/K23/K23S64.html	F52	2.49	Apollo	19.4	26.1	26	2023-Sep-21 01:39	2.129	674
2008 AR31	No MPEC Link	703	0.51	Inner MBA	19.9	16.9	1700	None	None	46
2023 SV1	https://www.minorplanetcenter.net/mpec/K23/K23SA3.html	F51	1.25	Apollo	19.6	24.1	64	2023-Sep-13 11:07	6.256	297
2023 SJ4	https://www.minorplanetcenter.net/mpec/K23/K23SG2.html	F52	0.56	Apollo	20.1	25.3	37	2023-Sep-15 15:33	9.149	716
2023 SZ3	https://www.minorplanetcenter.net/mpec/K23/K23SF2.html	M22	2.90	Apollo	18.6	24.1	65	2023-Sep-18 04:32	11.344	1141
2023 SL5	https://www.minorplanetcenter.net/mpec/K23/K23SI7.html	703	0.51	Aten	19.9	28.7	8	2023-Sep-20 07:53	0.135	175
2023 SY3	https://www.minorplanetcenter.net/mpec/K23/K23SF1.html	F52	1.50	Apollo	20.1	26.9	17	2023-Sep-26 01:21	3.417	668
2023 SK4	https://www.minorplanetcenter.net/mpec/K23/K23SG3.html	703	0.55	Apollo	19.5	24.8	44	2023-Sep-15 06:17	12.017	602
2023 SM5	https://www.minorplanetcenter.net/mpec/K23/K23SI8.html	F52	2.32	Aten	18.2	26.5	21	2023-Sep-23 11:14	0.979	1246
2023 SL8	https://www.minorplanetcenter.net/mpec/K23/K23T02.html	M22	1.81	Apollo	15.7	24.4	56	2023-Sep-30 09:02	2.014	2229
2013 TG6	https://www.minorplanetcenter.net/mpec/K23/K23T14.html	703	0.45	Aten	18.7	26.6	20	2023-Sep-28 22:21	3.530	887
1999 JW3	No MEPC	M22	7.99	Apollo	18.8	18.8	705	2023-Oct-17 13:20	79.257	150
2023 TM14	https://www.minorplanetcenter.net/mpec/K23/K23TQ0.html	G96	0.57	Amor	19.7	26.6	20	2023-Oct-19 07:07	8.226	1077
2023 TQ16	https://www.minorplanetcenter.net/mpec/K23/K23U31.html	G96	1.69	Amor	20.0	21.2	240	2023-Oct-17 16:22	94.445	321
2023 TG14	https://www.minorplanetcenter.net/mpec/K23/K23TP9.html	F51	2.35	Apollo	20.4	25.8	29	2023-Oct-26 01:03	4.135	197
2023 TO17	https://www.minorplanetcenter.net/mpec/K23/K23U36.html	703	0.60	Apollo	20.4	24.5	54	2023-Oct-14 14:35	0.141	394
2023 TR15	https://www.minorplanetcenter.net/mpec/K23/K23U09.html	703	0.65	Apollo	18.7	28.0	11	2023-Oct-16 09:35	3.430	4485
2023 TP15	https://www.minorplanetcenter.net/mpec/K23/K23U07.html	703	0.67	Apollo	19.1	26.0	27	2023-Oct-13 14:20	2.902	835
2023 TQ16	https://www.minorplanetcenter.net/mpec/K23/K23U31.html	G96	1.69	Amor	20.0	21.2	240	2023-Oct-17 16:22	94.441	321
2023 TB17	https://www.minorplanetcenter.net/mpec/K23/K23U35.html	G96	0.64	Amor	20.0	21.9	175	2023-Oct-16 13:35	60.439	392
2023 UT	https://www.minorplanetcenter.net/mpec/K23/K23U76.html	L87	0.73	Amor	19.6	21.8	185	2023-Nov-7 05:26	32.327	145
2023 UZ1	https://www.minorplanetcenter.net/mpec/K23/K23UB5.html	F51	0.37	Aten	20.1	22.8	114	2023-Oct-13 08:30	52.516	755
2023 UW	https://www.minorplanetcenter.net/mpec/K23/K23U80.html	F51	0.35	Aten	20.2	28.0	11	2023-Oct-21 05:10	4.190	1394
2023 UP	https://www.minorplanetcenter.net/mpec/K23/K23U64.html	F51	1.53	Apollo	19.6	28.0	11	2023-Oct-19 17:29	2.650	1727
2023 UR1	https://www.minorplanetcenter.net/mpec/K23/K23UA7.html	M22	0.12	Apollo	18.8	24.8	47	2023-Oct-21 01:17	2.169	835
2001 UB5	https://www.minorplanetcenter.net/mpec/K23/K23U51.html	F51	1.41	Amor	19.5	21.9	175	2023-Oct-22 03:27	51.246	622
2023 UD3	https://www.minorplanetcenter.net/mpec/K23/K23UF0.html	M22	2.79	Amor	19.4	19.5	535	2023-Oct-26 21:52	142.292	222
2023 UF3	https://www.minorplanetcenter.net/mpec/K23/K23UF2.html	703	0.52	Apollo	19.0	27.2	15	2023-Oct-18 18:32	4.320	2010
2023 UN7	https://www.minorplanetcenter.net/mpec/K23/K23UM9.html	703	0.50	Apollo	18.5	24.1	62	2023-Oct-24 16:52	15.302	1730
2023 UN10	https://www.minorplanetcenter.net/mpec/K23/K23UT6.html	F52	0.37	Apollo	19.5	24.1	64	2023-Oct-23 18:41	15.183	597
2023 UC11	https://www.minorplanetcenter.net/mpec/K23/K23V16.html	F52	15.4	Amor	19.3	21.6	200	2023-Nov-17 06:15	27.718	242
2023 VF	https://www.minorplanetcenter.net/mpec/K23/K23V18.html	G96	0.47	Apollo	19.6	23.4	85	2023-Nov-16 03:38	21.689	289
2004 VZ14	https://www.minorplanetcenter.net/mpec/K23/K23V11.html	703	1.65	Apollo	18.0	25.3	37	2023-Nov-01 13:49	3.471	1407
2023 VW1	https://www.minorplanetcenter.net/mpec/K23/K23V69.html	703	0.62	Aten	18.5	24.6	50	2023-Nov-3 14:37	2.441	1381
2023 VY1	https://www.minorplanetcenter.net/mpec/K23/K23V71.html	703	0.62	Apollo	19.8	25.0	42	2023-Nov-13 10:43	8.826	487
2023 VX1	https://www.minorplanetcenter.net/mpec/K23/K23V70.html	703	0.53	Apollo	19.3	25.4	35	2023-Nov-1 20:35	10.170	960
2023 VE3	https://www.minorplanetcenter.net/mpec/K23/K23VA6.html	703	0.53	Apollo	18.9	26.9	17	2023-Nov-5 23:03	1.162	1009
2023 VZ2	https://www.minorplanetcenter.net/mpec/K23/K23VA1.html	703	0.66	Aten	18.1	26.9	18	2023-Nov-8 20:29	5.612	3360
2023 VN3	https://www.minorplanetcenter.net/mpec/K23/K23VB7.html	G96	3.58	Apollo	19.9	25.0	42	2023-Nov-2 15:26	11.810	641
2023 VR4	https://www.minorplanetcenter.net/mpec/K23/K23VE8.html	W68	0.74	Aten	18.8	23.0	106	2023-Nov-14 07:03	17.883	772
2023 VV4	https://www.minorplanetcenter.net/mpec/K23/K23VF2.html	F52	1.34	Amor	19.7	22.3	147	2023-Nov-15 05:43	52.194	474
2023 VK7	https://www.minorplanetcenter.net/mpec/K23/K23VL4.html	G96	0.67	Apollo	19.2	22.7	120	2023-Nov-9 10:20	21.863	1458
2023 VE6	https://www.minorplanetcenter.net/mpec/K23/K23VI1.html	703	0.48	Apollo	18.4	27.1	16	2023-Nov-9 05:18	1.933	2123
2023 VN7	https://www.minorplanetcenter.net/mpec/K23/K23VL6.html	W68	0.54	Aten	18.5	25.5	33	2023-Nov-12 20:20	5.680	1646
2023 VB8	https://www.minorplanetcenter.net/mpec/K23/K23VM7.html	G96	0.53	Apollo	20.0	20.8	290	2023-Nov-8 03:13	105.364	422
2023 VC8	https://www.minorplanetcenter.net/mpec/K23/K23VM8.html	G96	0.66	Apollo	20.2	23.0	106	2023-Oct-20 19:26	28.953	218

2023 VY7	https://www.minorplanetcenter.net/mpec/K23/K23VM4.html	T05	0.55	Aten	19.8	23.3	92	2023-Nov-19 13:19	19.593	564
2023 VP7	https://www.minorplanetcenter.net/mpec/K23/K23VL8.html	703	1.66	Apollo	19.3	23.4	91	2023-Nov-16 22:03	23.710	701
2023 WR2	https://www.minorplanetcenter.net/mpec/K23/K23WA8.html	703	1.38	Apollo	19.3	22.5	133	2023-Nov-14 10:25	22.372	430
2023 XM1	https://www.minorplanetcenter.net/mpec/K23/K23X74.html	703	0.56	Apollo	17.8	24.5	54	2023-Dec-02 16:06	8.016	1946
2023 XO3	https://www.minorplanetcenter.net/mpec/K23/K23XD8.html	M22	2.03	Apollo	18.8	27.5	13	2023-Dec-03 09:26	1.360	2411
2020 KT4	https://www.minorplanetcenter.net/mpec/K23/K23X38.html	G96	1.57	Apollo	18.7	23.3	92	2023-Dec-25 19:59	13.317	154
2023 XU2	https://www.minorplanetcenter.net/mpec/K23/K23XB7.html	F51	0.33	Apollo	19.9	25.3	37	2023-Dec-01 19:24	11.429	788
2023 XD4	https://www.minorplanetcenter.net/mpec/K23/K23XE5.html	G96	1.43	Amor	19.8	20.3	365	2023-Dec-22 03:42	108.409	224
2023 XM3	No MPEC Link	F51	0.49	MCA	19.8	18.3	920	1983-Dec-03 20:26	189.741	119
2023 XS3	https://www.minorplanetcenter.net/mpec/K23/K23XD9.html	F52	1.41	Apollo	19.9	26.1	26	2023-Dec-09 03:49	11.860	994
2023 XC4	https://www.minorplanetcenter.net/mpec/K23/K23XE4.html	F51	1.27	Apollo	20.2	25.2	38	2023-Nov-30 07:26	9.755	377
2023 XR10	https://www.minorplanetcenter.net/mpec/K23/K23XN7.html	F51	0.52	Apollo	20.7	20.6	325	2023-Nov-15 16:47	101.510	209
2023 XR12	https://www.minorplanetcenter.net/mpec/K23/K23XR4.html	F51	1.42	Apollo, PHA	20.2	20.6	315	2023-Dec-27 09:58	43.373	187
2023 XV5	https://www.minorplanetcenter.net/mpec/K23/K23XH6.html	G96	3.64	Amor	20.5	24.5	52	2023-Dec-24 03:26	30.065	265
2023 XX10	https://www.minorplanetcenter.net/mpec/K23/K23XO4.html	W68	1.72	Apollo	19.1	21.1	255	2023-Nov-30 21:34	35.871	426
2023 XY10	https://www.minorplanetcenter.net/mpec/K23/K23XO5.html	703	1.65	Apollo, PHA	18.1	21.3	235	2023-Dec-09 21:57	28.702	1251
2023 XN10	https://www.minorplanetcenter.net/mpec/K23/K23XN3.html	F52	0.59	Apollo	20.3	23.6	78	2023-Dec-23 15:22	18.314	340
2023 XZ11	https://www.minorplanetcenter.net/mpec/K23/K23XQ4.html	F51	1.49	Apollo	19.4	25.2	39	2023-Dec-15 03:12	3.655	1555
2024 AV4	https://www.minorplanetcenter.net/mpec/K24/K24B16.html	703	0.62	Apollo	19.0	25.3	36	2024-Jan-17 12:35	8.634	2471
2024 CO1	https://www.minorplanetcenter.net/mpec/K24/K24C89.html	M22	1.94	Apollo	18.6	20.3	365	2024-Feb-11 03:40	43.054	1032
2018 CY2	https://www.minorplanetcenter.net/mpec/K24/K24C94.html	T05	0.49	Apollo	18.4	22.5	135	2024-Feb-14 16:34	21.871	736
2024 CO2	https://www.minorplanetcenter.net/mpec/K24/K24CC4.html	M22	0.08	Apollo	19.2	26.8	18	2024-Feb-08 18:51	1.481	993
2024 CR2	https://www.minorplanetcenter.net/mpec/K24/K24CC6.html	M22	0.07	Apollo	19.2	23.9	71	2024-Feb-05 12:47	12.318	668
2024 CG2	https://www.minorplanetcenter.net/mpec/K24/K24CB8.html	M22	0.07	Apollo	15.9	23.1	100	2024-Feb-08 03:42	2.592	1052
2024 CK3	https://www.minorplanetcenter.net/mpec/K24/K24CE7.html	M22	1.10	Amor	19.1	24.7	47	2024-Feb-14 05:24	17.488	823
2024 CD4	https://www.minorplanetcenter.net/mpec/K24/K24CF5.html	T05	0.45	Apollo	17.5	26.6	20	2024-Feb-13 05:17	4.336	2693
2024 CG4	https://www.minorplanetcenter.net/mpec/K24/K24CF8.html	T05	0.45	Aten	18.5	23.7	78	2024-Feb-13 01:57	21.793	1628
2024 EC	https://www.minorplanetcenter.net/mpec/K24/K24E14.html	F51	0.49	Apollo	18.8	24.0	65	2024-Feb-22 09:05	11.744	376
2024 ER	https://www.minorplanetcenter.net/mpec/K24/K24E32.html	703	1.59	Apollo, PHA	18.4	21.4	220	2024-Mar-02 01:28	22.861	1009
2024 EJ1	https://www.minorplanetcenter.net/mpec/K24/K24E61.html	703	0.60	Amor	19.3	20.4	345	2024-Feb-29 18:57	135.409	249
2024 EQ1	https://www.minorplanetcenter.net/mpec/K24/K24E68.html	703	0.59	Apollo	18.7	25.1	40	2024-Mar-09 12:07	6.555	923
2024 EN2	https://www.minorplanetcenter.net/mpec/K24/K24EB7.html	I41	1.59	Apollo	19.5	26.5	21	2024-Mar-04 15:49	1.980	763
2024 EP3	https://www.minorplanetcenter.net/mpec/K24/K24EG7.html	703	0.49	Apollo	19.6	24.7	48	2024-Mar-17 23:30	11.009	713
2024 EH3	https://www.minorplanetcenter.net/mpec/K24/K24EF8.html	703	0.47	Apollo	18.3	25.5	34	2024-Mar-14 16:16	6.491	1454
2024 ER4	https://www.minorplanetcenter.net/mpec/K24/K24F03.html	M22	0.11	Aten	18.9	27.4	14	2024-Mar-17 09:14	0.421	254
2024 EU4	https://www.minorplanetcenter.net/mpec/K24/K24F08.html	M22	0.11	Apollo	19.1	22.1	156	2024-Mar-23 12:53	18.848	493
2024 GL	https://www.minorplanetcenter.net/mpec/K24/K24G52.html	M22	0.85	Apollo	18.4	24.9	45	2024-Mar-31 14:21	4.737	559
2024 GO	https://www.minorplanetcenter.net/mpec/K24/K24G56.html	G96	0.47	Apollo	18.6	26.5	21	2024-Apr-05 17:07	2.173	2922
2024 GS3	https://www.minorplanetcenter.net/mpec/K24/K24GF9.html	703	1.58	Apollo	19.1	25.3	38	2024-Apr-08 01:20	10.300	1072
2024 HJ	https://www.minorplanetcenter.net/mpec/K24/K24H29.html	F52	0.35	Apollo, PHA	18.3	21.0	265	2024-Apr-26 16:24	33.348	380
2024 HR1	https://www.minorplanetcenter.net/mpec/K24/K24H92.html	G96	0.57	Amor	18.3	23.1	100	2024-Apr-28 01:02	28.829	694
2024 HT1	https://www.minorplanetcenter.net/mpec/K24/K24H94.html	W68	1.71	Apollo	17.9	24.5	52	2024-Apr-26 12:09	0.935	229
2024 HR1	https://www.minorplanetcenter.net/mpec/K24/K24H92.html	G96	0.57	Amor	18.5	23.1	100	2024-Apr-28 01:02	28.829	678
2024 JA2	https://www.minorplanetcenter.net/mpec/K24/K24J88.html	G96	3.52	Apollo	17.7	24.2	62	2024-May-03 02:17	3.340	671
2024 JZ6	https://www.minorplanetcenter.net/mpec/K24/K24JM7.html	W68	0.69	Apollo, PHA	18.3	20.7	305	2024-May-23 14:09	14.551	159
2024 JW16	https://www.minorplanetcenter.net/mpec/K24/K24JT8.html	W68	1.74	Apollo, PHA	18.3	20.9	275	2024-May-16 20:37	32.454	871
2024 KO1	https://www.minorplanetcenter.net/mpec/K24/K24LO2.html	G96	0.43	Amor	19.3	27.2	16	2024-Jun-01 11:21	7.220	1778
2024 LN2	https://www.minorplanetcenter.net/mpec/K24/K24L99.html	W68	1.56	Amor	19.4	20.3	375	2024-Jul-08 03:10	91.739	59
2024 LH3	https://www.minorplanetcenter.net/mpec/K24/K24LB9.html	G96	0.42	Apollo	18.6	24.4	57	2024-Jun-16 21:52	12.950	638
2024 LM4	No MPEC Link	G96	2.44	MBA	20.0	16.7	1900	None	None	38
2024 LS4	https://www.minorplanetcenter.net/mpec/K24/K24LE2.html	F51	0.43	Amor	19.5	26.0	26	2024-Jun-15 23:21	11.103	765
2024 LM5	No MPEC Link	L87	0.19	MCA	18.1	16.8	1850	None	None	90
2024 ME2	https://www.minorplanetcenter.net/mpec/K24/K24N21.html	M22	0.87	Apollo	18.7	23.8	71	2024-Jun-27 06:55	9.918	3913
2024 NC	https://www.minorplanetcenter.net/mpec/K24/K24N24.html	M22	1.73	Aten	19.2	25.0	43	2024-Jul-02 16:43	13.555	825
2002 MR3	https://www.minorplanetcenter.net/mpec/K24/K24N77.html	F52	1.46	Apollo, PHA	19.0	21.4	220	2024-Jul-01 14:34	30.910	939
2024 OM1	https://minorplanetcenter.net/mpec/K24/K24OB1.html	L87	1.84	Apollo	18.9	24.3	57	2024-Aug-06 21:40	3.640	183
2024 OO1	https://minorplanetcenter.net/mpec/K24/K24OB3.html	W68	1.56	Apollo	19.2	24.8	47	2024-Jul-29 14:48	14.387	1262
2024 OJ2	https://www.minorplanetcenter.net/mpec/K24/K24P24.html	F51	1.37	Amor	19.3	25.0	43	2024-Aug-03 22:15	18.637	1002
2024 OM1	https://www.minorplanetcenter.net/mpec/K24/K24OB1.html	F51	1.84	Apollo	18.1	24.3	57	2024-Aug-06 21:40	3.640	404
2024 PA	https://www.minorplanetcenter.net/mpec/K24/K24P31.html	M22	0.10	Amor	19.1	25.0	43	2024-Aug-02 19:16	17.604	849
2024 PC	https://www.minorplanetcenter.net/mpec/K24/K24P34.html	M22	0.84	Apollo	18.5	26.4	22	2024-Jul-30 11:57	3.187	1086
2024 PW	https://www.minorplanetcenter.net/mpec/K24/K24P67.html	F51	0.33	Apollo	19.3	22.0	170	2024-Aug-08 11:26	33.105	648
2024 PC2	https://www.minorplanetcenter.net/mpec/K24/K24P96.html	M22	0.08	Apollo	17.0	22.3	142	2024-Jul-31 22:58	5.542	707

2024 PJ2	https://www.minorplanetcenter.net/mpec/K24/K24PA9.html	L87	0.06	Amor	19.6	22.0	169	2024-Sep-06 15:50	34.140	128
2024 PF6	https://www.minorplanetcenter.net/mpec/K24/K24Q03.html	T08	2.47	Amor	18.4	25.2	38	2024-Aug-13 23:00	3.161	1873
2024 QK	https://www.minorplanetcenter.net/mpec/K24/K24Q41.html	W68	0.52	Apollo	18.6	24.2	38	2024-Aug-28 04:23	18.886	1142
2024 QK1	https://www.minorplanetcenter.net/mpec/K24/K24Q76.html	W68	1.66	Apollo	18.6	25.3	37	2024-Sep-01 15:51	8.296	1517
2024 QS1	https://www.minorplanetcenter.net/mpec/K24/K24Q85.html	M22	0.81	Apollo	18.9	22.1	161	2024-Sep-12 06:03	12.028	195
2024 QV1	https://www.minorplanetcenter.net/mpec/K24/K24Q89.html	K88	1.86	Apollo	17.9	24.8	47	2024-Sep-03 23:37	5.463	1184
2024 QK2	https://www.minorplanetcenter.net/mpec/K24/K24R15.html	W68	0.60	Apollo	17.9	25.6	32	2024-Aug-29 04:15	4.028	1517
2024 RN3	https://www.minorplanetcenter.net/mpec/K24/K24RA7.html	W68	0.60	Apollo	19.2	26.5	21	2024-Sep-09 19:55	1.780	412
2024 RW4	https://www.minorplanetcenter.net/mpec/K24/K24RE7.html	M22	0.09	Amor	18.7	24.9	44	2024-Sep-11 12:57	8.614	756
2024 RH6	https://www.minorplanetcenter.net/mpec/K24/K24RH7.html	L87	365	Apollo	19.7	28.6	8	2024-Sep-07 10:36	0.559	842
2024 RL10	https://www.minorplanetcenter.net/mpec/K24/K24RN3.html	F51	367	Apollo	19.3	27.5	13	2024-Sep-14 00:24	3.881	1392
2024 RU8	https://www.minorplanetcenter.net/mpec/K24/K24RK5.html	703	1.59	Amor	18.5	24.0	66	2024-Sep-08 11:07	11.988	1938
2024 RT12	https://www.minorplanetcenter.net/mpec/K24/K24RQ7.html	703	365	Amor	19.0	26.0	27	2024-Sep-12 07:05	10.202	1303
2024 SQ	https://www.minorplanetcenter.net/mpec/K24/K24S51.html	G96	0.53	Apollo	18.8	25.8	28	2024-Sep-28 08:11	3.221	671
2024 RV50	https://www.minorplanetcenter.net/mpec/K24/K24SB6.html	F51	25.3	Apollo, PHA	19.1	21.1	255	2024-Oct-18 17:02	19.296	112
2024 SA7	https://www.minorplanetcenter.net/mpec/K24/K24T16.html	F51	2.46	Apollo	19.5	27.3	15	2024-Sep-28 01:53	4.759	823
2024 TE	https://www.minorplanetcenter.net/mpec/K24/K24T45.html	703	0.56	Apollo	18.6	27.2	15	2024-Oct-03 12:59	3.389	2241
2024 TA	https://www.minorplanetcenter.net/mpec/K24/K24T24.html	703	0.55	Apollo	19.5	28.2	9	2024-Sep-29 04:49	0.967	951
2024 TY	https://www.minorplanetcenter.net/mpec/K24/K24T68.html	F52	1.35	Apollo	19.7	26.1	26	2024-Oct-07 04:54	1.756	381
2024 TE3	https://www.minorplanetcenter.net/mpec/K24/K24TE1.html	703	0.54	Apollo	19.7	26.2	24	2024-Oct-01 04:52	3.936	798
2024 TS2	https://www.minorplanetcenter.net/mpec/K24/K24TC8.html	T05	0.41	Apollo	18.2	27.0	16	2024-Oct-04 11:06	0.498	539
2024 TU3	https://www.minorplanetcenter.net/mpec/K24/K24TG0.html	M22	0.92	Apollo	19.7	28.1	10	2024-Oct-03 15:02	0.260	536
2024 TY1	https://www.minorplanetcenter.net/mpec/K24/K24TA1.html	F52	0.50	Aten	19.5	23.8	71	2024-Oct-08 11:31	24.873	662
2024 TL5	https://www.minorplanetcenter.net/mpec/K24/K24TI5.html	703	0.53	Aten	19.3	27.7	12	2024-Oct-05 09:45	4.832	1727
2024 TK7	https://www.minorplanetcenter.net/mpec/K24/K24TL7.html	G96	1.54	Apollo	19.1	24.1	64	2024-Oct-07 15:41	18.825	872
2024 TV8	https://www.minorplanetcenter.net/mpec/K24/K24TM8.html	703	0.53	Apollo	17.8	26.3	23	2024-Oct-08 05:20	1.439	1466
2024 TZ11	https://www.minorplanetcenter.net/mpec/K24/K24TQ6.html	703	0.64	Apollo	18.2	23.5	84	2024-Oct-09 15:23	18.490	1722
2024 TB22	https://www.minorplanetcenter.net/mpec/K24/K24U13.html	M22	2.08	Apollo, PHA	16.0	19.2	605	2024-Oct-18 01:51	29.730	1387
2024 UK	https://www.minorplanetcenter.net/mpec/K24/K24U38.html	W68	1.68	Apollo	18.7	24.5	52	2024-Oct-19 12:10	2.016	572
2024 US	https://www.minorplanetcenter.net/mpec/K24/K24U51.html	703	0.56	Apollo	18.2	28.0	11	2024-Oct-22 01:07	0.943	1149
2024 UR5	https://www.minorplanetcenter.net/mpec/K24/K24UI1.html	I41	0.59	Apollo	18.9	25.1	40	2024-Oct-23 03:08	5.589	2343
2024 UJ8	https://www.minorplanetcenter.net/mpec/K24/K24UN2.html	703	1.64	Apollo	19.5	19.9	435	2046-Oct-10 23:04	33.256	239
2024 UT7	https://www.minorplanetcenter.net/mpec/K24/K24UM1.html	W57	2.53	Apollo	18.5	23.7	78	2024-Nov-05 02:33	2.672	252
2024 UB13	https://www.minorplanetcenter.net/mpec/K24/K24V18.html	M22	1.13	Apollo	18.6	22.8	113	2024-Oct-25 17:09	6.546	405
2024 VA4	https://www.minorplanetcenter.net/mpec/K24/K24VH2.html	T05	0.48	Apollo	17.0	25.1	40	2024-Dec-09 14:46	1.815	2768
2024 WK	https://www.minorplanetcenter.net/mpec/K24/K24W38.html	T05	1.46	Apollo	18.4	26.2	24	2024-Nov-24 17:43	4.564	1343
2024 WV51	https://www.minorplanetcenter.net/mpec/K24/K24XL6.html	F52	8.43	Apollo	18.0	25.0	42	2024-Dec-09 14:46	1.815	957
2024 YM12	https://www.minorplanetcenter.net/mpec/K25/K25A13.html	703	0.55	Apollo	19.3	25.8	29	2024-Dec-29 03:28	2.395	695
2024 YM9	https://www.minorplanetcenter.net/mpec/K24/K24YO2.html	703	0.57	Apollo	18.6	22.3	135	2024-Dec-27 23:20	27.608	1376

[a]Observatory code of Discoverer

[b]Time between last observation of discoverer and the first follow-up observation

[c]Absolute magnitude (`https://ssd.jpl.nasa.gov/sbdb.cgi`)

[d]Asteroid size estimated using (`https://cneos.jpl.nasa.gov/tools/ast_size_est.html`) with albedo values of 0.05 and 0.3 to get an average size

[a] 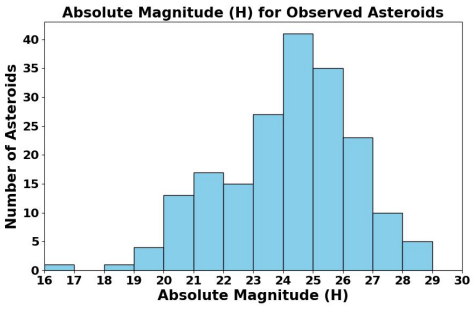

[b] 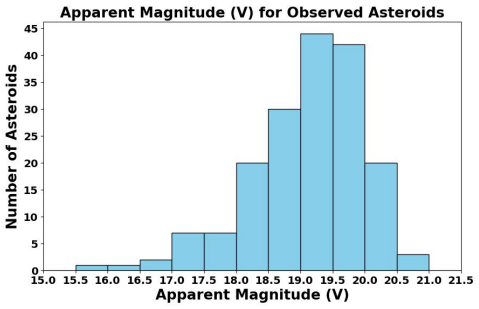

Figure 16: Histogram (a) shows the distribution of Absolute Magnitude (H) values for successfully observed NEAs, with data submitted to the MPC. There is a large distribution of asteroids with high H values, with a median of 24.9, corresponding to diameters of approximately 35–86 m, depending on an assumed albedo of between 0.05 and 0.30. The second histogram shows the Apparent Magnitude (V-magnitude) of the observed asteroids, where a large fraction have a V-magnitude > 19.0. This reflects the Lesedi telescope's ability to perform follow-up observations of objects listed on the NEOCP, which are often faint, while brighter objects (V-magnitude < 18) rarely appear on the page.

3.1.1 Results

One of the main aims of this project was to observe the small NEA population to determine whether their taxonomic distribution mirrors that of previously published results for larger NEAs. As shown in Figure 17, the majority of the asteroids followed up (75%) had diameters of less than 100 m, which demonstrates that the project successfully achieved its goal of probing the small NEA population.

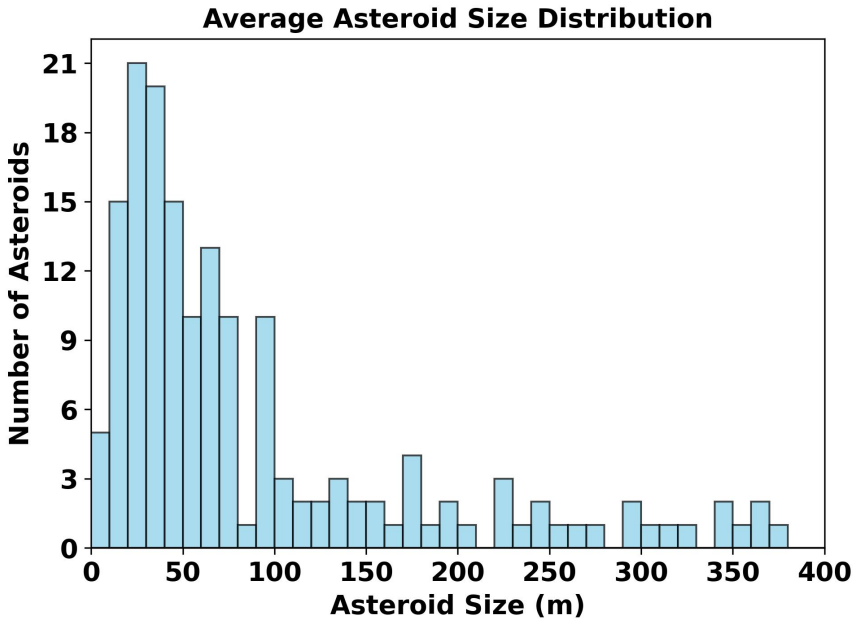

Figure 17: Histogram showing the distribution of estimated average diameters (in metres) for Near-Earth Asteroids (NEAs) observed in this study with assumed albedo values of 0.05 and 0.30 to get an average size. A majority of the observed NEAs are small, with sizes concentrated below 100 metres. This distribution shows the prevalence of smaller NEAs in the sample and supports the project's aim of probing the small NEA population (<300 m).

Figure 18 shows the NEA discovery statistics by survey from 1995 to the present. Pan-STARRS and Catalina have historically been the largest contributors to NEA discoveries, while LINEAR made significant early contributions, with a peak in the mid-2000s. The newer ATLAS survey has rapidly increased its contributions in recent years, particularly benefiting from its Southern Hemisphere expansion through ATLAS-STH and ATLAS-Chile. Although ATLAS's total discovery numbers are smaller compared to other surveys, its frequent sky coverage makes it particularly effective at detecting asteroids that might be missed by deeper surveys. Other programs, such as NEOWISE, have also made important contributions, though at a smaller scale. The data indicates that NEA discovery rates have levelled off in recent years, with 2023 showing a decrease in discoveries and early 2024 suggesting a similar trend. This plateau likely represents a saturation point in discovery rates, primarily due to the comprehensive sky coverage now provided by existing surveys up to certain magnitudes. Future increases in discovery rates will likely depend on the ability to detect fainter objects, a capability that upcoming surveys like the Vera C. Rubin Observatory Legacy Survey of Space and Time (LSST) are expected to provide.

The number of NEAs observed in this project and their discovering surveys are shown in Figure 19. The data shows significant follow-up observations of objects detected by ATLAS, with notable contributions from ATLAS Chile (W68) and SAAO (M22). The prominence of these Southern Hemisphere facilities aligns with the Lesedi telescope's location, making their discoveries particularly accessible for follow-up observations. The data also includes follow-up observations of NEAs discovered by established surveys, including the Catalina Sky Survey (703), PanSTARRS (F51, F52), and Moonbase South Observatory at Hakos, Namibia (L87). ATLAS-STH demonstrates the highest follow-up rate, primarily due to the co-location of the Lesedi Telescope and the ATLAS node at SAAO, enabling efficient same-night rapid follow-up observations.

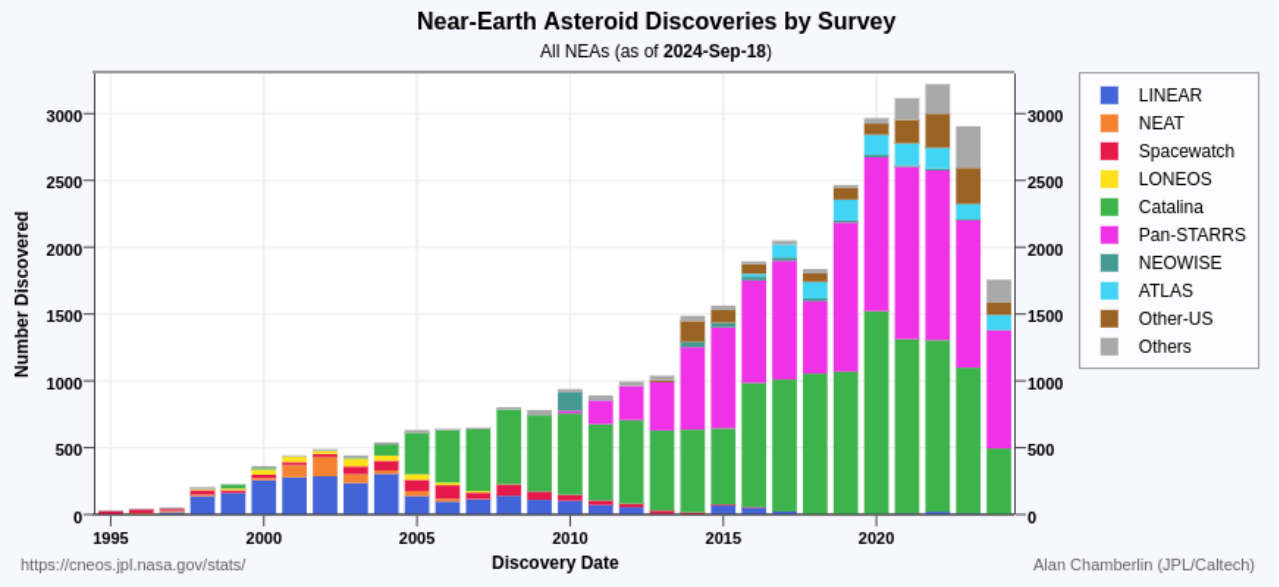

Figure 18: Plot showing cumulative NEA discoveries from 1995 to the present by various ground- and space-based surveys. LINEAR dominated discoveries in the early 2000s but declined after 2005. Catalina Sky Survey and Pan-STARRS have been major contributors in recent years, while ATLAS, though smaller in total discoveries, plays a key role in detecting NEAs that other surveys might miss. Source: `https://cneos.jpl.nasa.gov/stats/site_all.html`

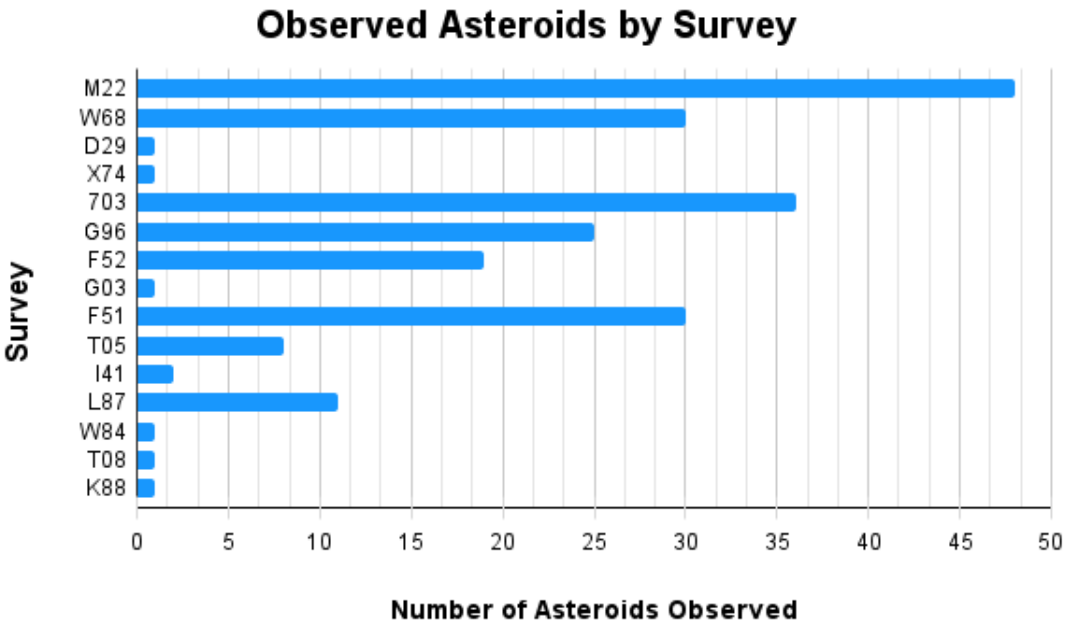

Figure 19: Shows the number of Near-Earth Asteroids (NEAs) successfully followed up on as part of this MSc thesis research.

Table 2: **Surveys and Observatories Locations**

Code	Survey/Observatory and Location
M22	ATLAS–SAAO, Sutherland, South Africa
W68	ATLAS-CHL, El Sauce Observatory, Rio Hurtado, Chile
D29	PMO NEO Survey Program, XuYi Station, Purple Mountain Observatory, Nanjing, China
X74	Campo dos Amarais Observatory, Brazil
703	Catalina Sky Survey, Tucson, Arizona, USA
G96	Mount Lemmon Survey, Mount Lemmon, Arizona, USA
F52	Pan-STARRS 2 (PS2), Haleakalā Observatory, Hawaii, USA
G03	Capricornus Observatory, Csókakő, Hungary
F51	Pan-STARRS 1 (PS1), Haleakalā Observatory, Hawaii, USA
T05	ATLAS-HKO, Haleakalā Observatory, Hawaii, USA
L87	Moonbase South Observatory, Hakos, Namibia
W84	Cerro Tololo-DECam, Cerro Tololo, Chile
I41	Zwicky Transient Facility (ZTF) and Palomar Transient Factory (PTF), Palomar Mountain, California, USA
T08	ATLAS-MLO, Mauna Loa Observatory, Hawaii, USA
K88	GINOP-KHK, Piszkéstető, Hungary

3.1.2 Discussion

One of the primary aims of this study was to conduct rapid follow-up observations of Near-Earth Asteroids (NEAs) and investigate the small NEA population. Figure 15 illustrates the number of successful follow-up observations conducted over different time intervals. The data reveal that approximately 61% of follow-up observations were completed within one day, with 10% achieved in less than three hours. The majority of these observations

occurred within a day of discovery. Although a faster response time is theoretically possible, it is constrained by the time required to report discoveries to the Minor Planet Centre (MPC)[1].

In summary, these results demonstrate the capability of the Lesedi telescope to perform rapid follow-up observations, including same-night observations in some cases. The telescope's ability to observe smaller NEAs is evident, with the smallest asteroid followed up being 2023 SL5, which has an estimated absolute magnitude of 28.7 and a diameter between 4 m and 11 m, depending on its assumed albedo of 0.05 and 0.30. This shows Lesedi's capability and the observing strategy used for this project in targeting and successfully observing very small asteroids.

3.2 Asteroid classification

A useful approach to understanding near-Earth asteroids (NEAs) is to classify them based on multiband photometric data. This method helps infer their taxonomic types, providing insights into their physical and compositional properties. Taxonomic classifications not only help in understanding the origins of NEAs in the Solar System but also provide critical information that can be used in planetary defence strategies, particularly in the event of a potential asteroid impact. Asteroid classification systems, such as the widely used Bus-DeMeo Classification Scheme (DeMeo et al. 2009), categorise asteroids into different types based on their spectral properties (see Section 1.4). In this project, photometric colours were collected using g, r, and i filters, following the procedure described in section 2.5, building a dataset to generate a colour-colour plot ($r-i$ vs. $g-r$). Similarly to what was done by Mommert et al. 2016 and Janse van Rensburg 2021, we performed three sequences of clear, g, r, i, with one-minute exposures for each filter.. Astrometric extraction was performed using the clear frames (see Section 2.4.2) because they provided a higher signal-to-noise ratio (SNR). For this project, the weighted mean magnitudes were computed and colour indices $g-r$ and $r-i$ (see Section 2.5) with the uncertainty for the colour indices. Table 3 shows a summary of $g-r$ and $r-i$ colour indices for the 72 asteroids out of the 230 successful follow-up observations (see Table 1) that yielded sufficient signal-to-noise ratio (SNR) in the filtered frames to extract reliable colour measurements.

Figure 14 shows examples of the resulting multi-filter light-curve plots with error bars, the rest of these plots for all the other NEAs successfully observed in this project can be found in Appendix A. These light curve plots were used to determine the likely taxonomic types of the observed NEAs. This was done by superimposing the calculated $g-r$ and $r-i$ magnitudes on a decision boundary surface (Figure 22) generated through a machine learning algorithm, as done by Janse van Rensburg 2021. The method used in this work

[1] `http://www.minorplanetcenter.net/iau/mpc.html`

involved several steps to classify asteroid taxonomic types using machine learning. First, data for various taxonomic types (e.g., S, C, X, V, D, and Q) was collected from synthetic colour data generated from observed spectra. The synthetic colours together with the corresponding observed spectrum that could be matched to a specific taxonomic type could therefore be used as a training dataset for the ML algorithms. Next, the data was preprocessed which included scaling the features and splitting the dataset into training and test sets. Both scaled and unscaled versions of the data were used. Several machine learning models were tested, including, Random Forest, and Support Vector Machines (SVM). Hyperparameter tuning was performed using grid search with cross-validation to find the best model settings. The models were then trained on the training data and evaluated on the test data. This would then be used to generate the decision surfaces. A normalized confusion matrix was also used to assess the accuracy of the models for each taxonomic type.

This decision boundary surface separates asteroids into their respective taxonomic types depending on where they fall relative to the decision boundaries. Some data points had error bars extending into multiple taxonomic boundaries, making classification uncertain. To improve the accuracy of the classifications, a probabilistic approach was adopted, which accounts for the uncertainties in the measured colour indices. Rather than relying solely on the location of the asteroid on the decision boundary surface, this method calculated the likelihood of each target belonging to specific taxonomic classes. This is a similar method chosen by Mommert et al. 2016, Erasmus et al. 2017 and Janse van Rensburg 2021. Instead of relying on a single measured colour value, the method generates 10,000 random pseudo-colours for each asteroid, following a Gaussian distribution within 1σ of the measured error. This approach is based on the $g - r$ and $r - i$ photometric indices (Figures 20 and 21).

Once the pseudo-colours are generated, this method then involves calculating the likelihood of the asteroid belonging to each taxonomic class—S, C, X, D, Q, and V—by assessing how many of the pseudo-colours fall into each classification zone within the surface. These pseudo-colours are classified and a percentage probability is returned. Table 3 presents the results from this analysis. An asteroid is assigned a taxonomic type if more than 50% of the generated pseudo-colours correspond to a specific class. For cases where no single class meets this threshold, no class is assigned but the table still shows the relative likelihoods of all potential classifications. An example of such a case where an asteroid was left unclassified is shown in Figure 21 for asteroids 2023 EU4 and 2024 PA. Table 4 summarizes the percentage probabilities the percentage probabilities of these 72 NEAs.

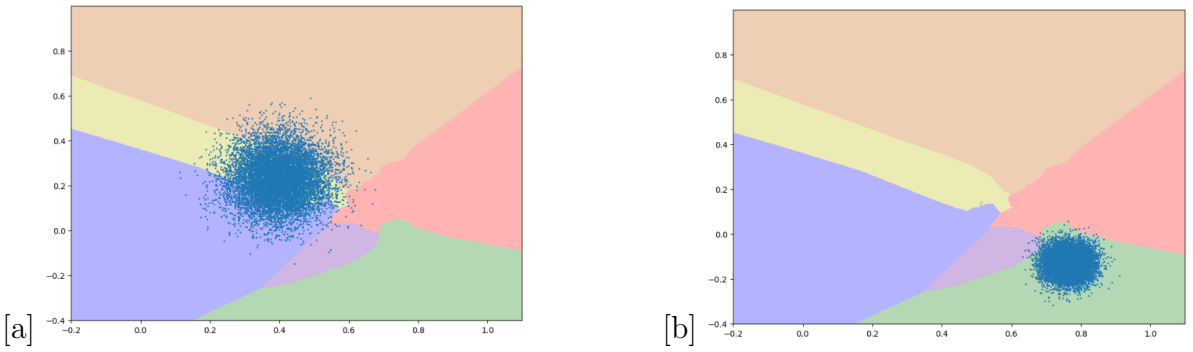

Figure 20: Distribution of 10,000 random pseudo-colours for asteroids on the decision surface for two asteroids: a) 2024 EJ1 and b) 2023 QB.a) 2024 EJ1, where 66.4% of the pseudo-colours fall within the X type, indicating its likely taxonomic classification as X; b) 2023 QB, which shows 99.6% of the pseudo-colours corresponding to the V type, suggesting its probable classification as V.

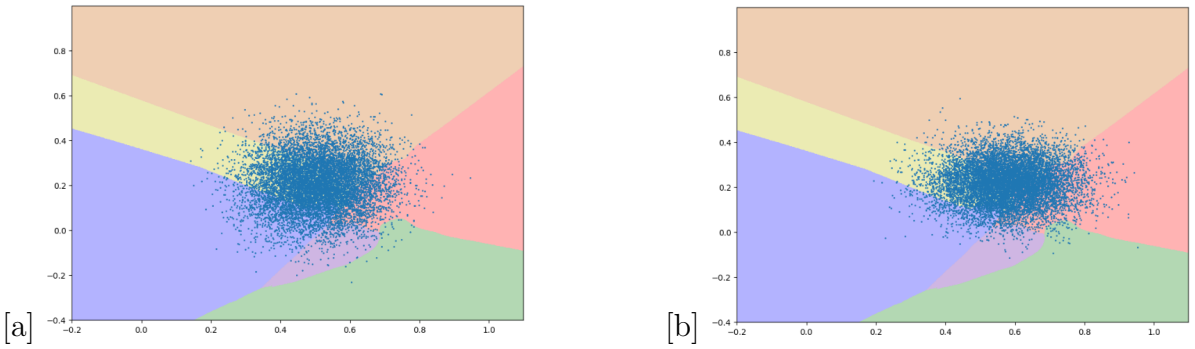

Figure 21: Distribution of 10,000 random pseudo-colours for asteroids with the calculated $g-r$ and $r-i$ values superimposed on the decision boundary surface. These two asteroids did not meet the set threshold of 50%: a) 2024 PA, which exhibited its highest percentage probabilities of 43.2% of the pseudo-colours falling within the X region and 27.9% in the D region; and b) 2023 EU4, which had its highest percentage probabilities of 35.5% in the D region and 31.7% of the pseudo-colours falling in the X region. So these two asteroids were left unclassified.

Table 3: **Summary of colour indices**

Asteroid name	MPEC Link	Absolute Magnitude (H)	Size[a] (m)	r'-i'	r'-i' sig	g'-r'	g'-r' sig
2023 PR	https://www.minorplanetcenter.net/mpec/K23/K23P55.html	24.6	50	0.208	0.048	0.824	0.055
2023 QB	https://www.minorplanetcenter.net/mpec/K23/K23Q11.html	20.8	290	-0.128	0.048	0.764	0.037
2023 QW	https://www.minorplanetcenter.net/mpec/K23/K23Q39.html	26.0	26	0.175	0.169	0.442	0.165
2007 RR17	https://www.minorplanetcenter.net/mpec/K23/K23QA7.html	23.8	71	0.244	0.041	0.754	0.040
2023 QN7	https://www.minorplanetcenter.net/mpec/K23/K23QG1.html	23.6	78	0.296	0.081	0.566	0.071
2023 RF1	https://www.minorplanetcenter.net/mpec/K23/K23R55.html	25.8	29	0.145	0.027	0.760	0.038
2023 RW9	https://www.minorplanetcenter.net/mpec/K23/K23RL8.html	22.1	162	0.658	0.097	0.597	0.087
2023 SZ3	https://www.minorplanetcenter.net/mpec/K23/K23SF2.html	24.1	65	0.137	0.087	0.638	0.084
2023 SK4	https://www.minorplanetcenter.net/mpec/K23/K23SG3.html	24.8	44	0.318	0.110	0.464	0.116
2023 SL8	https://www.minorplanetcenter.net/mpec/K23/K23TO2.html	24.4	55	0.241	0.041	0.664	0.039
2013 TG6	https://www.minorplanetcenter.net/mpec/K23/K23T14.html	26.6	20	0.139	0.086	0.470	0.075
2023 TP15	https://www.minorplanetcenter.net/mpec/K23/K23U07.html	26.0	27	-0.020	0.134	0.481	0.086
2023 UT	https://www.minorplanetcenter.net/mpec/K23/K23U76.html	21.8	185	0.482	0.088	0.627	0.080
2023 UD3	https://www.minorplanetcenter.net/mpec/K23/K23UF0.html	19.5	535	0.215	0.132	1.093	0.272
2023 UN7	https://www.minorplanetcenter.net/mpec/K23/K23UM9.html	24.1	62	0.109	0.124	0.580	0.151
2023 VR4	https://www.minorplanetcenter.net/mpec/K23/K23VE8.html	23.0	105	0.217	0.062	0.554	0.047
2023 VV4	https://www.minorplanetcenter.net/mpec/K23/K23VF2.html	22.3	147	0.052	0.204	0.415	0.114
2023 VK7	https://www.minorplanetcenter.net/mpec/K23/K23VL4.html	22.7	119	0.505	0.132	0.149	0.158
2023 VN7	https://www.minorplanetcenter.net/mpec/K23/K23VL6.html	25.4	33	0.279	0.120	0.358	0.074
2023 VP7	https://www.minorplanetcenter.net/mpec/K23/K23VL8.html	23.4	90	0.101	0.116	0.636	0.101
2024 CO1	https://www.minorplanetcenter.net/mpec/K24/K24C89.html	20.3	365	0.086	0.158	0.456	0.090
2018 CY2	https://www.minorplanetcenter.net/mpec/K24/K24C94.html	22.5	134	0.226	0.054	0.813	0.049
2024 CO2	https://www.minorplanetcenter.net/mpec/K24/K24CC4.html	26.8	17	0.743	0.105	0.853	0.141
2024 CR2	https://www.minorplanetcenter.net/mpec/K24/K24CC6.html	23.9	70	0.414	0.101	0.304	0.076
2024 CG2	https://www.minorplanetcenter.net/mpec/K24/K24CB8.html	23.1	99	0.556	0.017	0.149	0.016
2024 CK3	https://www.minorplanetcenter.net/mpec/K24/K24CE7.html	24.7	47	0.069	0.092	0.527	0.073
2024 CG2	https://www.minorplanetcenter.net/mpec/K24/K24CB8.html	23.1	37	-0.397	0.017	1.375	0.016
2024 CG4	https://www.minorplanetcenter.net/mpec/K24/K24CF8.html	23.7	77	0.038	0.121	0.590	0.082
2024 EC	https://www.minorplanetcenter.net/mpec/K24/K24E14.html	24.0	65	0.164	0.122	0.440	0.163
2024 ER	https://www.minorplanetcenter.net/mpec/K24/K24E32.html	21.4	220	-0.068	0.038	0.700	0.055
2024 EJ1	https://www.minorplanetcenter.net/mpec/K24/K24E61.html	20.4	345	0.236	0.098	0.397	0.074
2024 EQ1	https://www.minorplanetcenter.net/mpec/K24/K24E68.html	25.1	40	0.285	0.068	0.651	0.068
2024 EN2	https://www.minorplanetcenter.net/mpec/K24/K24EB7.html	26.5	20	-0.033	0.192	0.711	0.106
2024 EP3	https://www.minorplanetcenter.net/mpec/K24/K24EG7.html	24.7	48	0.167	0.190	0.541	0.127
2024 EH3	https://www.minorplanetcenter.net/mpec/K24/K24EF8.html	25.5	34	0.168	0.130	0.483	0.080
2024 EU4	https://www.minorplanetcenter.net/mpec/K24/K24F03.html	22.1	156	0.218	0.088	0.578	0.104
2024 GL	https://www.minorplanetcenter.net/mpec/K24/K24F08.html	24.9	44	0.159	0.048	0.573	0.040
2024 HJ	https://www.minorplanetcenter.net/mpec/K24/K24G52.html	21.0	265	0.152	0.055	0.481	0.050
2024 HR1	https://www.minorplanetcenter.net/mpec/K24/K24H29.html	23.1	99	0.185	0.070	0.300	0.066
2024 JA2	https://www.minorplanetcenter.net/mpec/K24/K24H92.html	24.2	62	0.140	0.028	0.655	0.034
2024 JZ6	https://www.minorplanetcenter.net/mpec/K24/K24J88.html	20.7	305	0.159	0.051	0.578	0.060
2024 JW16	https://www.minorplanetcenter.net/mpec/K24/K24JM7.html	20.9	275	0.377	0.158	0.244	0.071
2024 LN2	https://www.minorplanetcenter.net/mpec/K24/K24JT8.html	20.3	375	0.206	0.226	0.181	0.208
2024 LH3	https://www.minorplanetcenter.net/mpec/K24/K24L99.html	24.4	56	-0.081	0.132	0.736	0.105
2024 NC	https://www.minorplanetcenter.net/mpec/K24/K24LB9.html	25.0	43	-0.059	0.183	0.748	0.126
2002 MR3	https://www.minorplanetcenter.net/mpec/K24/K24N24.html	21.4	220	0.132	0.117	0.487	0.072
2024 OM1	https://www.minorplanetcenter.net/mpec/K24/K24N77.html	24.3	57	0.168	0.086	0.780	0.092
2024 OO1	https://www.minorplanetcenter.net/mpec/K24/K24OB1.html	24.8	46	0.133	0.179	0.581	0.099
2024 PA	https://www.minorplanetcenter.net/mpec/K24/K24OB3.html	25.0	43	0.210	0.112	0.507	0.101
2024 PC	https://www.minorplanetcenter.net/mpec/K24/K24P31.html	26.4	21	0.036	0.073	0.472	0.056
2024 PW	https://www.minorplanetcenter.net/mpec/K24/K24P34.html	21.9	169	0.012	0.332	0.134	0.142
2024 PC2	https://www.minorplanetcenter.net/mpec/K24/K24P67.html	22.3	142	0.084	0.024	0.687	0.023
2024 PF6	https://www.minorplanetcenter.net/mpec/K24/K24P96.html	25.2	38	0.298	0.129	0.541	0.153
2024 QK	https://www.minorplanetcenter.net/mpec/K24/K24Q03.html	24.2	38	0.441	0.222	0.514	0.206
2024 QS1	https://www.minorplanetcenter.net/mpec/K24/K24Q41.html	22.1	161	0.526	0.092	0.479	0.088
2024 QV1	https://www.minorplanetcenter.net/mpec/K24/K24Q85.html	24.8	46	0.137	0.043	0.451	0.034
2024 QK2	https://www.minorplanetcenter.net/mpec/K24/K24Q89.html	25.6	31	-0.074	0.053	0.786	0.047
2024 RH6	https://www.minorplanetcenter.net/mpec/K24/K24RH7.html	28.6	8	0.326	0.240	0.204	0.125
2024 RT12	https://www.minorplanetcenter.net/mpec/K24/K24RQ7.html	26.0	27	-0.034	0.184	0.358	0.151
2024 RW4	https://www.minorplanetcenter.net/mpec/K24/K24R15.html	25.0	43	0.221	0.076	0.381	0.052
2024 SA7	https://www.minorplanetcenter.net/mpec/K24/K24T16.html	27.3	15	0.549	0.143	0.632	0.206
2024 SQ	https://www.minorplanetcenter.net/mpec/K24/K24S51.html	25.8	28	-0.087	0.122	0.122	0.110
2024 TA	https://www.minorplanetcenter.net/mpec/K24/K24T24.html	28.2	9	-0.005	0.248	0.439	0.160
2024 TB22	https://www.minorplanetcenter.net/mpec/K24/K24U13.html	19.2	605	0.081	0.046	0.594	0.124
2024 TK7	https://www.minorplanetcenter.net/mpec/K24/K24TL7.html	24.1	86	0.071	0.160	0.475	0.143
2024 TL5	https://www.minorplanetcenter.net/mpec/K24/K24TI5.html	27.7	12	-0.476	0.563	0.527	0.321
2024 TU3	https://www.minorplanetcenter.net/mpec/K24/K24TG0.html	28.1	10	0.201	0.144	0.933	0.230
2024 UB13	https://www.minorplanetcenter.net/mpec/K24/K24V18.html	22.8	113	0.315	0.064	0.524	0.061
2024 UJ8	https://www.minorplanetcenter.net/mpec/K24/K24UN2.html	19.9	435	-0.119	0.177	0.533	0.111
2024 UT7	https://www.minorplanetcenter.net/mpec/K24/K24UM1.html	23.7	78	0.373	0.067	0.639	0.064

[a]Size estimated using absolute magnitude and assumed albedo of between 0.05 and 0.30 (`https://cneos.jpl.nasa.gov/tools/ast_size_est.html`)

3.2.1 Results

Using the decision surfaces, the likely taxonomic types for 72 out of 230 successfully observed NEAs were determined. These 72 NEAs were the only ones that had enough SNR to produce colours. From these, 24.6% were classified as D-types, 21.8% S-types, 21.3% as X-types, 17.9% as C-types, 9.6% as V-types and 4.8% as Q-types. For these the median absolute magnitude H is 24.9 corresponding to a size of between 35 m and 62 m depending on an assumed albedo of 0.05 and 0.30. A summary of this is shown in Figure 23 which was generated by calculating the percentage of all the pseudo colours that fall into each taxonomic class using the decision boundary in Figure 22.

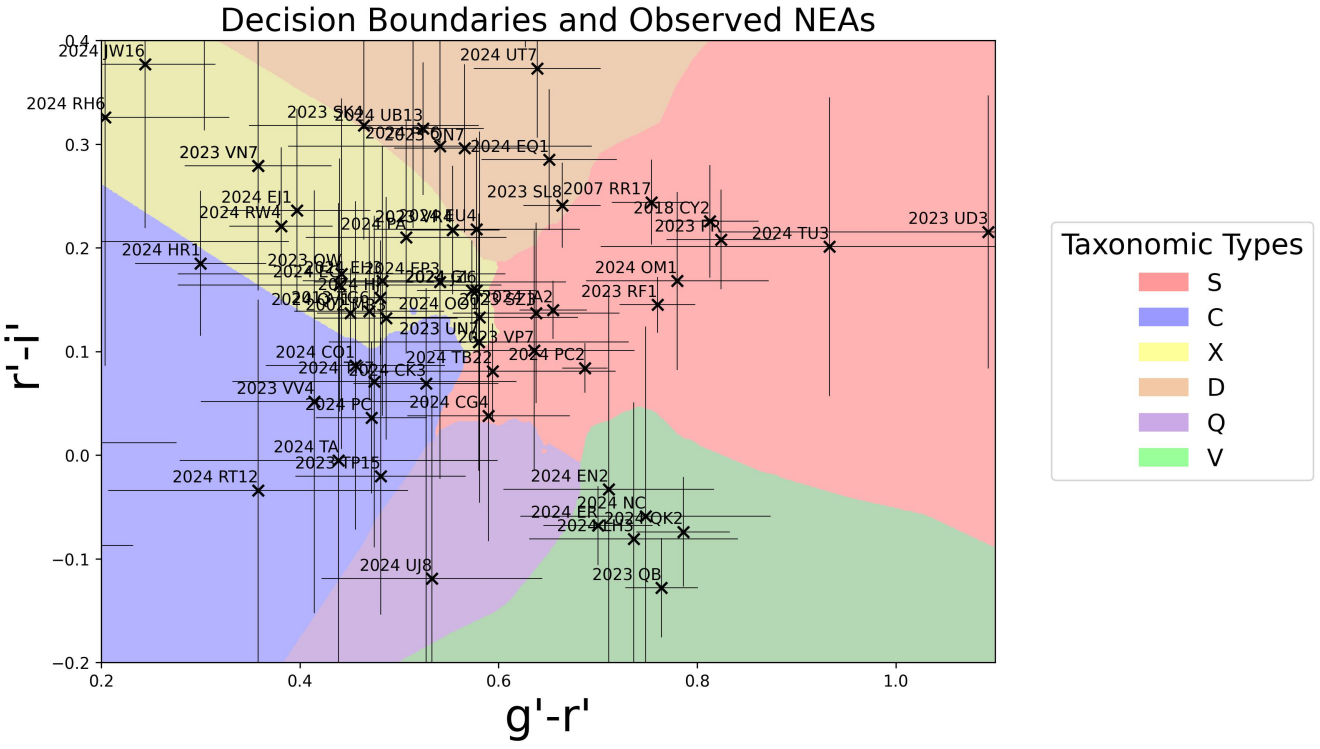

Figure 22: Plot shows asteroids (marked with x) for which $g - r$ and $r - i$ colours were calculated. These colours are superimposed on a decision boundary surface generated by a machine learning algorithm (Janse van Rensburg 2021).

The distribution of taxonomic classes was analysed using the full probability values rather than the most probable classification assigned using the 50% threshold. For each object, the classification method provided probability estimates across six taxonomic classes (S, C, X, D, Q, and V). By averaging these probabilities across all objects, a distribution

was obtained that captures the uncertainty in asteroid classification. This probabilistic approach preserves information about classification uncertainty and asteroids that have a high number of pseudo colours in multiple taxonomic classes. The plot shows a significant number of D-type asteroids than reported in previous literature. It also shows a significant number of S-type asteroids but this is much less than in previous studies of the distribution of NEAs.

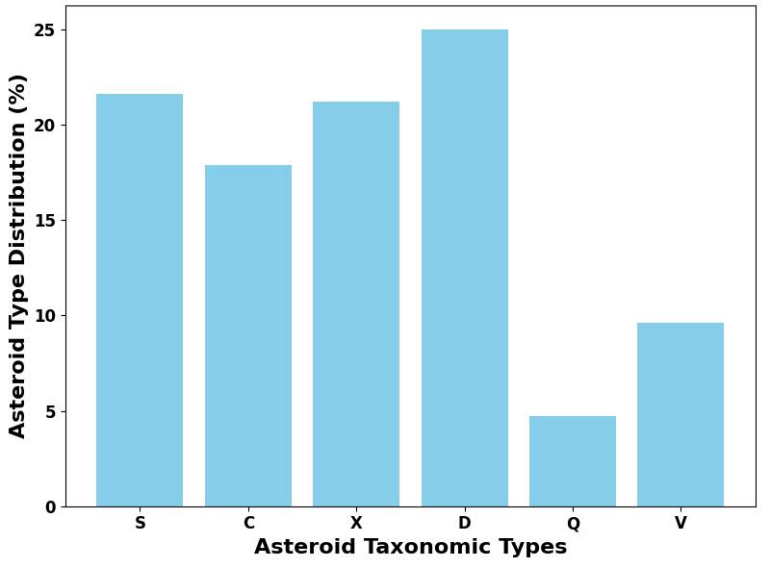

Figure 23: Distribution of asteroid taxonomic types derived from this study's dataset using the first decision boundary.

Table 4: **Asteroid Classification Probabilities for first decision boundary**

Asteroid Name	S probability	C probability	X probability	D probability	Q probability	V probability	Most probable class
2023 PR	99.4	0.0	0.0	0.6	0.0	0.0	S
2023 QB	0.1	0.0	0.0	0.0	0.1	99.7	V
2023 QW	9.6	32.9	29.6	19.4	5.7	2.7	-
2007 RR17	93.7	0.0	0.0	6.4	0.0	0.0	S
2023 QN7	6.7	0.9	22.0	70.3	0.1	0.0	D
2023 RF1	100	0.0	0.0	0.0	0.0	0.0	S
2023 SZ3	56.9	6.9	14.0	13.0	5.6	3.6	S
2023 SL8	47.0	0.0	0.7	52.4	0.0	0.0	D
2013 TG6	5.1	38.1	48.4	5.5	2.9	0.1	-
2023 UN7	32.0	22.2	18.9	10.0	9.7	7.2	-
2023 VR4	8.2	3.9	48.2	39.6	0.1	0.0	-
2023 VN7	0.0	18.9	59.9	21.1	0.1	0.0	X
2023 SK4	3.3	5.2	40.2	51.2	0.1	0.0	D
2023 TP15	5.0	44.9	11.5	1.5	27.5	9.6	-
2023 UT	1.0	0.0	0.3	98.7	0.0	0.0	D
2023 UD3	91.8	0.7	1.2	4.6	0.3	1.4	S
2023 RW9	0.0	0.0	0.0	100	0.0	0.0	D
2023 VV4	2.8	47.1	22.1	8.9	10.9	8.3	-
2023 VK7	0.0	9.0	41.0	50.0	0.0	0.0	-
2023 VP7	45.4	9.8	11.1	11.3	12.8	9.7	-
2024 CO1	4.2	42.4	28.2	9.0	12.7	3.6	-
2018 CY2	98.6	0.0	0.0	1.4	0.0	0.0	S
2024 CO2	6.2	0.0	0.0	93.8	0.0	0.0	D
2024 CR2	0.0	2.6	46.7	50.7	0.0	0.0	D
2024 CG2	0.0	0.0	0.2	99.8	0.0	0.0	D
2024 CK3	16.2	37.6	22.3	3.2	19.7	1.1	-
2024 CG4	27.5	15.4	10.9	6.0	29.1	11.2	-
2023 UN7	31.8	21.9	18.7	10.2	10.1	7.3	-
2023 VR4	7.7	4.2	49.3	38.8	0.1	0.0	-
2023 VN7	0.0	19.3	59.8	20.8	0.1	0.0	X
2024 EC	11.7	37.4	34.0	12.3	3.6	1.0	-
2024 ER	1.8	0.0	0.0	0.0	28.0	70.3	V
2024 EJ1	0.2	19.9	65.9	13.9	0.1	0.0	X
2024 EQ1	27.6	0.1	4.2	68.0	0.0	0.0	D
2024 EN2	30.9	1.9	1.7	5.6	11.1	48.8	-
2024 EP3	17.3	18.3	20.6	27.8	9.7	6.3	-
2024 EH3	5.8	27.8	42.6	18.0	5.5	0.3	-
2024 EU4	26.3	6.5	32.1	34.0	0.8	0.4	-
2024 GL	26.5	9.3	49.7	14.2	0.3	0.0	-
2024 HJ	1.7	27.1	69.1	1.9	0.2	0.0	X
2024 HR1	0.0	57.9	42.0	0.1	0.0	0.0	C
2024 JA2	95.5	0.1	3.4	0.9	0.0	0.0	S
2024 JZ6	33.7	9.8	42.9	13.4	0.2	0.0	-
2024 JW16	0.0	19.1	46.9	34.0	0.0	0.0	-
2024 LN2	0.9	57.2	25.3	14.3	1.2	1.3	C
2024 LH3	22.3	1.0	0.6	0.5	12.3	63.4	V
2024 NC	30.0	1.9	1.4	3.0	8.9	54.9	V
2002 MR3	6.0	34.5	40.4	10.6	8.1	0.4	-
2024 OM1	89.3	0.2	0.9	6.0	0.4	3.3	S
2024 OO1	22.7	12.6	17.1	24.4	14.8	8.4	-
2024 PA	10.7	16.7	42.8	27.1	2.3	0.4	-
2024 PC	3.3	70.3	12.0	0.2	14.2	0.0	C
2024 PW	0.0	68.3	12.6	7.6	0.6	11.0	C
2024 PC2	98.7	0.0	0.0	0.0	0.0	1.3	S
2024 PF6	15.1	6.6	27.3	50.0	0.7	0.4	-
2024 QK	9.8	6.5	14.7	67.3	1.0	0.8	D
2024 QS1	0.0	0.0	2.0	98.0	0.0	0.0	D
2024 QV1	0.0	33.9	66.1	0.0	0.0	0.0	X
2024 QK2	4.7	0.0	0.0	0.0	0.6	94.7	V
2024 RW4	0.0	19.6	76.7	3.7	0.0	0.0	X
2024 RH6	0.1	38.7	32.9	27.9	0.2	0.2	-
2024 RT12	2.3	61.8	10.4	2.2	10.3	13.0	C
2024 SQ	0.0	98.6	0.2	0.0	0.2	1.0	C
2024 SA7	9.8	0.1	3.6	86.6	0.0	0.0	D
2024 TA	5.8	37.2	14.7	9.6	11.8	20.9	-
2024 TU3	80.8	1.6	2.8	9.4	1.0	4.5	S
2024 TL5	5.9	12.8	3.2	6.7	2.8	68.7	V
2024 TK7	10.5	39.6	21.1	8.1	13.3	7.4	-
2024 TB22	50.6	30.2	10.7	0.2	5.1	3.2	S
2024 UJ8	6.8	20.4	5.1	1.9	26.4	39.5	-
2024 UT7	4.2	0.0	0.8	95.0	0.0	0.0	D
2024 UB13	0.6	0.1	28.3	71.0	0.0	0.0	D
Total	21.8	17.9	21.3	24.6	4.8	9.6	100

3.2.2 Discussion

The classification of Near-Earth Asteroids (NEAs) is essential for understanding their composition, origin, and potential hazard. This study applied a probabilistic approach to taxonomic classification using colour indices, enabling a detailed analysis of asteroid types within the dataset. Figure 22 illustrates the classification of asteroids based on their colour indices, generated as part of a data analysis and visualization process designed to support NEA taxonomy. This process involved importing libraries essential for data manipulation, machine learning, and visualization (e.g., NumPy, Matplotlib, and scikit-learn). The data analyzed includes colour index measurements for both synthetic and randomly generated asteroids, categorized by taxonomic type (e.g., S, C, X, D, Q, V).

In this approach, synthetic and random data points were combined, labelled according to asteroid type, and then partitioned into training and testing sets for model development and evaluation. Various machine learning classifiers, including K-Nearest Neighbors (KNN), were employed, with grid search used to optimize hyperparameters to improve classification accuracy.

The final phase of the analysis involved visualizing the data alongside the decision boundaries established by the trained classifier. Scatter plots depict the colour indices of asteroids, with error bars indicating measurement uncertainties, and data points are labelled according to asteroid designations. The decision boundary delineates regions corresponding to distinct asteroid types within the Bus-DeMeo Classification scheme (DeMeo et al. 2022), thereby offering insights into the distribution of different asteroid types in colour space and identifying potential classifications for the observed asteroids.

As seen from Figure 23, it was found that the results did not fully match previous literature. More D-type asteroids were found compared to Hromakina et al. 2021 where they found 12% D-types and Erasmus et al. 2017 also found significantly less D-type asteroids.

This discrepancy prompted a re-evaluation of the initial model's decision boundary. The initial model was trained using data that may not have been representative of the true spectral type distributions, particularly for D-type asteroids. Training data from (Popescu et al. 2018) was used to generate a similar decision boundary as shown in Figure 24 and the colour indices obtained were also superimposed on that decision surface. This approach yielded the following distribution: X-type 28.1%, S-type 27.6%, C-type 25.7%, Q-type 9.9%, V-type 8.7% and D-type (1%). These boundaries help infer likely taxonomic types for each plotted asteroid. The plot shows asteroids (marked with an 'x') for which $g - r$ and $r - i$ colours have been calculated within this program and shown in Table 3.

Compared to earlier results from this analysis, it was found that there is a higher percentage of X-types 28.1%, while D-types were no longer prominently represented (down to 1% in the second decision boundary. The graph shown in Figure 25 summarises the

taxonomic classes obtained from the second dataset. This revision aligns more closely with the current understanding of asteroid compositions and reflects potential observational biases in the original dataset to D-type asteroids. Erasmus et al. 2017 conducted a photometric survey of NEAs and found that S-types and non-stony types (C+X+D) were present in a 1:1 ratio. In contrast, this study identified 27.6% S-types, which is significantly lower. This discrepancy could be attributed to the high H magnitudes of the asteroids in the sample (H > 22), which likely biases the dataset toward fainter, less reflective objects. Furthermore, Erasmus's sample primarily observed NEAs with H = 15 - 25, whereas a large portion of the dataset was composed of fainter NEAs, potentially skewing the taxonomic distribution. This could also mean that there could be a different distribution of asteroid types in the small NEA population. Mommert et al. 2016 classified 86 NEAs and observed a lower-than-expected fraction of S-complex asteroids, consistent with the findings of this project. The 27.6% S-types identified in this study are in line with Mommert's suggestion that S-types may be less common in the small NEA population than previously assumed.

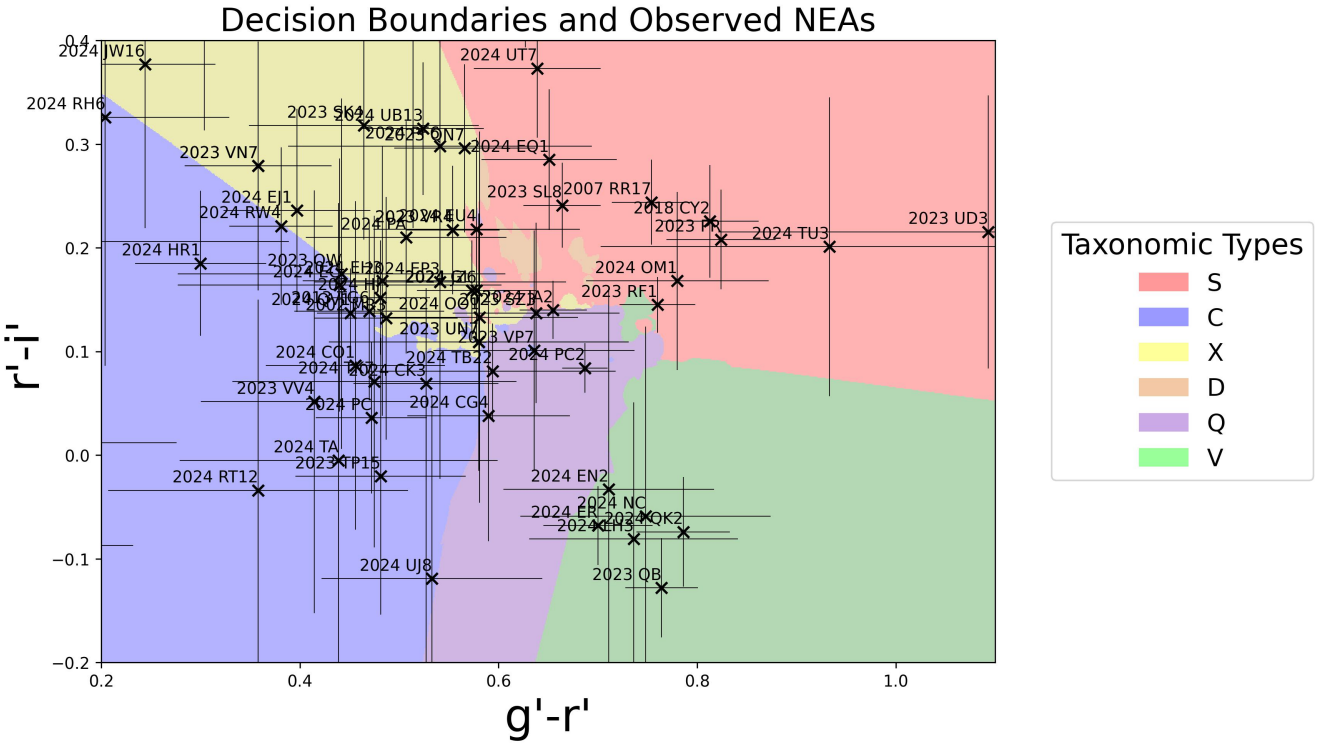

Figure 24: Plot showing asteroids (marked with 'x') with calculated g'-r' and r'-i' colours, alongside decision boundaries from a trained machine learning algorithm, using data from Popescu et al. 2021.

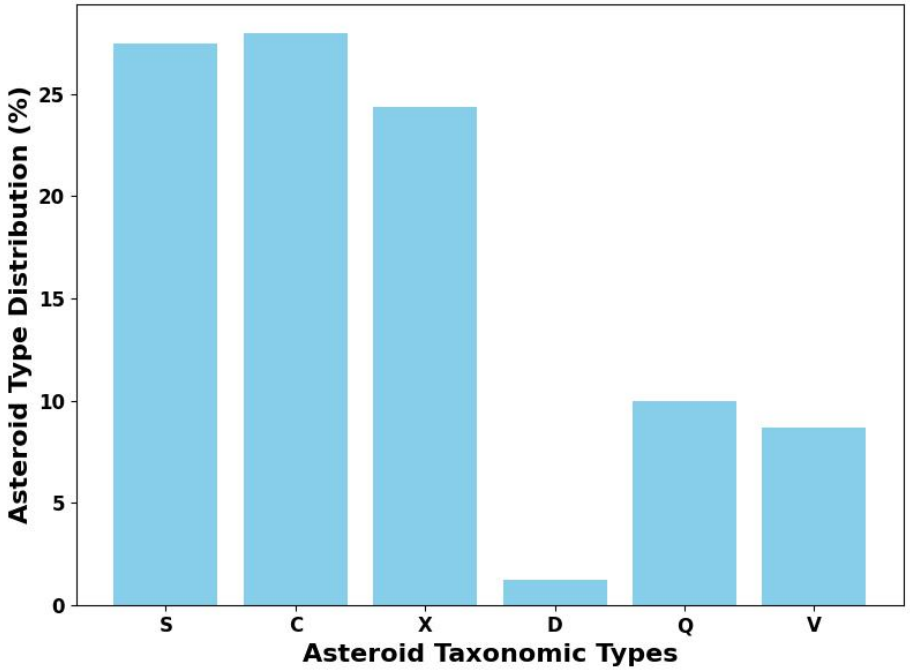

Figure 25: Distribution of asteroid taxonomic types derived from comparison data. This histogram shows the proportions of asteroid taxonomic types in the reference dataset, with type S asteroids representing the highest fraction.

In the first decision boundary, 24% of the classified NEAs were identified as D-types, which was notably higher than reported in the literature. For instance, Hromakina et al. 2021 found only 12% D-types in a photometric survey of 55 NEAs, while Erasmus et al. 2017 and Mommert et al. 2016 also reported lower D-type fractions. The rarity of D-types in NEA populations has been documented, possibly due to their fragile, volatile-rich nature, which makes them less likely to survive the transition to become NEAs. Results from the second decision boundary (Figure 24) showed a reduced fraction of D-type asteroids and a slight increase in the X-type fraction, bringing the results to closer agreement with other studies. The updated 28.1% X-types in this study are consistent with the suggestion by Delbo et al. 2019 that many X-type asteroids in the inner main belt have been under-represented due to the dispersion of ancient collisional families. This supports the growing evidence that X-types may be more common among NEAs than previously thought.

The work by Hromakina et al. 2021 emphasized the observational bias toward brighter, smaller asteroids, particularly in datasets that focus on objects with D < 500 m. In their sample, silicate (S+Q complex) asteroids were over-represented, accounting for 43% of the classified objects. By considering S, V and Q-type asteroids to be stony types, it shows an approximately 1:1 for (S+V+Q):(C+X). This result agrees with Erasmus et al.

2017 who found a similar ratio for S:(C+D) types. Binzel and Rivkin 2001 also found a large number of S and C types. In contrast, the asteroids observed include a significant number of objects with H-magnitude $H > 22$, which may have contributed to the lower proportion of S-types and the higher representation of X-types. Additionally, Hromakina et al. 2021 noted that carbonaceous asteroids (C-types) are more prevalent among objects with Tisserand parameter $Tj < 3$, indicating their likely origin from extinct or dormant comets. The Tisserand parameter is a nearly conserved quantity that describes the relationship between a small body (such as an asteroid or a comet) and a much larger perturbing body (usually Jupiter); objects with $Tj < 3$ typically have orbit characteristics similar to Jupiter-family comets, while asteroids have $Tj > 3$. While this study did not directly investigate Tisserand parameters, the high classification of C-types in both decision boundaries(17.9% and 25.7%) is consistent with their findings and further supports the hypothesis that some NEAs may have cometary origins.

Table 5: **Asteroid Classification Probabilities using second decision boundary**

Asteroid Name	S probability	C probability	X probability	D probability	Q probability	V probability	Most probable class
2023 PR	97.8	0	0	0.2	0.6	1.3	S
2023 QB	0	0	0	0	0.4	99.7	V
2023 QW	12.9	43.8	33.8	0.7	6.9	2.0	-
2007 RR17	98.8	0	0	0.7	0.2	0.3	S
2023 QN7	45.9	1.4	49.0	2.6	1.2	0.0	-
2023 RF1	72.3	0.0	0.5	0.6	13.2	13.6	S
2023 SZ3	32.2	10.9	16.7	3.8	30.4	6.0	-
2023 SL8	90.2	0.0	1.5	7.3	0.9	0.1	S
2013 TG6	3.1	51.8	41.3	0.4	3.4	0.0	C
2023 UN7	20.2	30.9	18.9	1.6	19.4	8.9	-
2023 VR4	23.1	3.8	66.0	4.2	2.9	0.0	X
2023 VN7	0.4	32.9	66.6	0.0	0.0	0.0	X
2023 SK4	18.8	10.9	68.7	0.8	0.8	0.0	X
2023 TP15	1.0	71.4	9.3	0.2	16.9	1.1	C
2023 UT	92.1	0.0	7.8	0.0	0.0	0.0	S
2023 UD3	84.9	0.9	2.0	0.2	1.7	10.3	S
2023 RW9	95.3	0.0	4.7	0.0	0.0	0.0	S
2023 VV4	3.0	66.3	22.6	0.2	7.0	0.8	C
2023 VK7	1.9	14.7	83.3	0.0	0.0	0.0	X
2023 VP7	24.8	15.1	14.0	2.2	31.8	12.0	-
2024 CO1	3.4	60.1	28.6	0.5	7.1	0.3	C
2018 CY2	98.2	0.0	0.0	0.2	0.5	1.1	S
2024 CO2	99.9	0.0	0.1	0.0	0.0	0.0	S
2024 CR2	0.4	7.3	92.3	0.0	0.0	0.0	X
2024 CG2	0.0	0.0	100.0	0.0	0.0	0.0	X
2024 CK3	4.2	53.6	21.1	0.7	20.0	0.5	C
2024 CG4	9.2	28.2	12.0	1.2	41.1	8.4	-
2023 UN7	20.9	31.2	18.2	1.5	18.5	9.7	-
2023 VR4	22.5	4.0	66.5	4.2	2.9	0.0	X
2023 VN7	0.5	32.4	67.1	0.0	0.0	0.0	X
2024 EC	10.8	48.2	31.8	0.9	6.7	1.5	-
2024 ER	0.0	0.3	0.0	0.0	33.0	66.7	V
2024 EJ1	0.9	36.4	62.5	0.1	0.1	0.0	X
2024 EQ1	82.1	0.1	13.2	3.2	1.3	0.1	S
2024 EN2	18.6	4.9	2.5	0.8	26.8	46.5	-
2024 EP3	23.8	27.9	29.4	1.3	13.3	4.3	-
2024 EH3	6.8	39.5	47.7	0.9	5.1	0.1	-
2024 EU4	37.7	9.5	41.0	3.4	7.7	0.7	-
2024 GL	20.9	10.5	52.6	4.8	11.2	0.0	X
2024 HJ	1.3	42.4	55.3	0.2	0.9	0.0	X
2024 HR1	0.0	81.3	18.7	0.0	0.0	0.0	C
2024 JA2	36.8	1.1	9.4	4.9	47.0	0.8	-
2024 JZ6	23.9	11.4	44.3	5.3	14.9	0.2	-
2024 JW16	0.1	28.5	71.4	0.0	0.0	0.0	X
2024 LN2	2.3	65.7	30.8	0.1	0.9	0.2	C
2024 LH3	6.7	3.8	0.8	0.1	23.7	64.8	V
2024 NC	15.2	5.1	2.0	0.4	19.4	58.0	V
2002 MR3	4.3	48.8	40.8	0.6	5.5	0.1	-
2024 OM1	70.6	0.5	2.0	1.4	11.2	14.3	S
2024 OO1	24.8	22.1	23.4	1.6	22.5	5.6	-
2024 PA	17.3	23.7	51.3	1.8	5.6	0.3	X
2024 PC	0.1	87.7	8.4	0.0	3.7	0.0	C
2024 PW	0.2	82.9	16.6	0.0	0.3	0.0	C
2024 PC2	0.6	0.3	0.3	0.0	96.7	2.1	Q
2024 PF6	39.5	10.8	44.5	1.2	3.1	0.9	-
2024 QK	46.7	9.9	40.0	0.4	2.2	1.0	-
2024 QS1	47.4	0.0	52.5	0.0	0.0	0.0	X
2024 QV1	0.0	66.8	33.2	0.0	0.0	0.0	C
2024 QK2	0.1	0.0	0.0	0.0	1.5	98.4	V
2024 RW4	0.0	43.9	56.1	0.0	0.0	0.0	X
2024 RH6	1.0	46.6	52.3	0.0	0.1	0.0	X
2024 RT12	1.3	81.1	8.5	0.1	7.3	1.7	C
2024 SQ	0.0	99.9	0.1	0.0	0.0	0.0	C
2024 SA7	76.3	0.4	23.1	0.1	0.1	0.0	S
2024 TA	5.9	58.6	16.6	0.3	13.2	5.5	C
2024 TU3	74.3	1.9	4.2	0.4	4.3	14.9	S
2024 TL5	7.2	37.4	5.1	0.1	13.0	37.3	-
2024 TK7	7.0	54.2	20.1	0.7	14.2	3.8	C
2024 TB22	7.3	38.3	9.6	0.3	35.3	9.2	-
2024 UJ8	2.0	48.0	4.7	0.2	32.2	12.9	-
2024 UT7	90.2	0.0	9.4	0.4	0.0	0.0	S
2024 UB13	23.9	0.6	74.7	0.8	0.1	0.0	X
Total	27.6	28.1	24.4	1.2	10	8.7	100

The final taxonomic classifications of the observations are shown in the pie chart on Figure 26. On the second decision boundary, 72 asteroids bright enough to yield colour

information, 28.1% were identified as X-types, 27.6% as S-types, 25.7% as C-types, 9.9% as Q-types, 8.7% as V-types, and 1.0% as D-types. These classified NEAs had a mean absolute magnitude (H) of 23.7, corresponding to diameters ranging from 44 m to 110 m, depending on their albedo. If we consider S and V types and stony type asteroids, the results match previous studies (Hromakina et al. 2021, Erasmus et al. 2017) that found a 1:1 ratio for (S+Q):(C+X+D) and S:(C+X+D) respectively. It was also found that there were no NEAs that were classified as D types in the second decision boundary, which agrees with previous work done that found D-type asteroids to be rare. A significant number of X-type asteroids were also found, which agrees with Devogèle et al. 2019 and Hromakina et al. 2021 and suggests there could be a higher percentage of X-type asteroids in the small NEA population.

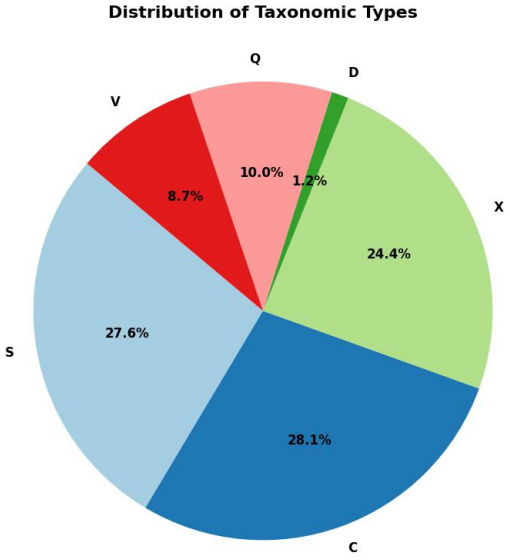

Figure 26: Asteroid taxonomic type distributions from the dataset collected in this project using the second decision boundary surface (see Section 3.2)

4 Conclusion

The MSc project focused on conducting rapid follow-up observations of the small(<300 m) Near-Earth Asteroids (NEAs) population using the 1-meter Lesedi telescope. This work builds upon previous research by Janse (Janse van Rensburg 2021) that successfully observed and characterised 20 NEAs using a 40-inch telescope at the South African Astronomical Observatory's (SAAO) observing site. Observing and characterizing the small NEA population is particularly important because these smaller asteroids are more abundant and have a higher potential for future Earth impact. While over 90% of NEAs larger than 1 kilometre in diameter have been identified, a substantial number of smaller NEAs remain undetected.

With approximately 37,000 NEAs discovered to date, new objects are identified each year through various surveys, with the Catalina Sky Survey (CSS), the Panoramic Survey Telescope and Rapid Response System (PanSTARRS), and the Asteroid Terrestrial-impact Last Alert System (ATLAS) being the most prominent. Given their small size and rapid movement when they come close to Earth, there is only a limited observational window to study them. Failing to observe and characterize these NEAs early could mean that future encounters with Earth remain unmonitored, increasing the risk of unpredicted impacts. Rapid follow-up observations are important because they allow for timely study and classification of these NEAs.

As NEAs frequently pass close to Earth, they also present potential resources for future mining due to their abundance of rare minerals. Gaining a deeper understanding of their composition is essential for devising effective strategies not only for impact prevention but also for resource exploitation. More recently NASAs Double Asteroid Redirection Test (DART; Chabot et al. 2024) mission was the first time an asteroid deflection technique had been successfully tested on the moonlet of asteroid Didymos using a kinetic impactor. Studying the compositions of these NEAs is crucial for determining the appropriate deflection techniques needed, as the NEA population is highly diverse and different types of asteroids would need different deflection techniques. Although observational efforts for small NEAs have grown in recent years, full characterization of these objects remains limited.

In this project, approximately 230 NEAs (including 15 Potentially Hazardous Asteroids, PHAs) with a median absolute magnitude (H) of 24.9, corresponding to a diameter of 35 m - 86 m depending on an assumed albedo of between 0.05 to 0.30, were observed using the Lesedi telescope. Astrometry for these observations was submitted to the Minor Planet Centre (MPC), which assisted in orbit refinement. Taxonomic probabilities were determined for 73 NEAs using a method similar to that of Mommert et al. 2016 and Janse van Rensburg 2021, where a decision surface was generated through machine learning. Colour indices ($g - r$ and $r - i$) were obtained for these 72 asteroids and superimposed on the

decision boundary. A similar decision boundary was also generated using training data from Popescu et al. 2018.

On the first decision boundary surface, generated by Janse van Rensburg 2021, of the 73 asteroids bright enough to yield colour indices, a higher number of D types was found (24.6%) which are not as abundant in the NEA region. A second decision boundary was generated and 27.6% were identified as S-types, 25.7% as C-types, 28.1% as X-types, 1.0% as D-types, 8.7% as V-types, and 9.9% as Q-types. These classified NEAs had a mean absolute magnitude (H) of 23.7, corresponding to diameters ranging from 44 m to 110 m, depending on an assumed albedo of between 0.05 and 0.30. Five of these asteroids were identified as PHAs.

A high number of S-type, X-type and C-type asteroids was found in the second decision boundary. By considering S, V and Q-type asteroids to be stony types, it shows an approximately 1:1 for (S+V+Q):(C+X). This result agrees with Erasmus et al. 2017 who found a similar ratio for S:(C+D) types. Binzel and Rivkin 2001 also found a large number of S and C types. The second major finding was that there was a significant number of X-type asteroids (28%) which is similar to Devogèle et al. 2019 who found 43% (S+Q) but found higher fractions of X-type asteroids (23%). Hromakina et al. 2021 also found 43% of asteroids being S+Q-types, and they also found a significant number of X-type asteroids (19%) as well as C and D-types. In contrast, this projects dataset includes a significant number of fainter objects ($H > 22$), which may have contributed to the lower proportion of S-types and the higher representation of X-types.

This project contributes to the broader understanding of NEA taxonomy, particularly in highlighting the significant presence of X-types and a significant fraction of stony-type asteroids. Future plans include expanding the program to use larger telescopes, such as the SAAO's 74-inch telescope and the South African Large Telescope (SALT), to observe fainter discoveries The project also plans to improve the efficiency of follow-up observations by refining the triggering criteria and automating the data reduction (e.g submitting astrometry to the MPC without human interaction). This could possibly be done using Automated Streak Detection for Astronomical Images (ASTRiDE; Kim 2016), which can be used to detect asteroid streaks.

References

Luis W. Alvarez, Walter Alvarez, Frank Asaro, and Helen V. Michel. Extraterrestrial cause for the cretaceous-tertiary extinction. *Science*, 208(4448):1095–1108, 1980. doi: 10.1126/science.208.4448.1095. URL https://www.science.org/doi/abs/10.1126/science.208.4448.1095.

Richard P. Binzel and Shui Xu. Chips off of asteroid 4 vesta: Evidence for the parent body of basaltic achondrite meteorites. *Science*, 260(5105):186–191, 1993. doi: 10.1126/science.260.5105.186. URL https://www.science.org/doi/abs/10.1126/science.260.5105.186.

Richard P. Binzel, Andrew S. Rivkin, J.Scott Stuart, Alan W. Harris, Schelte J. Bus, and Thomas H. Burbine. Observed spectral properties of near-earth objects: results for population distribution, source regions, and space weathering processes. *Icarus*, 170(2):259–294, 2004. ISSN 0019-1035. doi: https://doi.org/10.1016/j.icarus.2004.04.004. URL https://www.sciencedirect.com/science/article/pii/S0019103504001253.

RP Binzel and A Rivkin. Smithsonian astrophysical observatory. 2001.

W. F. Bottke et al. Debiased orbital and absolute magnitude distribution of the near-earth objects. *Icarus*, 156:399–433, 2002.

William F. Bottke, Daniel D. Durda, David Nesvorný, Robert Jedicke, Alessandro Morbidelli, David Vokrouhlický, and Harold F. Levison. Linking the collisional history of the main asteroid belt to its dynamical excitation and depletion. *Icarus*, 179(1):63–94, 2005. ISSN 0019-1035. doi: https://doi.org/10.1016/j.icarus.2005.05.017. URL https://www.sciencedirect.com/science/article/pii/S0019103505001958.

William F. Bottke, David Vokrouhlický, David P. Rubincam, and David Nesvorný. The yarkovsky and yorp effects: Implications for asteroid dynamics. *Annual Review of Earth and Planetary Sciences*, 34(Volume 34, 2006):157–191, 2006. ISSN 1545-4495. doi: https://doi.org/10.1146/annurev.earth.34.031405.125154. URL https://www.annualreviews.org/content/journals/10.1146/annurev.earth.34.031405.125154.

James M. Brenan and William F. McDonough. Core formation and metal-silicate fractionation of osmium and iridium from gold. *Nature Geoscience*, 2(11):798–801, November 2009. doi: 10.1038/ngeo658.

P. G. Brown, J. D. Assink, L. Astiz, R. Blaauw, M. B. Boslough, J. Borovička, N. Brachet, D. Brown, M. Campbell-Brown, L. Ceranna, W. Cooke, C. de Groot-Hedlin, D. P. Drob, W. Edwards, L. G. Evers, M. Garces, J. Gill, M. Hedlin, A. Kingery, G. Laske,

A. Le Pichon, P. Mialle, D. E. Moser, A. Saffer, E. Silber, P. Smets, R. E. Spalding, P. Spurný, E. Tagliaferri, D. Uren, R. J. Weryk, R. Whitaker, and Z. Krzeminski. A 500-kiloton airburst over chelyabinsk and an enhanced hazard from small impactors. *Nature*, 503(7475):238–241, November 2013. ISSN 1476-4687. doi: 10.1038/nature12741.

Schelte J. Bus and Richard P. Binzel. Phase ii of the small main-belt asteroid spectroscopic survey: A feature-based taxonomy. *Icarus*, 158(1):146–177, 2002. ISSN 0019-1035. doi: https://doi.org/10.1006/icar.2002.6856. URL `https://www.sciencedirect.com/science/article/pii/S0019103502968569`.

Nancy Chabot, Elena Adams, Andy Rivkin, and Jason Kalirai. Dart: Latest results from the dimorphos impact and a look forward to future planetary defense initiatives. *Acta Astronautica*, 220:118–125, 2024. ISSN 0094-5765. doi: https://doi.org/10.1016/j.actaastro.2024.04.001. URL `https://www.sciencedirect.com/science/article/pii/S0094576524002005`.

K. C. Chambers, E. A. Magnier, and Metcalfe. The Pan-STARRS1 Surveys. *arXiv e-prints*, art. arXiv:1612.05560, December 2016. doi: 10.48550/arXiv.1612.05560.

Andrew F. Cheng, Harrison F. Agrusa, Brent W. Barbee, Alex J. Meyer, Tony L. Farnham, Sabina D. Raducan, Derek C. Richardson, Elisabetta Dotto, Angelo Zinzi, Vincenzo Della Corte, Thomas S. Statler, Steven Chesley, Shantanu P. Naidu, Masatoshi Hirabayashi, Jian-Yang Li, Siegfried Eggl, Olivier S. Barnouin, Nancy L. Chabot, Sidney Chocron, Gareth S. Collins, R. Terik Daly, Thomas M. Davison, Mallory E. DeCoster, Carolyn M. Ernst, Fabio Ferrari, Dawn M. Graninger, Seth A. Jacobson, Martin Jutzi, Kathryn M. Kumamoto, Robert Luther, Joshua R. Lyzhoft, Patrick Michel, Naomi Murdoch, Ryota Nakano, Eric Palmer, Andrew S. Rivkin, Daniel J. Scheeres, Angela M. Stickle, Jessica M. Sunshine, Josep M. Trigo-Rodriguez, Jean-Baptiste Vincent, James D. Walker, Kai Wünnemann, Yun Zhang, Marilena Amoroso, Ivano Bertini, John R. Brucato, Andrea Capannolo, Gabriele Cremonese, Massimo Dall'Ora, Prasanna J. D. Deshapriya, Igor Gai, Pedro H. Hasselmann, Simone Ieva, Gabriele Impresario, Stavro L. Ivanovski, Michèle Lavagna, Alice Lucchetti, Elena M. Epifani, Dario Modenini, Maurizio Pajola, Pasquale Palumbo, Davide Perna, Simone Pirrotta, Giovanni Poggiali, Alessandro Rossi, Paolo Tortora, Marco Zannoni, and Giovanni Zanotti. Momentum transfer from the dart mission kinetic impact on asteroid dimorphos. *Nature*, 616(7957):457–460, March 2023. ISSN 1476-4687. doi: 10.1038/s41586-023-05878-z. URL `http://dx.doi.org/10.1038/s41586-023-05878-z`.

E. A. Cloutis, M. J. Gaffey, D. G. W. Smith, and R. St. J. Lambert. Metal Silicate Mixtures: Spectral Properties and Applications to Asteroid Taxonomy. , 95:8323–8338, June 1990. doi: 10.1029/JB095iB06p08323.

Rubin Observatory LSST Solar System Science Collaboration, R. Lynne Jones, Michelle T. Bannister, Bryce T. Bolin, Colin Orion Chandler, Steven R. Chesley, Siegfried Eggl, Sarah Greenstreet, Timothy R. Holt, Henry H. Hsieh, Zeljko Ivezić, Mario Jurić, Michael S. P. Kelley, Matthew M. Knight, Renu Malhotra, William J. Oldroyd, Gal Sarid, Megan E. Schwamb, Colin Snodgrass, Michael Solontoi, and David E. Trilling. The scientific impact of the vera c. rubin observatory's legacy survey of space and time (lsst) for solar system science, 2020. URL https://arxiv.org/abs/2009.07653.

Marco Delbo, Chrysa Avdellidou, and Alessandro Morbidelli. Ancient and primordial collisional families as the main sources of x-type asteroids of the inner main belt. *Astronomy amp; Astrophysics*, 624:A69, April 2019. ISSN 1432-0746. doi: 10.1051/0004-6361/201834745. URL http://dx.doi.org/10.1051/0004-6361/201834745.

F. E. DeMeo and B. Carry. The taxonomic distribution of asteroids from multi-filter all-sky photometric surveys. , 226(1):723–741, September 2013. doi: 10.1016/j.icarus.2013.06.027.

Francesca E. DeMeo, Richard P. Binzel, Stephen M. Slivan, and Schelte J. Bus. An extension of the bus asteroid taxonomy into the near-infrared. *Icarus*, 202(1):160–180, 2009. ISSN 0019-1035. doi: https://doi.org/10.1016/j.icarus.2009.02.005. URL https://www.sciencedirect.com/science/article/pii/S0019103509000554.

Francesca E. DeMeo, Brian J. Burt, Michaël Marsset, David Polishook, Thomas H. Burbine, Benoît Carry, Richard P. Binzel, Pierre Vernazza, Vishnu Reddy, Michelle Tang, Cristina A. Thomas, Andrew S. Rivkin, Nicholas A. Moskovitz, Stephen M. Slivan, and Schelte J. Bus. Connecting asteroids and meteorites with visible and near-infrared spectroscopy. *Icarus*, 380:114971, jul 2022. doi: 10.1016/j.icarus.2022.114971.

H. A. R. Devillepoix, P. A. Bland, E. K. Sansom, M. C. Towner, M. Cupák, R. M. Howie, B. A. D. Hartig, T. Jansen-Sturgeon, and M. A. Cox. Observation of metre-scale impactors by the Desert Fireball Network. , 483(4):5166–5178, March 2019. doi: 10.1093/mnras/sty3442.

Maxime Devogèle, Nicholas Moskovitz, Audrey Thirouin, Annika Gustaffson, Mitchell Magnuson, Cristina Thomas, Mark Willman, Eric Christensen, Michael Person, Richard Binzel, David Polishook, Francesca DeMeo, Mary Hinkle, David Trilling, Michael Mommert, Brian Burt, and Brian Skiff. Visible spectroscopy from the mission accessible near-earth object survey (manos): Taxonomic dependence on asteroid size. *The Astronomical Journal*, 158(5):196, October 2019. ISSN 1538-3881. doi: 10.3847/1538-3881/ab43dd. URL http://dx.doi.org/10.3847/1538-3881/ab43dd.

Linda T. Elkins-Tanton, Benjamin P. Weiss, and Maria T. Zuber. Chondrites as samples of differentiated planetesimals. *Earth and Planetary Science Letters*, 305(1-2):1–10,

May 2011. ISSN 0012-821X. doi: 10.1016/j.epsl.2011.03.010. Funding Information: An NSF Astronomy CAREER grant and the Mitsui Career Development Professorship to L.T.E.-T, a NASA Origins grant and the Victor P. Starr Career Development Professorship to B.P.W., and a NASA/Dawn co-investigator grant to M.T.Z funded this research. The manuscript was improved by reviews by Ian Sanders, Jeff Taylor, and an anonymous reviewer, and by conversations with Hap McSween, David Mittlefehldt, Stein Jacobsen, and Thorsten Kleine.

N. Erasmus, M. Mommert, D. E. Trilling, A. A. Sickafoose, C. van Gend, and J. L. Hora. Characterization of near-earth asteroids using kmtnet-saao. *The Astronomical Journal*, 154(4):162, sep 2017. doi: 10.3847/1538-3881/aa88be. URL https://dx.doi.org/10.3847/1538-3881/aa88be.

N. Erasmus, A. McNeill, M. Mommert, D. E. Trilling, A. A. Sickafoose, and C. van Gend. Taxonomy and Light-curve Data of 1000 Serendipitously Observed Main-belt Asteroids. , 237(1):19, July 2018. doi: 10.3847/1538-4365/aac38f.

N. Erasmus, A. McNeill, M. Mommert, D. E. Trilling, A. A. Sickafoose, and K. Paterson. A Taxonomic Study of Asteroid Families from KMTNET-SAAO Multiband Photometry. , 242(2):15, June 2019. doi: 10.3847/1538-4365/ab1344.

N. Erasmus, Iain Steele, Andrzej S. Piascik, Stuart D. Bates, Christopher J. Mottram, Kathryn Rosie, Carel van Gend, Ulrich Geen, Magaretha L. Pretorius, Stephen B Potter, Egan Loubser, Willie Koorts, Hitesh Gajjar, Keegan Titus, Hannah L. Worters, Amanda A. Sickafoose, Sunil Chandra, James E. O'Connor, Kgothatso Matlala, Justine Crook-Mansour, Ali Ranjbar, Robert J. Smith, Helen E. Jermak, Shalom Abiodun, and O. D. Egbo. Mookodi: multi-purpose low-resolution spectrograph and multi-filter photometric imager for rapid follow-up observations of astronomical transient events. *Journal of Astronomical Telescopes, Instruments, and Systems*, 10:025005 – 025005, 2024. URL https://api.semanticscholar.org/CorpusID:269436196.

S. Fornasier, B.E. Clark, E. Dotto, A. Migliorini, M. Ockert-Bell, and M.A. Barucci. Spectroscopic survey of m-type asteroids. *Icarus*, 210(2):655–673, 2010. ISSN 0019-1035. doi: https://doi.org/10.1016/j.icarus.2010.07.001. URL https://www.sciencedirect.com/science/article/pii/S0019103510002733.

Michael J. Gaffey. Spectral reflectance characteristics of the meteorite classes. *Journal of Geophysical Research (1896-1977)*, 81(5):905–920, 1976. doi: https://doi.org/10.1029/JB081i005p00905. URL https://agupubs.onlinelibrary.wiley.com/doi/abs/10.1029/JB081i005p00905.

Michael J. Gaffey, Jeffrey F. Bell, R. Hamilton Brown, Thomas H. Burbine, Jennifer L.

Piatek, Kevin L. Reed, and Damon A. Chaky. Mineralogical Variations within the S-Type Asteroid Class. , 106(2):573–602, December 1993. doi: 10.1006/icar.1993.1194.

Mikael Granvik, Alessandro Morbidelli, Robert Jedicke, Bryce Bolin, William F. Bottke, Edward Beshore, David Vokrouhlický, David Nesvorný, and Patrick Michel. Debiased orbit and absolute-magnitude distributions for near-earth objects. *Icarus*, 312:181–207, 2018. ISSN 0019-1035. doi: https://doi.org/10.1016/j.icarus.2018.04.018. URL https://www.sciencedirect.com/science/article/pii/S0019103517307017.

Alan W. Harris. On the revision of radiometric albedos and diameters of asteroids. *Icarus*, 126(2):450–454, 1997. ISSN 0019-1035. doi: https://doi.org/10.1006/icar.1996.5664. URL https://www.sciencedirect.com/science/article/pii/S001910359695664X.

Alan W. Harris and Germano D'Abramo. The population of near-earth asteroids. *Icarus*, 257:302–312, 2015. ISSN 0019-1035. doi: https://doi.org/10.1016/j.icarus.2015.05.004. URL https://www.sciencedirect.com/science/article/pii/S0019103515002067.

T. Hromakina, M. Birlan, M. A. Barucci, M. Fulchignoni, F. Colas, S. Fornasier, F. Merlin, A. Sonka, E. Petrescu, D. Perna, and E. Dotto and. Photometric survey of 55 near-earth asteroids. *Astronomy &amp Astrophysics*, 656:A89, dec 2021. doi: 10.1051/0004-6361/202141600.

Peter James, Peter H Schultz, and Adriana C Ocampo. *Comet and asteroid impacts: A planetary geologic history*. Cambridge University Press, 2022.

Petronella Janse van Rensburg. Characterisation of small, close-approaching near-earth asteroids. Master's thesis, Faculty of Science, 2021.

R Lynne Jones, Michelle T Bannister, Bryce T Bolin, Colin Orion Chandler, Steven R Chesley, Siegfried Eggl, Sarah Greenstreet, Timothy R Holt, Henry H Hsieh, Zeljko Ivezić, et al. The scientific impact of the vera c. rubin observatory's legacy survey of space and time (lsst) for solar system science. *arXiv preprint arXiv:2009.07653*, 2020.

Thomas Kenkmann and Natalia A Artemieva. The impact cratering record on earth: The role of space weathering and meteorite flux over time. *Earth and Planetary Science Letters*, 567:116993, 2021.

Dae-Won Kim. ASTRiDE: Automated Streak Detection for Astronomical Images. Astrophysics Source Code Library, record ascl:1605.009, May 2016.

E. L. Krinov. The tunguska meteorite. *International Geology Review*, 2(1):8–19, 1960. doi: 10.1080/00206816009473542. URL https://doi.org/10.1080/00206816009473542.

Dustin Lang, David W. Hogg, Keir Mierle, Michael Blanton, and Sam Roweis. Astrometry.net: Astrometric calibration of images. Astrophysics Source Code Library, record ascl:1208.001, August 2012.

S. Larson, J. Brownlee, C. Hergenrother, and T. Spahr. The Catalina Sky Survey for NEOs. In *Bulletin of the American Astronomical Society*, volume 30, page 1037, September 1998.

Dante S. Lauretta, Heather L. Enos, Anjani T. Polit, Heather L. Roper, and Catherine W.V. Wolner. Chapter 8 - osiris-rex at bennu: Overcoming challenges to collect a sample of the early solar system. In Andrea Longobardo, editor, *Sample Return Missions*, pages 163–194. Elsevier, 2021. ISBN 978-0-12-818330-4. doi: https://doi.org/10.1016/B978-0-12-818330-4.00008-2. URL https://www.sciencedirect.com/science/article/pii/B9780128183304000082.

G. Longo. *The Tunguska Event*, pages 303–330. Springer Berlin Heidelberg, Berlin, Heidelberg, 2007. ISBN 978-3-540-32711-0. doi: 10.1007/978-3-540-32711-0_18. URL https://doi.org/10.1007/978-3-540-32711-0_18.

A. Mainzer, T. Grav, J. Bauer, J. Masiero, R. S. McMillan, R. M. Cutri, R. Walker, E. Wright, P. Eisenhardt, D. J. Tholen, T. Spahr, R. Jedicke, L. Denneau, E. DeBaun, D. Elsbury, T. Gautier, S. Gomillion, E. Hand, W. Mo, J. Watkins, A. Wilkins, G. L. Bryngelson, A. Del Pino Molina, S. Desai, M. Gómez Camus, S. L. Hidalgo, I. Konstantopoulos, J. A. Larsen, C. Maleszewski, M. A. Malkan, J.-C. Mauduit, B. L. Mullan, E. W. Olszewski, J. Pforr, A. Saro, J. V. Scotti, and L. H. Wasserman. Neowise observations of near-earth objects: Preliminary results. *The Astrophysical Journal*, 743 (2):156, December 2011. ISSN 1538-4357. doi: 10.1088/0004-637x/743/2/156. URL http://dx.doi.org/10.1088/0004-637X/743/2/156.

A. Mainzer, T. Grav, J. Bauer, J. Masiero, R. S. McMillan, R. M. Cutri, R. Walker, E. Wright, P. Eisenhardt, D. J. Tholen, T. Spahr, R. Jedicke, L. Denneau, E. DeBaun, D. Elsbury, T. Gautier, S. Gomillion, E. Hand, W. Mo, J. Watkins, A. Wilkins, G. L. Bryngelson, A. Del Pino Molina, S. Desai, M. Gómez Camus, S. L. Hidalgo, I. Konstantopoulos, J. A. Larsen, C. Maleszewski, M. A. Malkan, J. C. Mauduit, B. L. Mullan, E. W. Olszewski, J. Pforr, A. Saro, J. V. Scotti, and L. H. Wasserman. NEOWISE Observations of Near-Earth Objects: Preliminary Results. , 743(2):156, December 2011. doi: 10.1088/0004-637X/743/2/156.

David A. Minton and Renu Malhotra. A record of planet migration in the main asteroid belt. *Nature*, 457(7233):1109–1111, February 2009. ISSN 1476-4687. doi: 10.1038/nature07778. URL http://dx.doi.org/10.1038/nature07778.

M. Mommert. Photometrypipeline: An automated pipeline for calibrated photometry. *Astronomy and Computing*, 18:47–53, 2017. ISSN 2213-1337. doi: https://doi.org/10.1016/j.ascom.2016.11.002. URL https://www.sciencedirect.com/science/article/pii/S2213133716300816.

M. Mommert, D. E. Trilling, D. Borth, R. Jedicke, N. Butler, M. Reyes-Ruiz, B. Pichardo, E. Petersen, T. Axelrod, and N. Moskovitz. First results from the rapid-response spectrophotometric characterization of near-earth objects using ukirt. *The Astronomical Journal*, 151(4):98, March 2016. ISSN 1538-3881. doi: 10.3847/0004-6256/151/4/98. URL http://dx.doi.org/10.3847/0004-6256/151/4/98.

A. Morbidelli, W. Jr, and Patrick Michel. Origin and evolution of near-earth objects. *Asteroids III*, 3, 01 2002.

Alessandro Morbidelli, William F. Bottke, David Nesvorný, and Harold F. Levison. Asteroids were born big. *Icarus*, 204(2):558–573, 2009. ISSN 0019-1035. doi: https://doi.org/10.1016/j.icarus.2009.07.011. URL https://www.sciencedirect.com/science/article/pii/S0019103509003029.

D Perna, E Dotto, S Ieva, MA Barucci, F Bernardi, S Fornasier, F De Luise, E Perozzi, A Rossi, E Mazzotta Epifani, et al. Grasping the nature of potentially hazardous asteroids. *The Astronomical Journal*, 151(1):11, 2015.

A. S. Piascik, Iain A. Steele, Stuart D. Bates, Christopher J. Mottram, R. J. Smith, R. M. Barnsley, and B. Bolton. SPRAT: Spectrograph for the Rapid Acquisition of Transients. In Suzanne K. Ramsay, Ian S. McLean, and Hideki Takami, editors, *Ground-based and Airborne Instrumentation for Astronomy V*, volume 9147 of *Society of Photo-Optical Instrumentation Engineers (SPIE) Conference Series*, page 91478H, July 2014. doi: 10.1117/12.2055117.

M. Popescu, J. Licandro, J. M. Carvano, R. Stoicescu, J. de León, D. Morate, I. L. Boacă, and C. P. Cristescu. Taxonomic classification of asteroids based on movis near-infrared colors. *Astronomy amp; Astrophysics*, 617:A12, September 2018. ISSN 1432-0746. doi: 10.1051/0004-6361/201833023. URL http://dx.doi.org/10.1051/0004-6361/201833023.

M. Popescu, O. Vaduvescu, J. de León, R. M. Gherase, J. Licandro, I. L. Boacă, A. B. Şonka, R. P. Ashley, T. Močnik, D. Morate, M. Predatu, M. De Prá, C. Fariña, H. Stoev, M. Díaz Alfaro, I. Ordonez-Etxeberria, F. López-Martínez, and R. Errmann. Near-earth asteroids spectroscopic survey atiisaac newton/itelescope. *Astronomy &amp Astrophysics*, 627:A124, jul 2019. doi: 10.1051/0004-6361/201935006.

Marcel Popescu, Julia de León, Javier Licandro, Gabriel Nicolae Simion, David Morate, Ovidiu Văduvescu, Juan Luis Rizos, Hissa Medeiros, and Radu Mihai Gherase. Simultaneous observations in four optical bands of near-Earth asteroids using TCS/MuSCAT2 instrument. In *European Planetary Science Congress*, pages EPSC2021–820, September 2021. doi: 10.5194/epsc2021-820.

Olga P. Popova, Peter Jenniskens, Vacheslav Emel'yanenko, Anna Kartashova, Eugeny Biryukov, Sergey Khaibrakhmanov, Valery Shuvalov, Yurij Rybnov, Alexandr Dudorov, Victor I. Grokhovsky, Dmitry D. Badyukov, Qing-Zhu Yin, Peter S. Gural, Jim Albers, Mikael Granvik, Läslo G. Evers, Jacob Kuiper, Vladimir Kharlamov, Andrey Solovyov, Yuri S. Rusakov, Stanislav Korotkiy, Ilya Serdyuk, Alexander V. Korochantsev, Michail Yu. Larionov, Dmitry Glazachev, Alexander E. Mayer, Galen Gisler, Sergei V. Gladkovsky, Josh Wimpenny, Matthew E. Sanborn, Akane Yamakawa, Kenneth L. Verosub, Douglas J. Rowland, Sarah Roeske, Nicholas W. Botto, Jon M. Friedrich, Michael E. Zolensky, Loan Le, Daniel Ross, Karen Ziegler, Tomoki Nakamura, Insu Ahn, Jong Ik Lee, Qin Zhou, Xian-Hua Li, Qiu-Li Li, Yu Liu, Guo-Qiang Tang, Takahiro Hiroi, Derek Sears, Ilya A. Weinstein, Alexander S. Vokhmintsev, Alexei V. Ishchenko, Phillipe Schmitt-Kopplin, Norbert Hertkorn, Keisuke Nagao, Makiko K. Haba, Mutsumi Komatsu, Takashi Mikouchi, and (the Chelyabinsk Airburst Consortium). Chelyabinsk airburst, damage assessment, meteorite recovery, and characterization. *Science*, 342(6162):1069–1073, 2013. doi: 10.1126/science.1242642. URL `https://www.science.org/doi/abs/10.1126/science.1242642`.

Stephen B. Potter. Towards an Intelligent Observatory. *Anais da Academia Brasileira de Ciências*, 93:1, May 2021. doi: 10.1590/0001-3756202120201026.

Sean N. Raymond and David Nesvorný . Origin and dynamical evolution of the asteroid belt. In *Vesta and Ceres*, pages 227–249. Cambridge University Press, mar 2022. doi: 10.1017/9781108856324.019. URL `https://doi.org/10.1017%2F9781108856324.019`.

John Smith. *Introduction to Planetary Science*. Academic Press, New York, 2020.

David James Tholen. *Asteroid Taxonomy from Cluster Analysis of Photometry.* PhD thesis, University of Arizona, September (1984).

J. L. Tonry, L. Denneau, A. N. Heinze, B. Stalder, K. W. Smith, S. J. Smartt, C. W. Stubbs, H. J. Weiland, and A. Rest. ATLAS: A High-cadence All-sky Survey System. , 130(988):064505, June 2018. doi: 10.1088/1538-3873/aabadf.

S. Watanabe, M. Hirabayashi, N. Hirata, Na. Hirata, R. Noguchi, Y. Shimaki, H. Ikeda, E. Tatsumi, M. Yoshikawa, S. Kikuchi, H. Yabuta, T. Nakamura, S. Tachibana, Y. Ishihara, T. Morota, K. Kitazato, N. Sakatani, K. Matsumoto, K. Wada, H. Senshu, C. Honda, T. Michikami, H. Takeuchi, T. Kouyama, R. Honda, S. Kameda, T. Fuse,

H. Miyamoto, G. Komatsu, S. Sugita, T. Okada, N. Namiki, M. Arakawa, M. Ishiguro, M. Abe, R. Gaskell, E. Palmer, O. S. Barnouin, P. Michel, A. S. French, J. W. McMahon, D. J. Scheeres, P. A. Abell, Y. Yamamoto, S. Tanaka, K. Shirai, M. Matsuoka, M. Yamada, Y. Yokota, H. Suzuki, K. Yoshioka, Y. Cho, S. Tanaka, N. Nishikawa, T. Sugiyama, H. Kikuchi, R. Hemmi, T. Yamaguchi, N. Ogawa, G. Ono, Y. Mimasu, K. Yoshikawa, T. Takahashi, Y. Takei, A. Fujii, C. Hirose, T. Iwata, M. Hayakawa, S. Hosoda, O. Mori, H. Sawada, T. Shimada, S. Soldini, H. Yano, R. Tsukizaki, M. Ozaki, Y. Iijima, K. Ogawa, M. Fujimoto, T. M. Ho, A. Moussi, R. Jaumann, J. P. Bibring, C. Krause, F. Terui, T. Saiki, S. Nakazawa, and Y. Tsuda. Hayabusa2 arrives at the carbonaceous asteroid 162173 Ryugu—A spinning top-shaped rubble pile. *Science*, 364(6437):268–272, April 2019. doi: 10.1126/science.aav8032.

Hannah L. Worters, James E. O'Connor, David B. Carter, Egan Loubser, Pieter A. Fourie, Amanda Sickafoose, and Pieter Swanevelder. SAAO's new robotic telescope and WiNCam (Wide-field Nasmyth Camera). In Christopher J. Evans, Luc Simard, and Hideki Takami, editors, *Ground-based and Airborne Instrumentation for Astronomy VI*, volume 9908 of *Society of Photo-Optical Instrumentation Engineers (SPIE) Conference Series*, page 99083Y, August 2016. doi: 10.1117/12.2231636.

B. Zellner, D.J. Tholen, and E.F. Tedesco. The eight-color asteroid survey: Results for 589 minor planets. *Icarus*, 61(3):355–416, 1985. ISSN 0019-1035. doi: https://doi.org/10.1016/0019-1035(85)90133-2. URL `https://www.sciencedirect.com/science/article/pii/0019103585901332`.

A Appendix A: Photometric Observations of Near-Earth Asteroids in g, r, and i filters

The grid below shows the photometry obtained from 72 of the observed NEAs as well as the legend for all plots below.

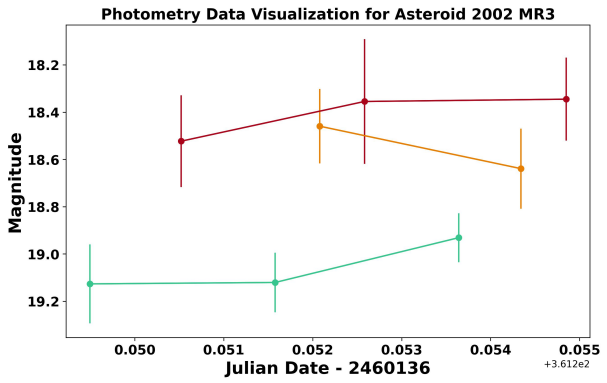

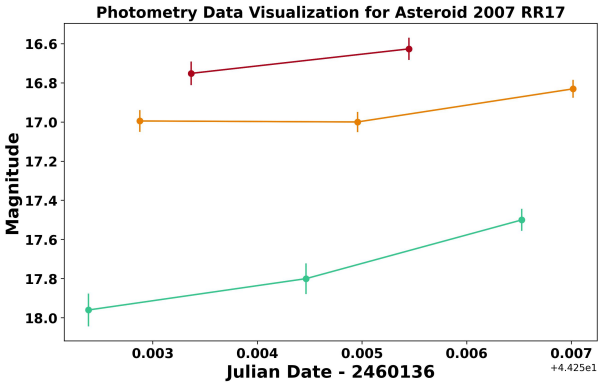

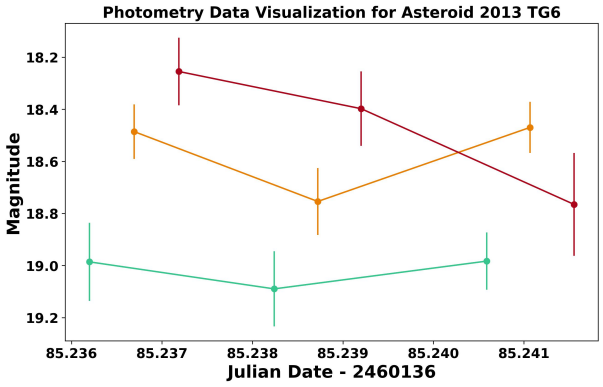

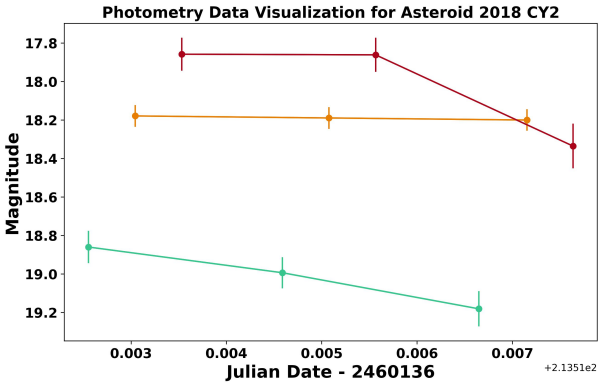

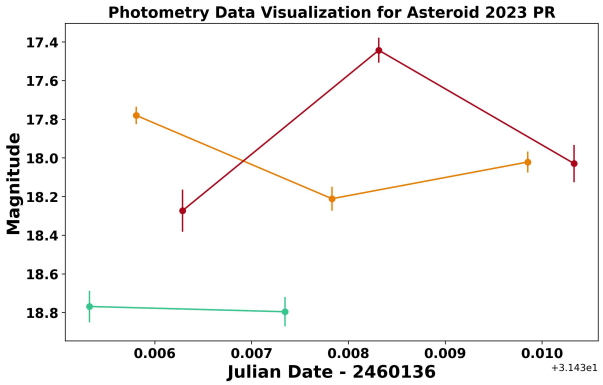
Photometry Data Visualization for Asteroid 2023 PR
Magnitude
17.4
17.6
17.8
18.0
18.2
18.4
18.6
18.8
0.006
0.007
0.008
0.009
0.010
Julian Date - 2460136
+3.143e1

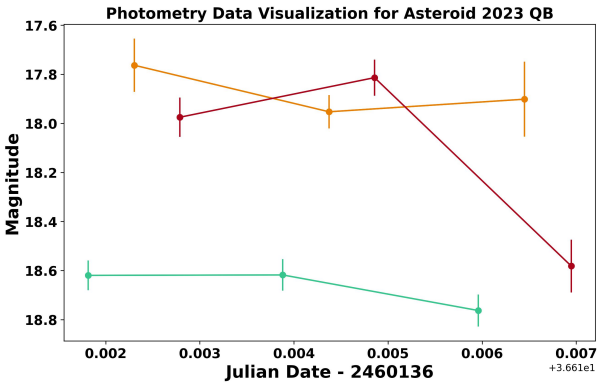
Photometry Data Visualization for Asteroid 2023 QB
Magnitude
17.6
17.8
18.0
18.2
18.4
18.6
18.8
0.002
0.003
0.004
0.005
0.006
0.007
Julian Date - 2460136
+3.661e1

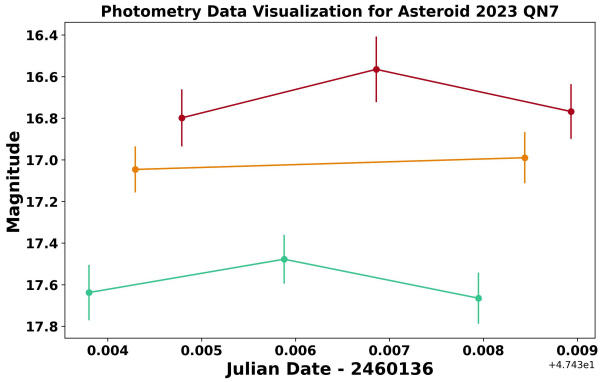
Photometry Data Visualization for Asteroid 2023 QN7
Magnitude
16.4
16.6
16.8
17.0
17.2
17.4
17.6
17.8
0.004
0.005
0.006
0.007
0.008
0.009
Julian Date - 2460136
+4.743e1

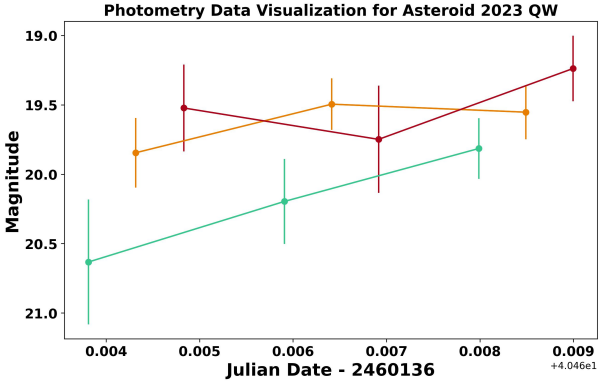
Photometry Data Visualization for Asteroid 2023 QW
Magnitude
19.0
19.5
20.0
20.5
21.0
0.004
0.005
0.006
0.007
0.008
0.009
Julian Date - 2460136
+4.046e1

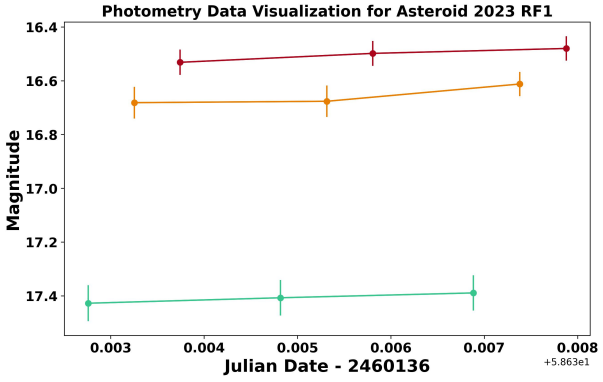
Photometry Data Visualization for Asteroid 2023 RF1
Magnitude
16.4
16.6
16.8
17.0
17.2
17.4
0.003
0.004
0.005
0.006
0.007
0.008
Julian Date - 2460136
+5.863e1

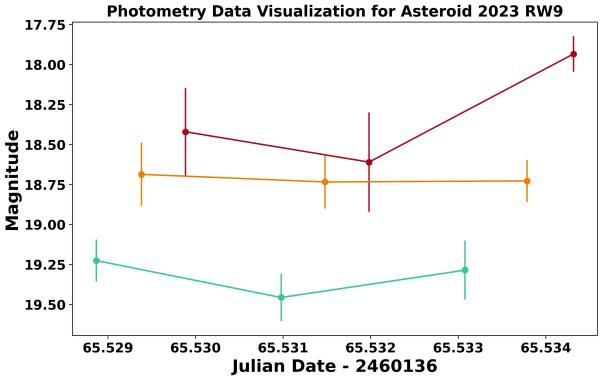
Photometry Data Visualization for Asteroid 2023 RW9
Magnitude
17.75
18.00
18.25
18.50
18.75
19.00
19.25
19.50
65.529
65.530
65.531
65.532
65.533
65.534
Julian Date - 2460136

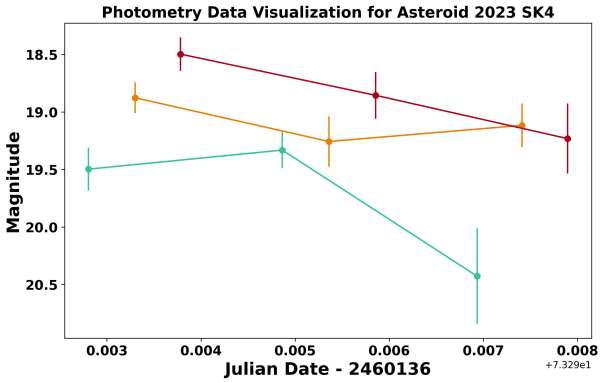
Photometry Data Visualization for Asteroid 2023 SK4
Magnitude
Julian Date - 2460136
+7.329e1

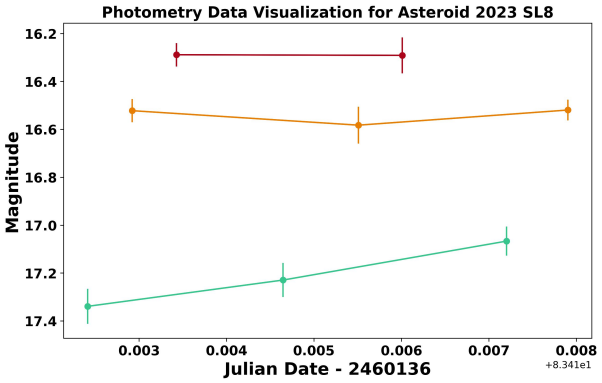
Photometry Data Visualization for Asteroid 2023 SL8
Magnitude
Julian Date - 2460136
+8.341e1

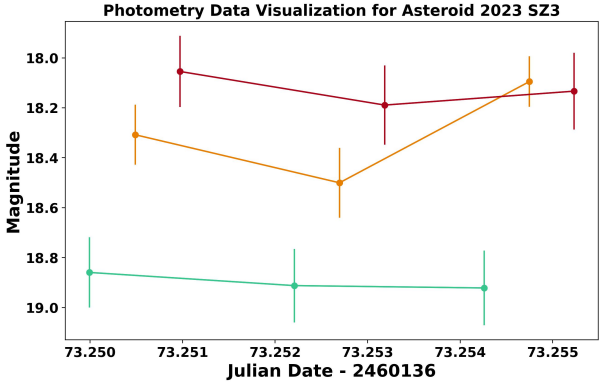
Photometry Data Visualization for Asteroid 2023 SZ3
Magnitude
Julian Date - 2460136

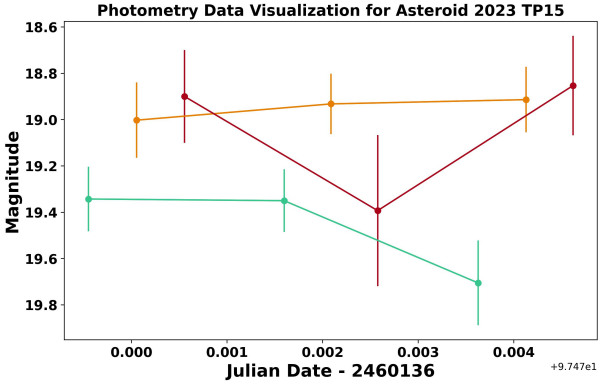
Photometry Data Visualization for Asteroid 2023 TP15
Magnitude
Julian Date - 2460136
+9.747e1

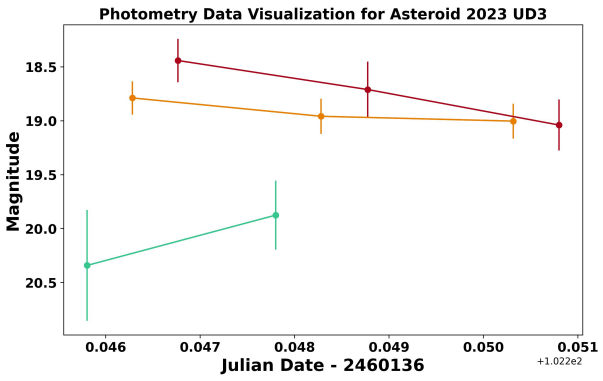
Photometry Data Visualization for Asteroid 2023 UD3
Magnitude
Julian Date - 2460136
+1.022e2

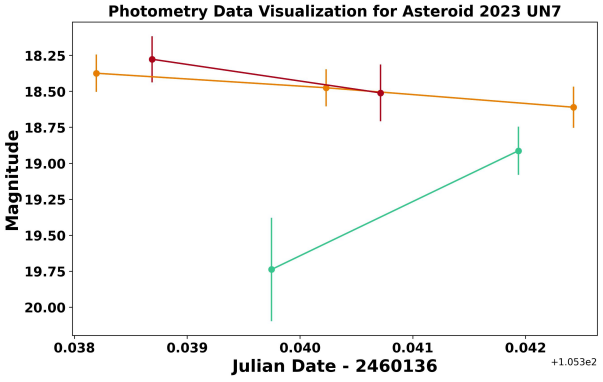
Photometry Data Visualization for Asteroid 2023 UN7
Magnitude
Julian Date - 2460136
+1.053e2

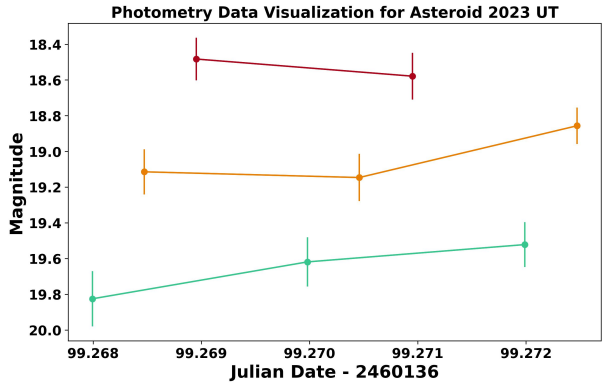
Photometry Data Visualization for Asteroid 2023 UT
Magnitude
Julian Date - 2460136

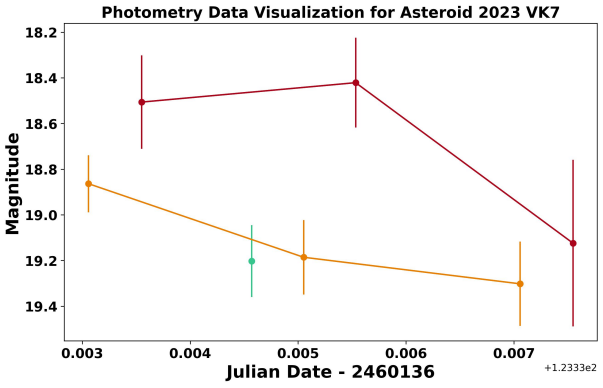
Photometry Data Visualization for Asteroid 2023 VK7
Magnitude
Julian Date - 2460136
+1.2333e2

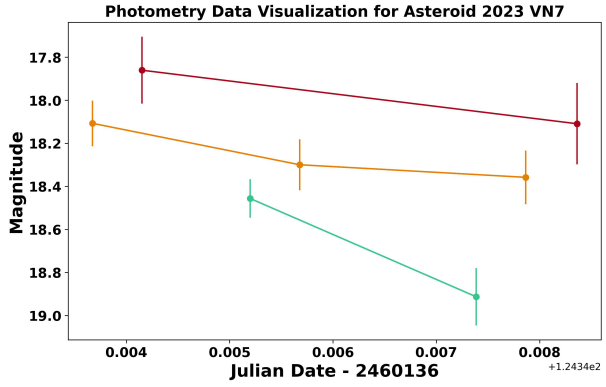
Photometry Data Visualization for Asteroid 2023 VN7
Magnitude
Julian Date - 2460136
+1.2434e2

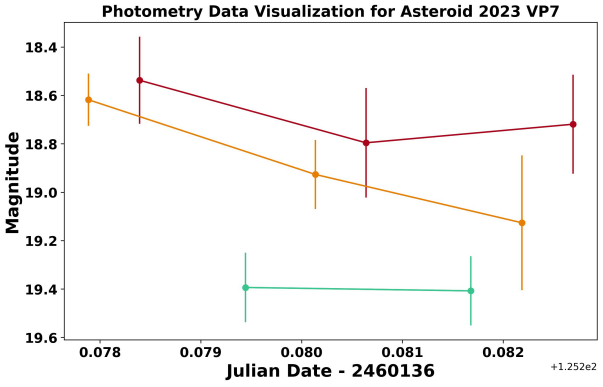
Photometry Data Visualization for Asteroid 2023 VP7
Magnitude
Julian Date - 2460136
+1.252e2

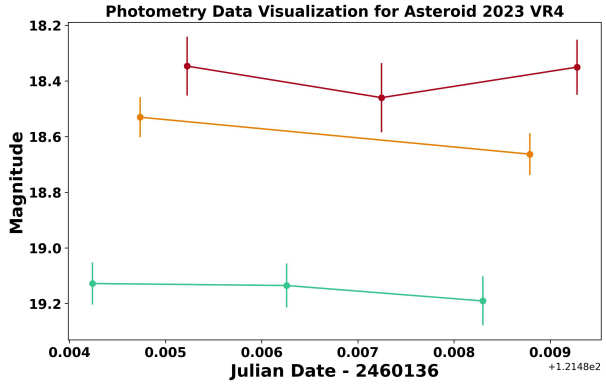
Photometry Data Visualization for Asteroid 2023 VR4
Magnitude
Julian Date - 2460136
+1.2148e2

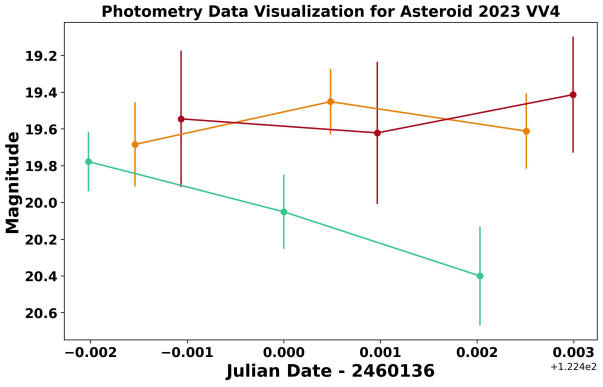
Photometry Data Visualization for Asteroid 2023 VV4
Magnitude
Julian Date - 2460136
+1.224e2

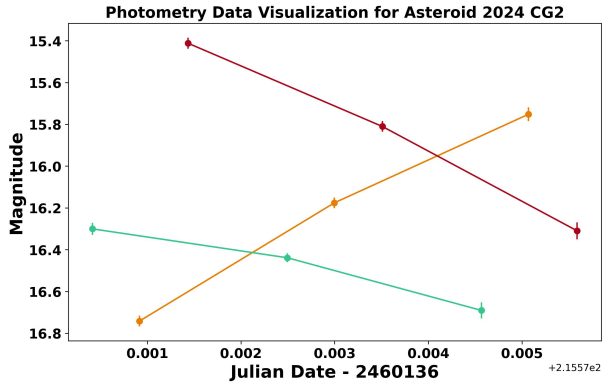
Photometry Data Visualization for Asteroid 2024 CG2
Magnitude
15.4
15.6
15.8
16.0
16.2
16.4
16.6
16.8
0.001
0.002
0.003
0.004
0.005
Julian Date - 2460136
+2.1557e2

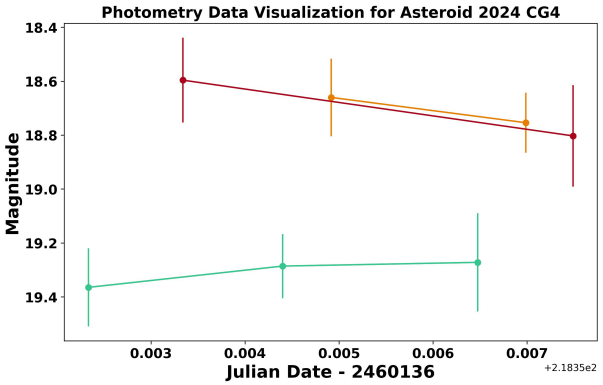
Photometry Data Visualization for Asteroid 2024 CG4
Magnitude
18.4
18.6
18.8
19.0
19.2
19.4
0.003
0.004
0.005
0.006
0.007
Julian Date - 2460136
+2.1835e2

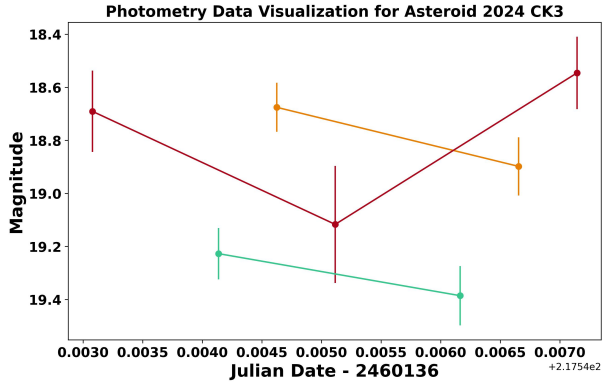
Photometry Data Visualization for Asteroid 2024 CK3
Magnitude
18.4
18.6
18.8
19.0
19.2
19.4
0.0030
0.0035
0.0040
0.0045
0.0050
0.0055
0.0060
0.0065
0.0070
Julian Date - 2460136
+2.1754e2

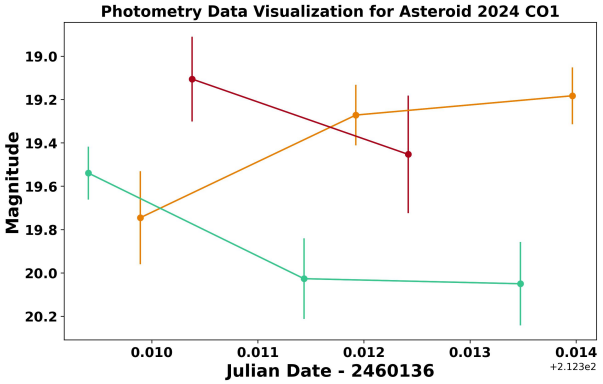
Photometry Data Visualization for Asteroid 2024 CO1
Magnitude
19.0
19.2
19.4
19.6
19.8
20.0
20.2
0.010
0.011
0.012
0.013
0.014
Julian Date - 2460136
+2.123e2

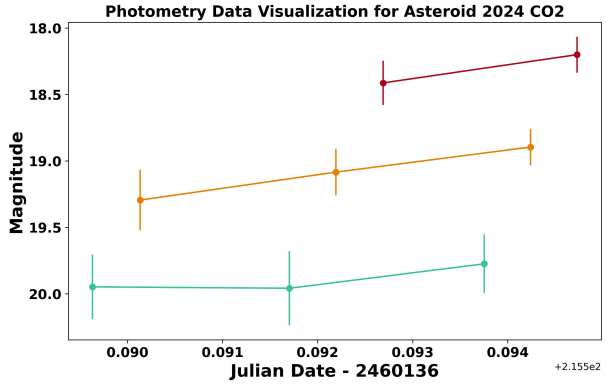
Photometry Data Visualization for Asteroid 2024 CO2
Magnitude
18.0
18.5
19.0
19.5
20.0
0.090
0.091
0.092
0.093
0.094
Julian Date - 2460136
+2.155e2

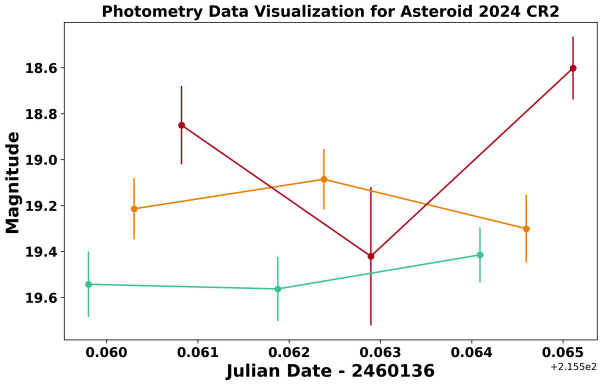
Photometry Data Visualization for Asteroid 2024 CR2
Magnitude
18.6
18.8
19.0
19.2
19.4
19.6
0.060
0.061
0.062
0.063
0.064
0.065
Julian Date - 2460136
+2.155e2

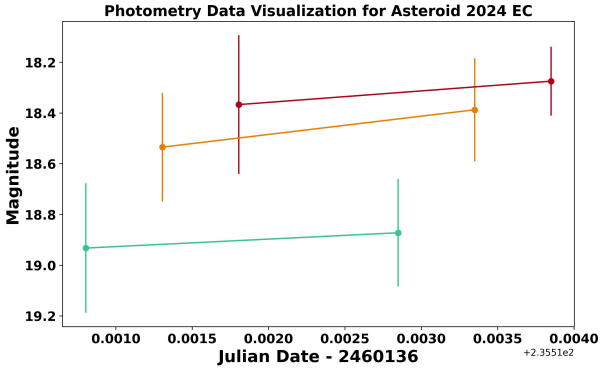
Photometry Data Visualization for Asteroid 2024 EC
Magnitude
Julian Date - 2460136
+2.3551e2

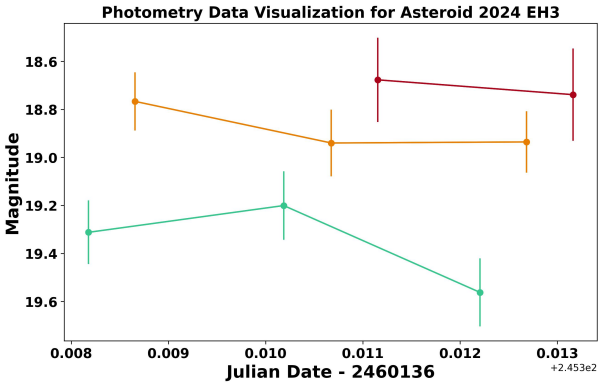
Photometry Data Visualization for Asteroid 2024 EH3
Magnitude
Julian Date - 2460136
+2.453e2

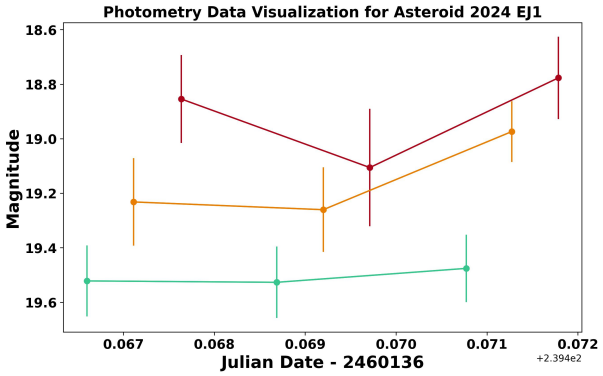
Photometry Data Visualization for Asteroid 2024 EJ1
Magnitude
Julian Date - 2460136
+2.394e2

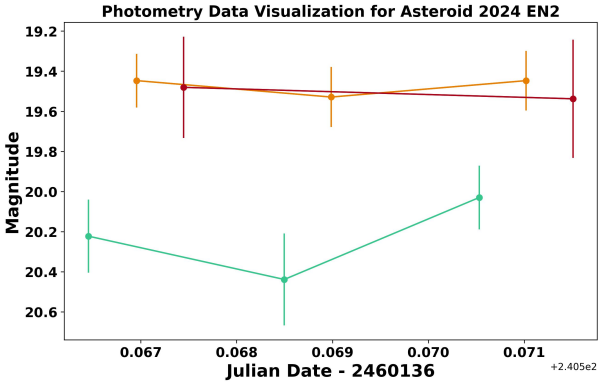
Photometry Data Visualization for Asteroid 2024 EN2
Magnitude
Julian Date - 2460136
+2.405e2

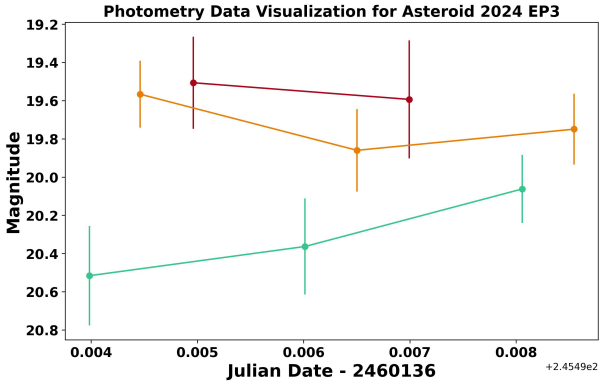
Photometry Data Visualization for Asteroid 2024 EP3
Magnitude
Julian Date - 2460136
+2.4549e2

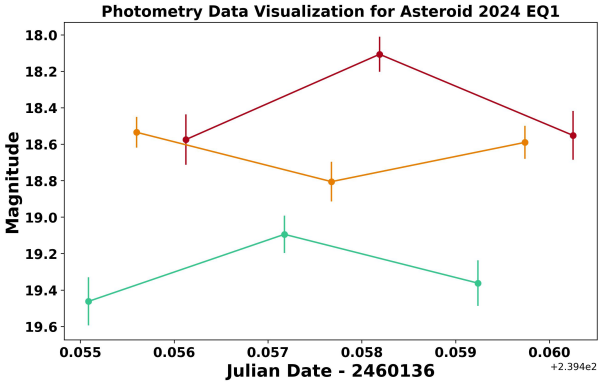
Photometry Data Visualization for Asteroid 2024 EQ1
Magnitude
Julian Date - 2460136
+2.394e2

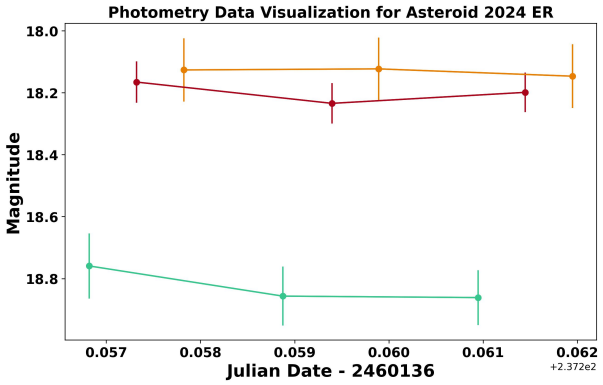
Photometry Data Visualization for Asteroid 2024 ER
Magnitude
Julian Date - 2460136
+2.372e2

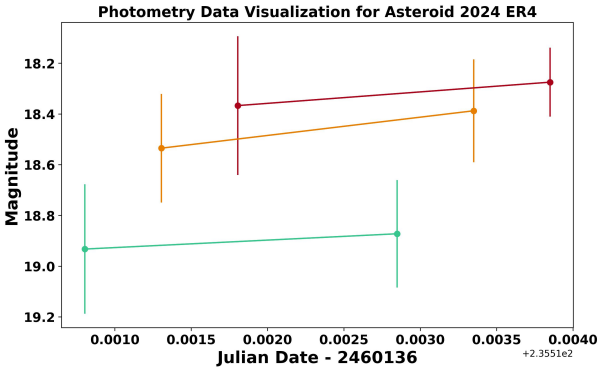
Photometry Data Visualization for Asteroid 2024 ER4
Magnitude
Julian Date - 2460136
+2.3551e2

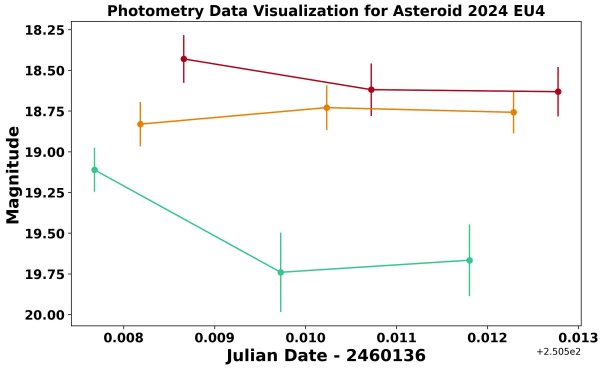
Photometry Data Visualization for Asteroid 2024 EU4
Magnitude
Julian Date - 2460136
+2.505e2

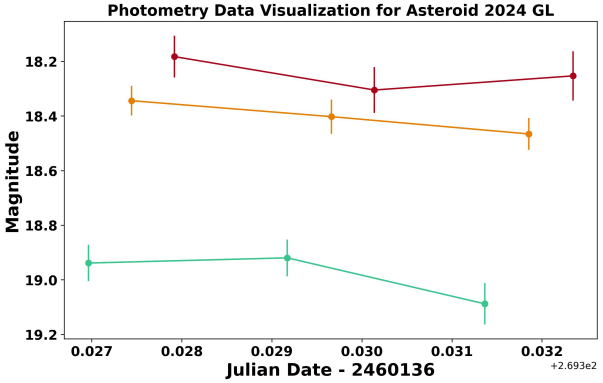
Photometry Data Visualization for Asteroid 2024 GL
Magnitude
Julian Date - 2460136
+2.693e2

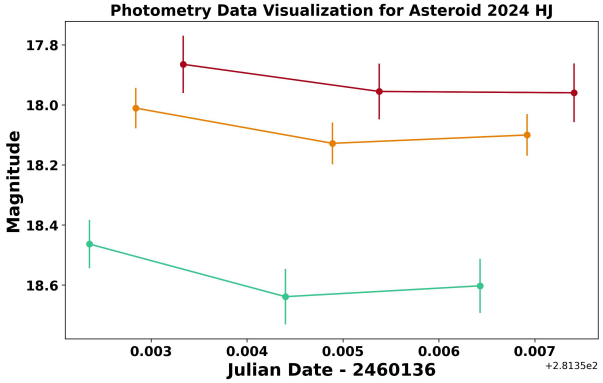
Photometry Data Visualization for Asteroid 2024 HJ
Magnitude
Julian Date - 2460136
+2.8135e2

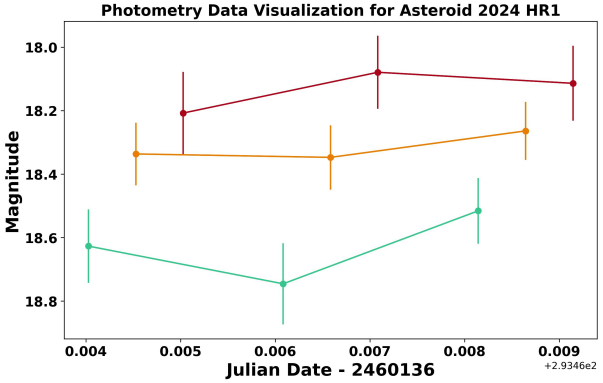
Photometry Data Visualization for Asteroid 2024 HR1
Magnitude
Julian Date - 2460136
+2.9346e2

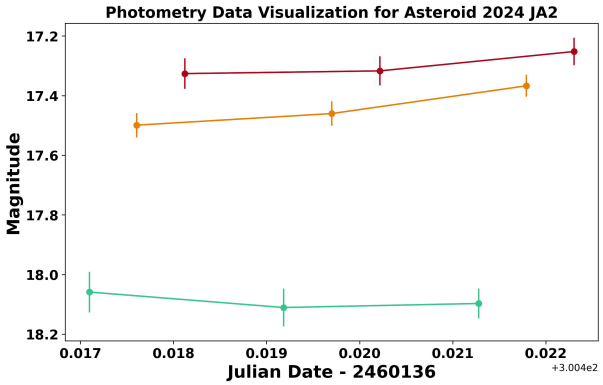
Photometry Data Visualization for Asteroid 2024 JA2
Magnitude
17.2
17.4
17.6
17.8
18.0
18.2
0.017
0.018
0.019
0.020
0.021
0.022
Julian Date - 2460136
+3.004e2

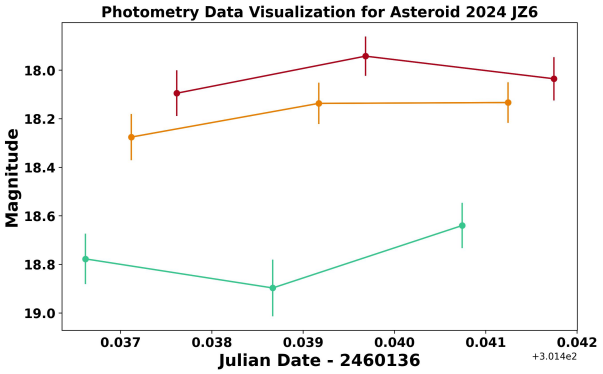
Photometry Data Visualization for Asteroid 2024 JZ6
Magnitude
18.0
18.2
18.4
18.6
18.8
19.0
0.037
0.038
0.039
0.040
0.041
0.042
Julian Date - 2460136
+3.014e2

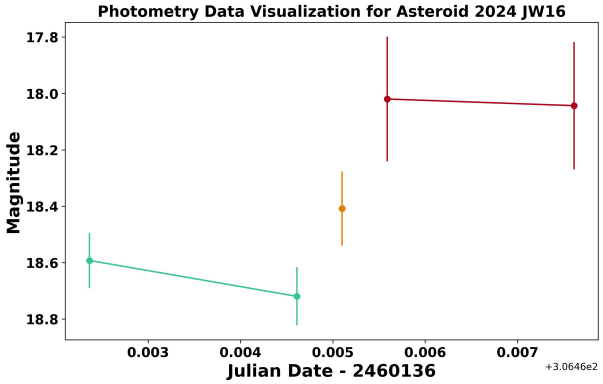
Photometry Data Visualization for Asteroid 2024 JW16
Magnitude
17.8
18.0
18.2
18.4
18.6
18.8
0.003
0.004
0.005
0.006
0.007
Julian Date - 2460136
+3.0646e2

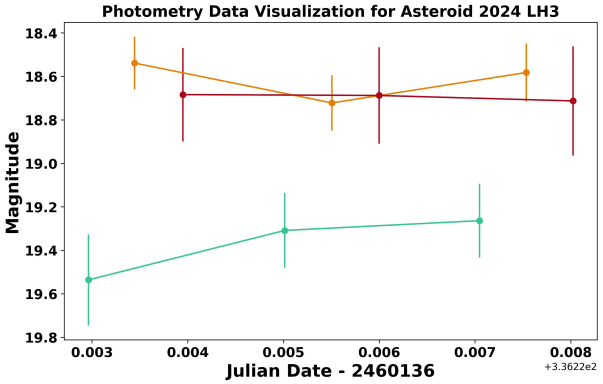
Photometry Data Visualization for Asteroid 2024 LH3
Magnitude
18.4
18.6
18.8
19.0
19.2
19.4
19.6
19.8
0.003
0.004
0.005
0.006
0.007
0.008
Julian Date - 2460136
+3.3622e2

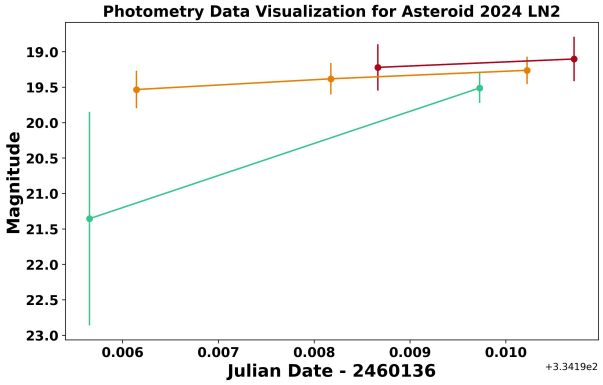
Photometry Data Visualization for Asteroid 2024 LN2
Magnitude
19.0
19.5
20.0
20.5
21.0
21.5
22.0
22.5
23.0
0.006
0.007
0.008
0.009
0.010
Julian Date - 2460136
+3.3419e2

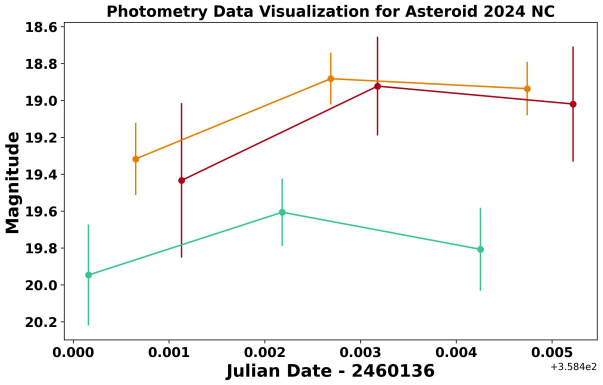
Photometry Data Visualization for Asteroid 2024 NC
Magnitude
18.6
18.8
19.0
19.2
19.4
19.6
19.8
20.0
20.2
0.000
0.001
0.002
0.003
0.004
0.005
Julian Date - 2460136
+3.584e2

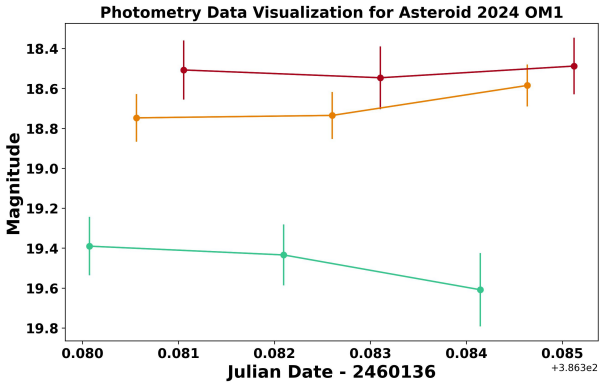
Photometry Data Visualization for Asteroid 2024 OM1
Magnitude
Julian Date - 2460136
+3.863e2

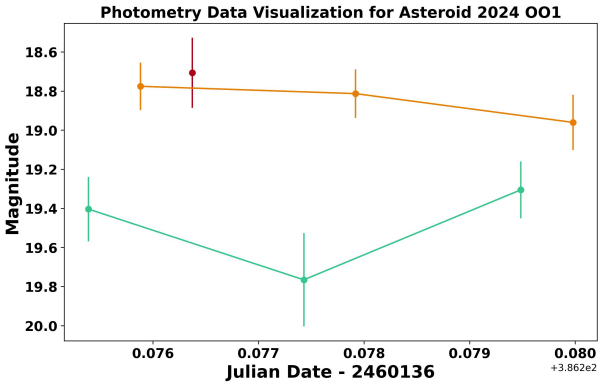
Photometry Data Visualization for Asteroid 2024 OO1
Magnitude
Julian Date - 2460136
+3.862e2

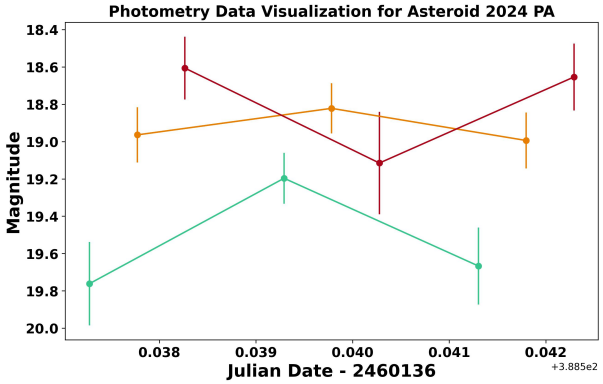
Photometry Data Visualization for Asteroid 2024 PA
Magnitude
Julian Date - 2460136
+3.885e2

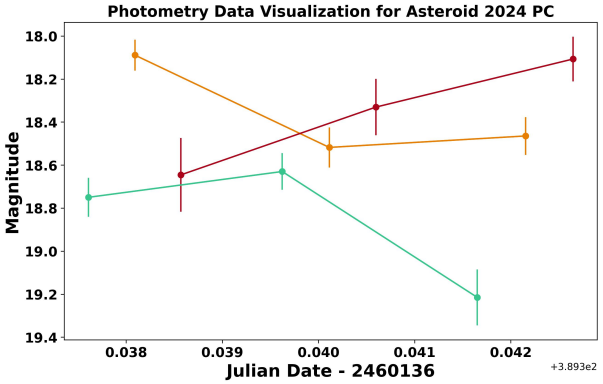
Photometry Data Visualization for Asteroid 2024 PC
Magnitude
Julian Date - 2460136
+3.893e2

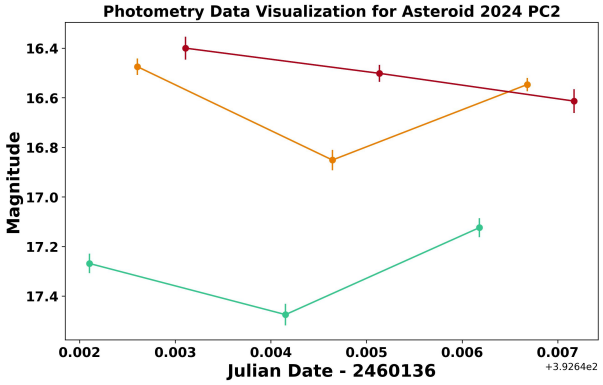
Photometry Data Visualization for Asteroid 2024 PC2
Magnitude
Julian Date - 2460136
+3.9264e2

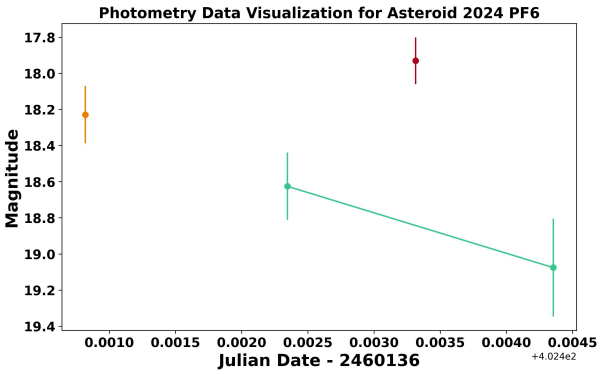
Photometry Data Visualization for Asteroid 2024 PF6
Magnitude
Julian Date - 2460136
+4.024e2

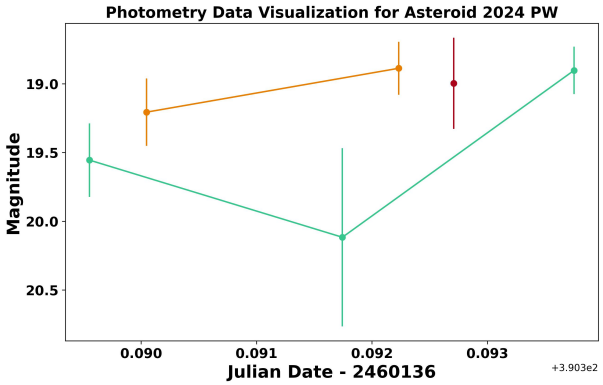
Photometry Data Visualization for Asteroid 2024 PW
Magnitude
19.0
19.5
20.0
20.5
0.090
0.091
0.092
0.093
Julian Date - 2460136
+3.903e2

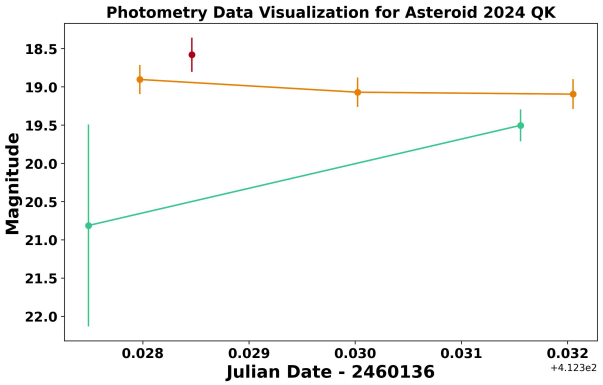
Photometry Data Visualization for Asteroid 2024 QK
Magnitude
18.5
19.0
19.5
20.0
20.5
21.0
21.5
22.0
0.028
0.029
0.030
0.031
0.032
Julian Date - 2460136
+4.123e2

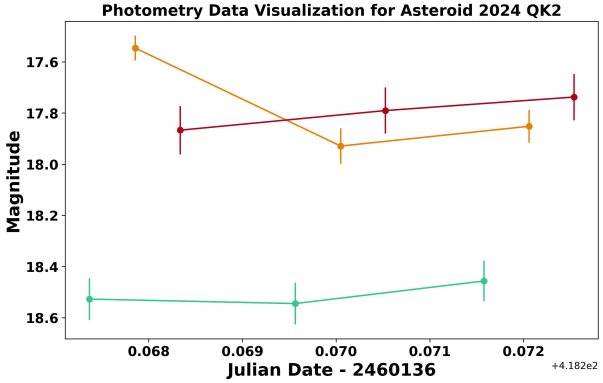
Photometry Data Visualization for Asteroid 2024 QK2
Magnitude
17.6
17.8
18.0
18.2
18.4
18.6
0.068
0.069
0.070
0.071
0.072
Julian Date - 2460136
+4.182e2

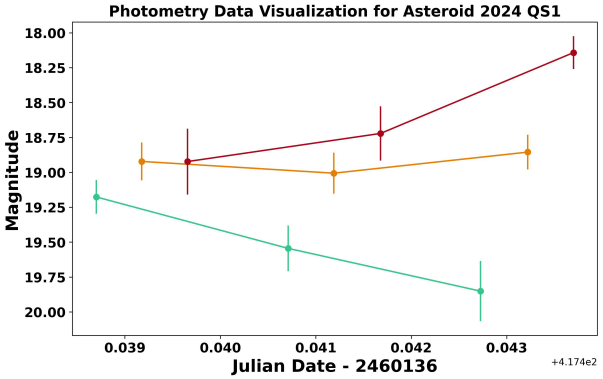
Photometry Data Visualization for Asteroid 2024 QS1
Magnitude
18.00
18.25
18.50
18.75
19.00
19.25
19.50
19.75
20.00
0.039
0.040
0.041
0.042
0.043
Julian Date - 2460136
+4.174e2

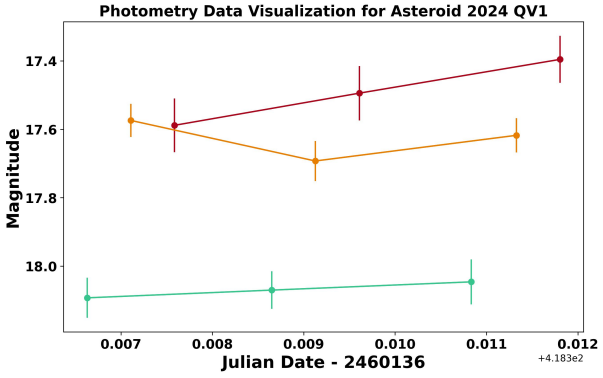
Photometry Data Visualization for Asteroid 2024 QV1
Magnitude
17.4
17.6
17.8
18.0
0.007
0.008
0.009
0.010
0.011
0.012
Julian Date - 2460136
+4.183e2

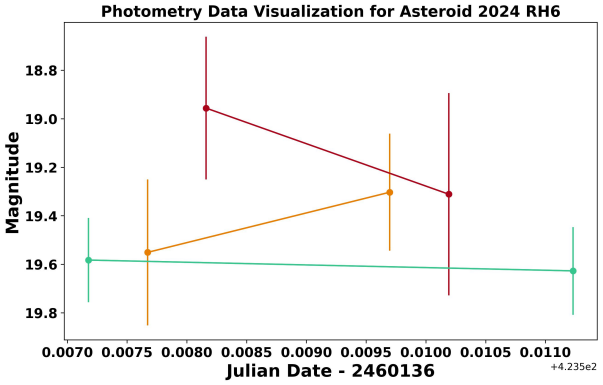
Photometry Data Visualization for Asteroid 2024 RH6
Magnitude
18.8
19.0
19.2
19.4
19.6
19.8
0.0070
0.0075
0.0080
0.0085
0.0090
0.0095
0.0100
0.0105
0.0110
Julian Date - 2460136
+4.235e2

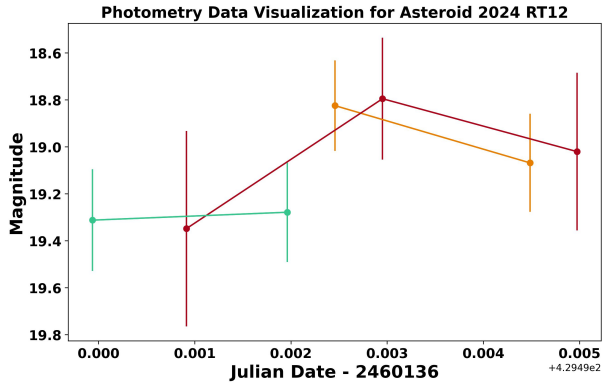
Photometry Data Visualization for Asteroid 2024 RT12
Magnitude
Julian Date - 2460136
+4.2949e2

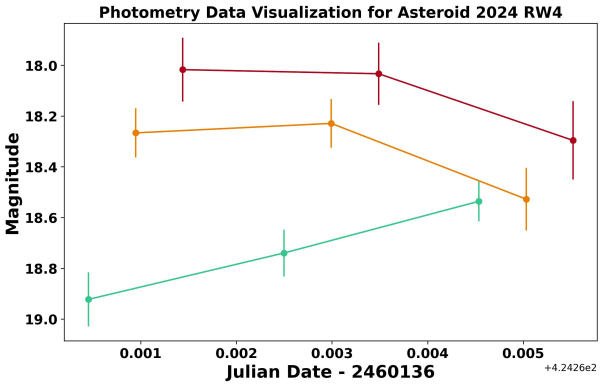
Photometry Data Visualization for Asteroid 2024 RW4
Magnitude
Julian Date - 2460136
+4.2426e2

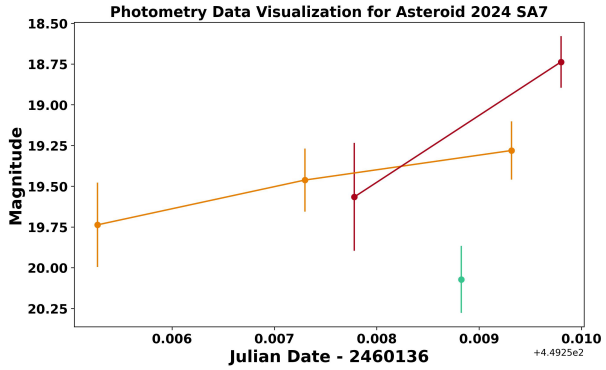
Photometry Data Visualization for Asteroid 2024 SA7
Magnitude
Julian Date - 2460136
+4.4925e2

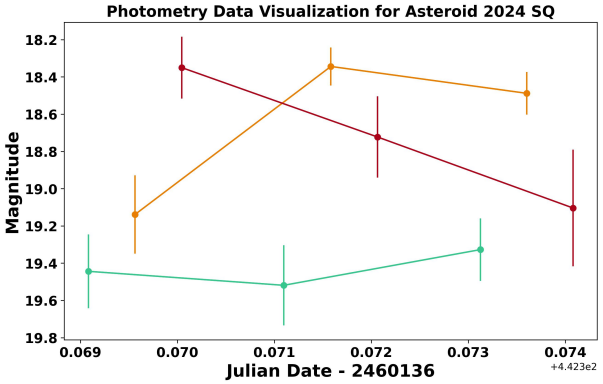
Photometry Data Visualization for Asteroid 2024 SQ
Magnitude
Julian Date - 2460136
+4.423e2

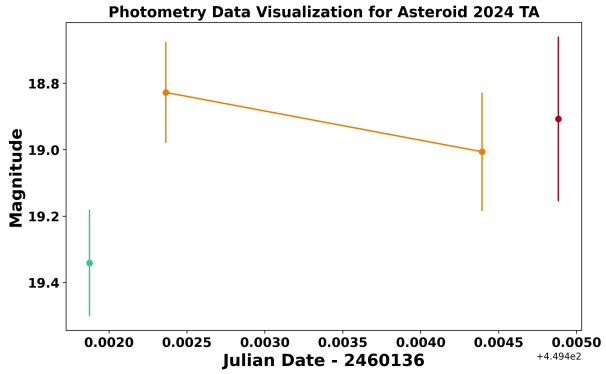
Photometry Data Visualization for Asteroid 2024 TA
Magnitude
Julian Date - 2460136
+4.494e2

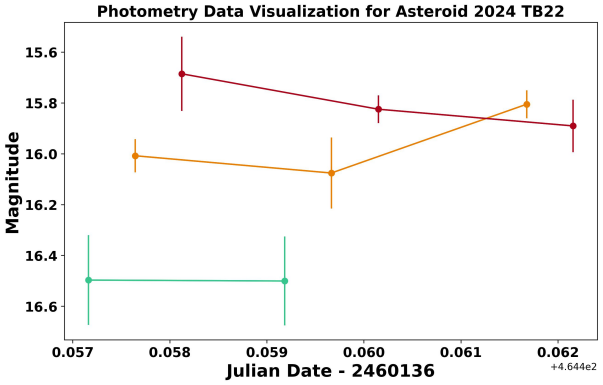
Photometry Data Visualization for Asteroid 2024 TB22
Magnitude
Julian Date - 2460136
+4.644e2

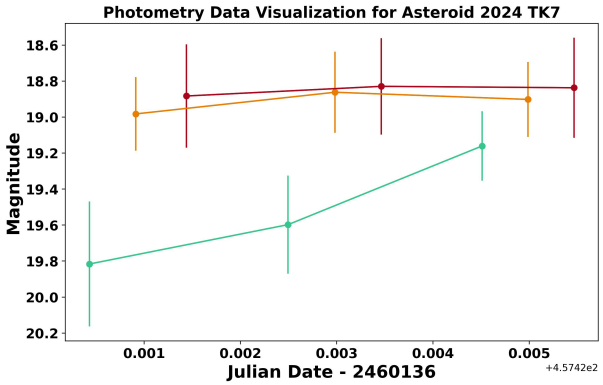
Photometry Data Visualization for Asteroid 2024 TK7
Magnitude
Julian Date - 2460136
+4.5742e2

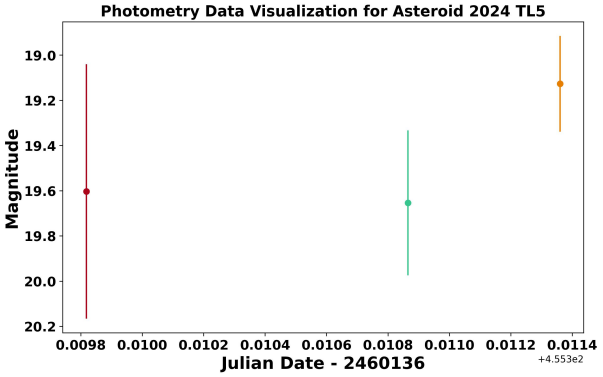
Photometry Data Visualization for Asteroid 2024 TL5
Magnitude
Julian Date - 2460136
+4.553e2

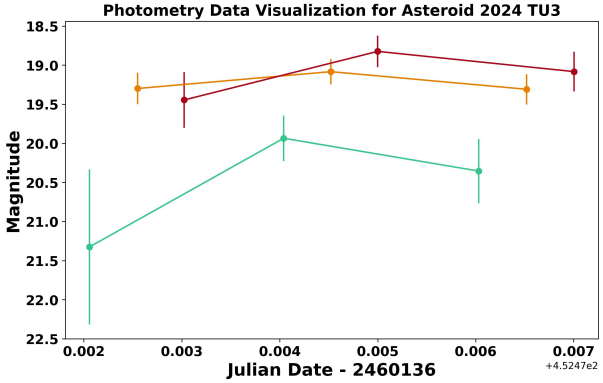
Photometry Data Visualization for Asteroid 2024 TU3
Magnitude
Julian Date - 2460136
+4.5247e2

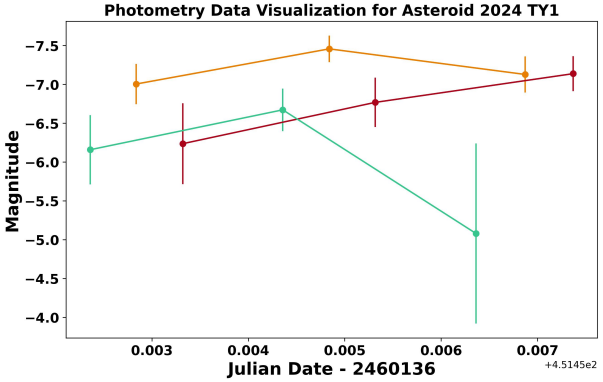
Photometry Data Visualization for Asteroid 2024 TY1
Magnitude
Julian Date - 2460136
+4.5145e2

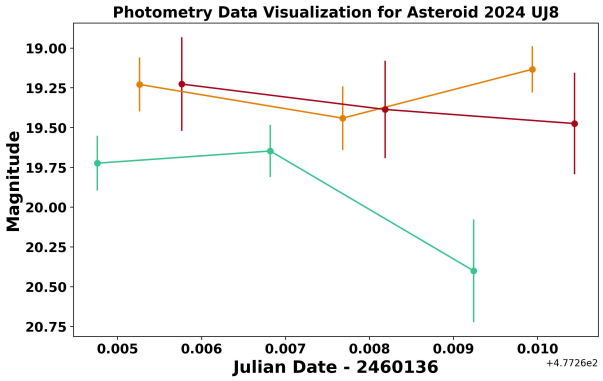
Photometry Data Visualization for Asteroid 2024 UJ8
Magnitude
Julian Date - 2460136
+4.7726e2

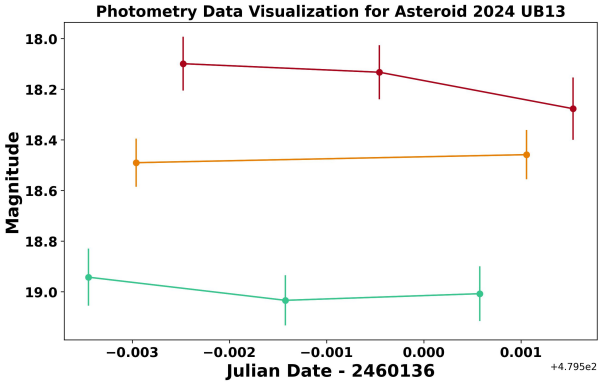
Photometry Data Visualization for Asteroid 2024 UB13
Magnitude
Julian Date - 2460136
+4.795e2

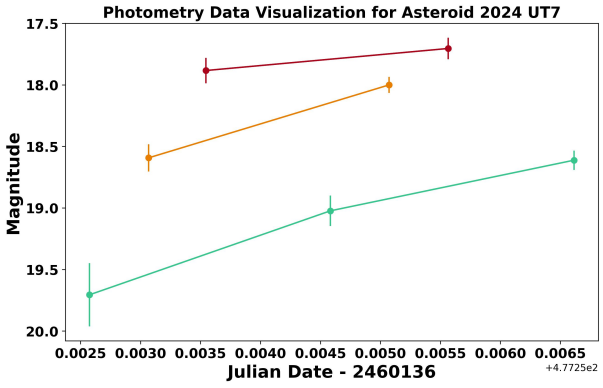
Photometry Data Visualization for Asteroid 2024 UT7
Magnitude
17.5
18.0
18.5
19.0
19.5
20.0
0.0025 0.0030 0.0035 0.0040 0.0045 0.0050 0.0055 0.0060 0.0065
Julian Date - 2460136
+4.7725e2

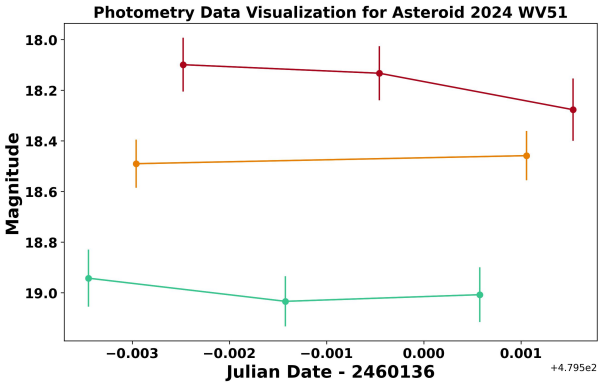
Photometry Data Visualization for Asteroid 2024 WV51
Magnitude
18.0
18.2
18.4
18.6
18.8
19.0
−0.003 −0.002 −0.001 0.000 0.001
Julian Date - 2460136
+4.795e2

B Appendix B: The Automated Script to Check for New Discoveries

```
import numpy as np
from astroplan import Observer
from astropy.time import Time,TimeDelta
from astropy.table import Table
from datetime import datetime,timedelta
import os
import requests
import json
import smtplib
from email.mime.text import MIMEText

import logging
logging.basicConfig(
    level=logging.INFO,
    format="%(asctime)s [%(levelname)s] %(message)s",
    handlers=[
        logging.FileHandler("LOG.log"),
        logging.StreamHandler()
    ]
)

##############################################
### OCS credentials and site information: ###
##############################################
SAAO_OCS_URL = 'http://10.1.100.96:8080/api/requestgroups/'
API_TOKEN = '93f84e6123c45917c735b6570490980beb415190'  # API
   token obtained from your profile page on the OCS website
PROPOSAL_ID = 'ATLAS_NEA_Ngwane_2024-1'  # Proposal ID
##############################################

def send_email(message):

    gmail_user = 'close.approach.alert@gmail.com'
    gmail_p = 'iypptywuqnrkmljy'

    fromx = gmail_user
    to  = ['nerasmus@saao.ac.za','thobekilesn@gmail.com']
    msg = MIMEText(message)
    msg['Subject'] = 'NEOCP follow-up request sent to SAAO OCS  '
```

```
39      msg['From'] = "SAAO IO NEOCP Alert"
40      msg['To'] = ", ".join(to)
41
42      try:
43          server = smtplib.SMTP('smtp.gmail.com:587')
44          server.starttls()
45          server.ehlo()
46          server.login(gmail_user, gmail_p)
47          server.sendmail(fromx, to, msg.as_string())
48          server.quit()
49
50          logging.info('Email sent!')
51      except Exception as err:
52          logging.error('Something went wrong with sending emails...
                ')
53          logging.error((Exception, err))
54
55  def send_observing_request_to_OCS(target,etime, duration,
        orbital_elements, start, end):
56
57      # window = 30 # minutes
58      # observation_duration = 10 #minutes
59      # Opening JSON template file
60      f = open('NEOCP_non_sidereal_template.json')
61      neocp_json = json.load(f)
62
63      ### make the changes for the specfic target ####
64      neocp_json['name'] = "NEOCP_"+target+"_follow_up_NS"
65      neocp_json['proposal'] = PROPOSAL_ID
66      neocp_json['requests'][0]["configurations"][0]['
           repeat_duration'] = str(duration)
67      neocp_json['requests'][0]["configurations"][0]['
           instrument_configs'][0]['exposure_time'] = "%0.0f"%(etime)
           # for clear filter
68      neocp_json['requests'][0]["configurations"][0]['
           instrument_configs'][1]['exposure_time'] = "%0.0f"%(etime)
           # for g-filter
69      neocp_json['requests'][0]["configurations"][0]['
           instrument_configs'][2]['exposure_time'] = "%0.0f"%(etime)
           # for r-filter
70      neocp_json['requests'][0]["configurations"][0]['
           instrument_configs'][3]['exposure_time'] = "%0.0f"%(etime)
           # for i-filter
```

```
71      neocp_json['requests'][0]["configurations"][0]['target']['name
            '] = target
72      neocp_json['requests'][0]["configurations"][0]['target']['
            orbinc'] = orbital_elements['orbinc']
73      neocp_json['requests'][0]["configurations"][0]['target']['
            longascnode'] = orbital_elements['longascnode']
74      neocp_json['requests'][0]["configurations"][0]['target']['
            argofperih'] = orbital_elements['argofperih']
75      neocp_json['requests'][0]["configurations"][0]['target']['
            eccentricity'] = orbital_elements['eccentricity']
76      neocp_json['requests'][0]["configurations"][0]['target']['
            meandist'] = orbital_elements['meandist']
77      neocp_json['requests'][0]["configurations"][0]['target']['
            meananom'] = orbital_elements['meananom']
78      neocp_json['requests'][0]["configurations"][0]['target']['
            epochofel'] = orbital_elements['epochofel']
79      neocp_json['requests'][0]['windows'][0]['start'] = str(start).
            replace('T',' ').split('.')[0] #current time, remove
            decimal seconds with split command
80      neocp_json['requests'][0]['windows'][0]['end'] =  str(end).
            replace('T',' ').split('.')[0] #next sunrise, remove
            decimal seconds with split command
81
82      # Submit the fully formed RequestGroup
83      response = requests.post(
84          SAAO_OCS_URL,
85          headers={'Authorization': 'Token {}'.format(API_TOKEN)},
86          json=neocp_json # Make sure you use json!
87      )
88
89      # Make sure the API call was successful
90      try:
91          response.raise_for_status()
92      except requests.exceptions.HTTPError as exc:
93          logging.error('API call failed: {}'.format(response.
                content))
94          raise exc
95
96      requestgroup_dict = response.json()  # The API will return the
            newly submitted requestgroup as json
97
98  def get_target_orbital_elements(target):
99
```

```
100     # request_url = "https://cgi.minorplanetcenter.net/cgi-bin/
            showobsorbs.cgi?Obj=A10UCLP&orb=y"
101     request_url = "https://cgi.minorplanetcenter.net/cgi-bin/
            showobsorbs.cgi?Obj="+target+"&orb=y"
102     logging.info(request_url)
103     r = requests.get(request_url)
104     return r.text
105 
106 def get_target_ephemeris(target,obs_code,start,stop,steps,fov,vmag
        ):
107 
108     # request_url = "https://ssd-api.jpl.nasa.gov/scout.api?tdes=
            A10IdnY&eph-start=2022-07-21T18:00:00&eph-stop=2022-07-21
            T18:30:00&eph-step=30m&fov-diam=10&fov-vmag=20.0&obs-code=
            M28"
109     request_url = "https://ssd-api.jpl.nasa.gov/scout.api?tdes="+
            target+"&eph-start="+str(start).split(".")[0]+"&eph-stop="+
            str(stop).split(".")[0]+"&eph-step="+steps+"&fov-diam="+"
            %0.0f"%(fov)+"&fov-vmag="+"%0.1f"%(vmag)+"&obs-code="+
            obs_code
110     logging.info(request_url)
111     r = requests.get(request_url)
112     return r
113 
114 def get_NEOCP_targets():
115 
116     request_url = "https://ssd-api.jpl.nasa.gov/scout.api"
117 
118     r = requests.get(request_url)
119     logging.info("Found "+str(r.json()['count'])+" potential
            targets")
120 
121     return r
122 
123 def unpack_date(packed_date):
124 
125     year_part1 = packed_date[0]
126     year_part2 = packed_date[1:3]
127     month_part = packed_date[3]
128     day_part = packed_date[4]
129 
130     ###### unpacking year ######
131     if year_part1 == 'I':
```

```
132         cent = '18'
133     elif year_part1 == 'J':
134         cent = '19'
135     elif year_part1 == 'K':
136         cent = '20'
137     else:
138         cent = 'XX'
139 
140     ###### unpacking month ######
141     if month_part ==  '1':
142         month = '01'
143     elif  month_part ==  '2':
144         month = '02'
145     elif  month_part ==  '3':
146         month = '03'
147     elif  month_part ==  '4':
148         month = '04'
149     elif  month_part ==  '5':
150         month = '05'
151     elif  month_part ==  '6':
152         month = '06'
153     elif  month_part ==  '7':
154         month = '07'
155     elif  month_part ==  '8':
156         month = '08'
157     elif  month_part ==  '9':
158         month = '09'
159     elif  month_part ==  'A':
160         month = '10'
161     elif  month_part ==  'B':
162         month = '11'
163     elif  month_part ==  'C':
164         month = '12'
165     else:
166         month = 'XX'
167 
168     ###### unpacking day ######
169     if day_part ==  '1':
170         day = '01'
171     elif  day_part ==  '2':
172         day = '02'
173     elif  day_part ==  '3':
174         day = '03'
```

```
175     elif  day_part ==  '4':
176         day = '04'
177     elif  day_part ==  '5':
178         day = '05'
179     elif  day_part ==  '6':
180         day = '06'
181     elif  day_part ==  '7':
182         day = '07'
183     elif  day_part ==  '8':
184         day = '08'
185     elif  day_part ==  '9':
186         day = '09'
187     elif  day_part ==  'A':
188         day = '10'
189     elif  day_part ==  'B':
190         day = '11'
191     elif  day_part ==  'C':
192         day = '12'
193     elif  day_part ==  'D':
194         day = '13'
195     elif  day_part ==  'E':
196         day = '14'
197     elif  day_part ==  'F':
198         day = '15'
199     elif  day_part ==  'G':
200         day = '16'
201     elif  day_part ==  'H':
202         day = '17'
203     elif  day_part ==  'I':
204         day = '18'
205     elif  day_part ==  'J':
206         day = '19'
207     elif  day_part ==  'K':
208         day = '20'
209     elif  day_part ==  'L':
210         day = '21'
211     elif  day_part ==  'M':
212         day = '22'
213     elif  day_part ==  'N':
214         day = '23'
215     elif  day_part ==  'O':
216         day = '24'
217     elif  day_part ==  'P':
```

```
218         day = '25'
219     elif  day_part ==  'Q':
220         day = '26'
221     elif  day_part ==  'R':
222         day = '27'
223     elif  day_part ==  'S':
224         day = '28'
225     elif  day_part ==  'T':
226         day = '29'
227     elif  day_part ==  'U':
228         day = '30'
229     elif  day_part ==  'V':
230         day = '31'
231     else:
232         day = 'XX'
233
234
235
236     #1999-01-01T00:00:00
237     return Time(cent+year_part2+'-'+month+'-'+day+'T00:00:00',
            format='isot')
238
239 #
240 def main():
241
242     logging.info(("\n----->>> Checking Scout now!\n"))
243
244     exp_time = 30 # for now we fix all follow-up to 30sec exposure
            in all filters, in future we may change strategy
245     duration = 600 # for now we fix expsore cycling to 10min, in
            future we may change strategy
246     # obs_code = 'M28' #for Lesedi
247     fov = 8 #arcmin FoV of imager
248     mag_limit = 18.7 # faintest magntude of object to attempt
            follow-up on
249     dec_limit = 25 # don't bother with objects with a dec further
            north than this
250     uncert_limit = fov # in arcmin, don't bother with objects that
            have a predicted co-ordinate uncertainty larger than this
251     # moon_limit = 30 # min distance to moon in deg
252     # fov_score_limit = 80 # JPL scout gives a probaly score of
            obejct being in FoV in percentage
```

```
253     # elevation_limit = 35 # minimun distance in deg of target
            from horizon to consider
254
255     done_targets = data = np.genfromtxt("done_targets.txt",
            delimiter='',skip_header=0,dtype=None, encoding='UTF-8',
            names =["name"])
256     time_now_utc = Time(str(datetime.utcnow()).replace(" ","T"),
            format='isot')
257     logging.info(("The UTC time now: "+str(time_now_utc)))
258     lesedi = Observer.at_site("Southern African Large Telescope")
259     sun_set = lesedi.sun_set_time(time_now_utc, which="nearest")
260     diff_time = (sun_set.mjd-time_now_utc.mjd)
261
262     # if True: #for testing at day
263     if diff_time < 0: # past sunset
264
265         start_date = time_now_utc
266         end_date = lesedi.sun_rise_time(time_now_utc, which="next"
                ).isot
267         # date_steps = '30m' #resolution of ephemeris
268
269         # check moon illumanation
270         lunar_illumination = lesedi.moon_illumination(start_date)
271         msg = "Lunar illumination = "+str(lunar_illumination)
272         # print(msg)
273         logging.info(msg)
274
275         if lunar_illumination<=0.1:
276             mag_limit = mag_limit+1 #chase after 1 mag fainter
                    stuff
277         elif lunar_illumination>0.1 and lunar_illumination<=0.5:
278             mag_limit = mag_limit+0.5 #chase after 0.5 mag fainter
                    stuff
279         else:
280             mag_limit = mag_limit
281
282         msg = "Limiting mag = "+str(mag_limit)
283         # print(msg)
284         logging.info(msg)
285
286         r = get_NEOCP_targets()
287
288         if int(r.json()['count']) > 0:
```

```
289             potential_targets =  np.array(r.json()['data'])
290
291             for target in potential_targets:
292                 logging.info("Found possible target: "+target['
                        objectName'])
293
294                 if target['objectName'] in done_targets['name']:
295                     logging.info("Nothing was done because a
                            follow-up request for this target has
                            already been sent before")
296                 else:
297
298                     if float(target['Vmag']) > mag_limit:
299                         logging.info("Nothing was done because
                                target is too faint")
300                         continue
301
302                     if float(target['dec']) > dec_limit:
303                         logging.info("Nothing was done because
                                target too far north")
304                         continue
305
306                     if float(target['unc']) > uncert_limit:
307                         logging.info("Nothing was done because
                                target position not known well enough
                                to be in Mookodi's FoV")
308                         continue
309
310                     # if target['objectName'][0:2] != 'A1':
311                     #     logging.info("Nothing was done because
                            target not ATLAS object, ignore for now")
312                     #     continue
313
314                     if target['objectName'][0:2] != 'A1' and
                            target['objectName'][0:1] != 'P' and target
                            ['objectName'][0:1] != 'C' and target['
                            objectName'][0:2] != 'ZT' and target['
                            objectName'][0:4] != 'xkos':
315                         logging.info("Nothing was done because
                                target not ATLAS/Pan-STARRS/Catalina/
                                ZTF or xkos object, ignore for now")
316                         continue
317
```

```
318
319                 logging.info("Target is potentially observable
                        , gathering object ephemeris")
320
321                 orbital_elements = get_target_orbital_elements
                        (target = target['objectName'])
322                 #print(orbital_elements)
323                 text_file = open("orb_elem.txt", "w")
324                 text_file.write(orbital_elements.split('</pre>
                        ')[0].split('<pre>')[-1])
325                 text_file.close()
326
327                 orbital_elements_array = np.genfromtxt("
                        orb_elem.txt", skip_header = 2,delimiter=''
                        ,dtype=None,encoding='UTF-8',names = ['
                        Object', 'H', 'G','Epoch','M','Peri','Node'
                        ,'Incl','e','n','a','NObs','NOpp','Arc','
                        Arcunit','rms','Orbit_ID'])
328                 epoch = orbital_elements_array['Epoch'][0]
329                 unpacked_epoch = str(unpack_date(epoch).mjd)
330                 print(unpacked_epoch)
331
332                 # ocs_orbital_elements = {    "orbinc": np.
                        median(orbital_elements_array['Incl']),
333                 #                 \\              "longascnode":
                         np.median(orbital_elements_array['Node']),
334                 #                 \\              "argofperih":
                        np.median(orbital_elements_array['Peri']),
335                 #                 \\              "eccentricity
                        ": np.median(orbital_elements_array['e']),
336                 #                 \\              "meandist": np
                        .median(orbital_elements_array['a']),
337                 #                 \\              "meananom":
                        np.median(orbital_elements_array['M']),
338                 #                 \\              "epochofel":
                        unpacked_epoch}
339                 ### --> need to take the first element in the
                        table because that is the "nominal"
                        parameters
340
341                 ocs_orbital_elements = {    "orbinc":
                        orbital_elements_array['Incl'][0],
```

```
342                                     \\              "longascnode":
                                           orbital_elements_array['Node'
                                           ][0],
343                                     \\              "argofperih":
                                           orbital_elements_array['Peri'
                                           ][0],
344                                     \\              "eccentricity":
                                           orbital_elements_array['e'
                                           ][0],
345                                     \\              "meandist":
                                           orbital_elements_array['a'
                                           ][0],
346                                     \\              "meananom":
                                           orbital_elements_array['M'
                                           ][0],
347                                     \\              "epochofel":
                                           unpacked_epoch}
348
349                             logging.info("Sending an observation request
                                   to the OCS...")
350                             try:
351                                 send_observing_request_to_OCS(target=
                                       target['objectName'],etime=exp_time,
                                       duration=duration,orbital_elements=
                                       ocs_orbital_elements,start=start_date,
                                       end=end_date)
352                                 logging.info("Request sent successfully,
                                       adding target to done list")
353
354                                 ### at the end we add it to "done targets"
355                                 f = open(os.getcwd()+"/done_targets.txt",
                                       "a")
356                                 f.write(target['objectName']+"\n")
357                                 f.close()
358
359                                 send_email(target['objectName'])
360                             except Exception as err:
361                                 logging.error("Something went wrong with
                                       request to OCS")
362                                 logging.error(Exception, err)
363 #
364
365         else:
```

```
366                 logging.info("No targets on the Scout page")
367
368
369         else:
370             logging.info("Nothing was done because it is not after
                sunset yet")
371
372
373 if __name__ == "__main__":
374     main()
```

C Appendix C: Mookodi Extract Manual MPC Astrometry Script

```
    import matplotlib.pyplot as plt
import numpy as np
from astropy import units as u
from astropy.wcs import WCS
from astroquery.gaia import Gaia
import os
import glob
import time
from astropy.time import Time, TimeDelta
from astropy.io import fits
from astropy.coordinates import SkyCoord
import astropy.visualization
zscaler = astropy.visualization.ZScaleInterval()
import sep
from photutils.aperture import CircularAperture
import sys
import argparse
import paramiko
from scipy.optimize import curve_fit


def linear_func(x,x0,m,c):
    return m*(x-x0)+c

def get_calibrated_mag_function_param(central_coords,wcs,
   all_sources_table,all_sources_flux,all_sources_fluxerr):

    good_star_ind = np.where((all_sources_table['peak']>2000) & (
       all_sources_table['peak']<40000))
    all_sources_table = all_sources_table[good_star_ind]
    all_sources_flux = all_sources_flux[good_star_ind]
    all_sources_fluxerr = all_sources_fluxerr[good_star_ind]

    ax2 = plt.subplot2grid((1,2), (0,1),rowspan=1, colspan=1)
    ax2.clear()
    coord = SkyCoord(ra=central_coords.ra.deg, dec=central_coords.
       dec.deg, unit=(u.degree, u.degree), frame='icrs')
    print("Central RA and DEC of image: ",coord)
    width = u.Quantity(0.166667, u.deg)#10 arcmin in degrees
```

```
    height = u.Quantity(0.166667, u.deg)#10 arcmin in degrees
    print("RA and DEC range observing window: ",width,height)

    ### get star that fall in entire observing window
    Gaia.ROW_LIMIT = -1
    r = Gaia.query_object_async(coordinate=coord, width=width,
       height=height)
    star_info = np.rec.fromarrays([ r['SOURCE_ID'].data,
                                    r['ra'].data,
                                    r['dec'].data,
                                    r['phot_g_mean_mag'].data,
                                    r['phot_variable_flag'].data],
                                    dtype=None,names=['SOURCE_ID','
                                       ra','dec','phot_g_mean_mag',
                                       'phot_variable_flag'])

    print("Number of stars covered by observing window: ", len(
       star_info))

    GAIA_star_coords = SkyCoord(ra=star_info['ra'], dec=star_info[
       'dec'], unit=(u.degree, u.degree), frame='icrs')
    GAIA_x_px, GAIA_y_px = wcs.world_to_pixel(GAIA_star_coords)
    # print(GAIA_x_px, GAIA_y_px )
    instrument_mags = []
    instrument_mags_err = []
    match_mags = []
    for s,source in enumerate(all_sources_table):
        source_x = source['x']
        source_y = source['y']
        # print(source_x,source_y)

        x_dif = GAIA_x_px-source_x
        y_dif = GAIA_y_px-source_y
        r_dif = np.sqrt(np.power(x_dif,2)+np.power(y_dif,2))

        closest_source_ind =np.argmin(r_dif)

        if r_dif[closest_source_ind] <= 3: # detected source and
           GAIA source have to be within 2 pixels of each other
            # print(star_info[closest_source_ind])
            instrument_mag = -2.5*np.log10(all_sources_flux[s])
            instrument_mag_lower = -2.5*np.log10(all_sources_flux[
               s]-all_sources_fluxerr[s])
```

```
73              instrument_mag_upper = -2.5*np.log10(all_sources_flux[
                    s]+all_sources_fluxerr[s])
74
75              instrument_mags.append(instrument_mag)
76              instrument_mags_err.append(np.abs(instrument_mag_lower
                    -instrument_mag_upper))
77              match_mags.append(star_info[closest_source_ind]['
                    phot_g_mean_mag'])
78
79      instrument_mags = np.array(instrument_mags)
80      instrument_mags_err = np.array(instrument_mags_err)
81      match_mags =  np.array(match_mags)
82
83      #### plot and do a prelimanry linear fit####
84      ax2.errorbar(instrument_mags, match_mags, yerr=np.abs(
            instrument_mags_err), label = 'outliers', markersize=2,
            alpha=0.7, marker='o',color='b',markeredgecolor='none',
            linestyle='',capsize=3,elinewidth=0.5,capthick=0.5)
85      popt, pcov = curve_fit(f=linear_func, xdata=instrument_mags,
            ydata=match_mags)
86      fit_x = np.linspace(np.min(instrument_mags), np.max(
            instrument_mags),1000)
87      fit_y =  linear_func(fit_x,*popt)
88      ax2.plot(fit_x,fit_y,c='k', linestyle='-.',linewidth=2,zorder
            =100,label = "prelim. linear fit with outliers")
89
90      ### remove outliers from preliminary fit and redo fit #####
91      residuals = match_mags-linear_func(instrument_mags,*popt)
92      clean_ind = np.where(np.abs(residuals)<1)# accept data where
            resdiuals less than 1 mag for preliminary fit
93      instrument_mags_clean = instrument_mags[clean_ind]
94      match_mags_clean = match_mags[clean_ind]
95      instrument_mags_err_clean = instrument_mags_err[clean_ind]
96
97      ax2.errorbar(instrument_mags_clean, match_mags_clean, yerr=np.
            abs(instrument_mags_err_clean), markersize=4, alpha=1,
            marker='o',color='b',markeredgecolor='none',linestyle='',
            capsize=3,elinewidth=0.5,capthick=0.5)
98      popt, pcov = curve_fit(f=linear_func, xdata=
            instrument_mags_clean, ydata=match_mags_clean)
99      fit_x = np.linspace(np.min(instrument_mags_clean), np.max(
            instrument_mags_clean),1000)
100     fit_y =  linear_func(fit_x,*popt)
```

```
101     ax2.plot(fit_x,fit_y,c='k', linestyle='-',linewidth=2,zorder
            =100,label = "final linear fit after removing outliers")
102
103
104
105     ax2.set_xlabel('instrument mag')
106     ax2.set_ylabel('gaia G mag')
107     ax2.legend()
108     # plt.show()
109
110
111     return popt
112
113 def create_MPC_header(write_file):
114
115     write_file.write('COD M28\n')
116     write_file.write('CON N. Erasmus, 1 Observatory Road, Cape
            Town, South Africa\n')
117     write_file.write('OBS N. Erasmus, S. Potter, C. van Gend, S.
            Chandra, H. Worters\n')
118     write_file.write('MEA T. Ngwane, N. Erasmus\n')
119     write_file.write('TEL 1.0-m f/8 Reflector + CCD\n')
120     write_file.write('NET Gaia-DR2\n')
121     write_file.write('AC2 nerasmus@saao.ac.za, thobekilesn@gmail.
            com\n')
122     write_file.write('ACK NEOCP\n')
123     write_file.write('\n')
124
125 def main():
126
127     global fig
128
129     parser = argparse.ArgumentParser("Usage: python
            mookodi_extract_manual_mpc_astrometry.py --file_dir /path/
            to/files/")
130     parser.add_argument('--file_dir', type=str, default='./files',
             action='store', help="path to files")
131     parser.add_argument('--snr', type=str, default='1.1', action='
            store', help="threshold for source detection")
132
133
134     args = parser.parse_args()
135     path = args.file_dir
```

```
136     snr = float(args.snr)
137 
138     ### astrometry.net on IOserver ####
139     host = "     "
140     username = '     '
141     passw = ' '
142 
143     # #### astrometry.net on old astrometry.net server ####
144     #host = "     "
145     #username = '    '
146     #passw = '       '
147 
148     search_radius =  0.5 #in degrees
149     scale_low  = 0.13 #8 arcmin in degrees
150     scale_high  = 0.18 #11 arcmin in degrees
151 
152 
153     MPC_file = open(path+"/MPC_submission.txt",'w')
154     create_MPC_header(MPC_file)
155 
156     file_path_list = sorted(glob.glob(path+"/MKD*.fits"))
157     file_path_list = file_path_list
158 
159     fig = plt.figure()
160     fig.set_size_inches(10, 6)
161     ax1 = plt.subplot2grid((1,2), (0,0),rowspan=1, colspan=1)
162 
163 
164     for i,file_path in enumerate(file_path_list):
165         fits_file = file_path.split('/')[-1]
166         print(fits_file)
167         ax1.clear()
168         ########################################################
169         #### check time diffrence between adjacent images ####
170         ########################################################
171         hdu1 = fits.open(file_path)
172 
173         ############################################################
174         ### extract sources from image and save as .xyls file ###
175         ############################################################
176         data = hdu1[0].data.astype(float)#.byteswap(inplace=True).
               newbyteorder()
```

```
177         ax1.imshow(data,cmap='gray',vmin=zscaler.get_limits(data)
                [0],vmax=zscaler.get_limits(data)[1])
178         ax1.invert_yaxis()
179
180         bkg = sep.Background(data)
181
182         data_sub = data - bkg
183         radius = 4
184         sources = sep.extract(data_sub, thresh=snr, minarea=(np.pi
                *radius**2)/10, err=bkg.globalrms)
185         ax1.scatter(sources['x'],sources['y'],marker='.', c='#65
                fe08')
186         flux, fluxerr, flag = sep.sum_circle(data_sub, x = sources
                ['x'], y = sources['y'],r = radius, err=bkg.globalrms,
                gain=1.0)
187
188         source_aperture = CircularAperture(zip(sources['x'],
                sources['y']), r=radius)
189         source_aperture.plot(color='blue', lw=1, alpha=0.5, label=
                'detected sources, used for astrom. callib.')
190
191         col1 = fits.Column(name='x', format='1E', array=sources['x
                ']+1) #need to add +1 becasue of the 0 vs. 1 base for
                image origin pixel between astrometry.net and imshow
192         col2 = fits.Column(name='y', format='1E', array=sources['y
                ']+1) #need to add +1 becasue of the 0 vs. 1 base for
                image origin pixel between astrometry.net and imshow
193         col3 = fits.Column(name='flux', format='1E', array=sources
                ['flux'])
194
195         coldefs = fits.ColDefs([col1, col2, col3])
196         source_hdu = fits.BinTableHDU.from_columns(coldefs)
197         source_hdu.writeto(file_path.replace('.fits','.xyls'),
                output_verify='silentfix',overwrite=True)
198         # plt.savefig(file_path.replace('.fits','.png'), format='
                png',dpi=150)
199         ##########################################################
200
201
202         ##########################################
203         ### do wcs on each image via astrometry.net SAAO server
                and copy solution back to local machine #####
204         ##########################################
```

```
205
206         try:
207             ra = hdu1[0].header['RA']
208             dec = hdu1[0].header['DEC']
209         except Exception as e:
210             print('RA or DEC header keyword may be missing, see
                    detail below. Delete/Repair specific file and try
                    again.')
211             print(sys.stderr, "Exception: %s" % str(e))
212             sys.exit(1)
213             # print('Trying TARG_RA and TARG_DEC keywords')
214             # ra = hdu1[0].header['TARG_RA']
215             # dec = hdu1[0].header['TARG_DEC']
216
217         telescope_coords = SkyCoord(ra, dec,unit=(u.hourangle, u.
                deg))
218         ra_in_deg = telescope_coords.to_string().split()[0]
219         dec_in_deg = telescope_coords.to_string().split()[1]
220
221         image_size_x = hdu1[0].header['NAXIS1']
222         image_size_y = hdu1[0].header['NAXIS2']
223         # print(image_size_x,image_size_y)
224         # print(data.shape)
225
226         target = hdu1[0].header['OBJECT']
227
228         exp_time = hdu1[0].header['EXPTIME']
229
230         sdds_filter = hdu1[0].header['FILTERA'].strip()
231         spec_filter = hdu1[0].header['FILTERB'].strip()
232         if sdds_filter == "out" and spec_filter == "clear":
233             sdds_filter = "G"
234
235         t = Time(float(hdu1[0].header['MJD']) , format='mjd')
236         t_mid_exposure = t+TimeDelta(float(exp_time)/2/24/60/60,
                format='jd')
237         date = str(t_mid_exposure.iso).split()[0].split('-')
238         year = date[0]
239         month =  date[1]
240         day =  date[2]
241         day_fract = ('%.5f' % float(t_mid_exposure.mjd)).split('.'
                )[-1]
242
```

```
243         ######################################
244         ### create ssh/ftp client and conenct ###
245         ######################################
246         ssh_client = paramiko.client.SSHClient()
247         ssh_client.set_missing_host_key_policy(paramiko.
               AutoAddPolicy())
248         ssh_client.connect(host, username=username, password=passw
               )
249         ftp_client=ssh_client.open_sftp()
250 
251         try: #### copy xyls accross ######
252             print('Copying xyls (source list) to local Astrometry.
                   net server...')
253             ftp_client.put(file_path.replace('.fits','.xyls'),'/
                   tmp/'+fits_file.replace('.fits','.xyls'))
254             print('Source list copied across.')
255         except Exception as e:
256             print('Could not copy source list to local Astrometry.
                   net server. Exiting.')
257             print(sys.stderr, "Exception: %s" % str(e))
258             sys.exit(1)
259 
260         try:#### astrometry.net command on server and write
               results to wcs_info.txt:
261             astr_command = '/usr/local/astrometry/bin/solve-field
                   --overwrite \
262                                             \\                    --
                                                crpix-center \
263                                             \\                    --
                                                tweak-order 0 \
264                                             \\                    --
                                                scale-units degwidth
                                                 \
265                                             \\                    --
                                                scale-low '+str(
                                                scale_low)+' \
266                                             \\                    --
                                                scale-high '+str(
                                                scale_high)+' \
267                                             \\                    --
                                                ra '+str(ra_in_deg)+
                                                ' --dec '+str(
                                                dec_in_deg)+' \
```

```
268                                                 \\                  --
                                                       radius '+str(
                                                       search_radius)+' \
269                                                 \\                  --x
                                                       -column x --y-column
                                                        y --sort-column
                                                       flux \
270                                                 \\                  --
                                                       width '+str(
                                                       image_size_x)+' --
                                                       height '+str(
                                                       image_size_y)+' \
271                                                 \\                  --
                                                       no-plots  --new-fits
                                                        none /tmp/'+
                                                       fits_file.replace('.
                                                       fits','.xyls'+\
272                                                 \\                  ' >
                                                        '+fits_file.replace
                                                       ('.fits','_wcs_info.
                                                       txt'))
273             print('Running astrometry.net command on source list
                    ...')
274             # print(astr_command.strip('\n'))
275             stdin, stdout, stderr = ssh_client.exec_command(
                    astr_command)
276             time.sleep(3) # just sleep a bit wait for files to be
                    created by astrometry.net before tryong to copy in
                    next step
277             print('Writing solution to wcs_info.txt')
278         except Exception as e:
279             print('Could not run astrometry.net on server. Exiting
                    .')
280             print(sys.stderr, "Exception: %s" % str(e))
281             sys.exit(1)
282
283         try: #### copy wcs header back ######
284             print('Copying wcs header back to your machine...')
285             ftp_client.get('/tmp/'+fits_file.replace('.fits','.wcs
                    '), file_path.replace('.fits','.wcs'))
286             print('WCS header copied across.')
287         except Exception as e:
```

```
288             print('Could not copy wcs header from local Astrometry
                    .net server. Exiting.')
289             print(sys.stderr, "Exception: %s" % str(e))
290             sys.exit(1)
291 
292         ssh_client.close()
293         ftp_client.close()
294 
295         wcs_hdu = fits.open(file_path.replace('.fits','.wcs'))
296         wcs_header = wcs_hdu[0].header
297         w = WCS(wcs_header)
298 
299         central_coords = w.pixel_to_world(image_size_x/2,
                image_size_x/2)
300         param = get_calibrated_mag_function_param(central_coords,w
                ,sources,flux, fluxerr)
301         plt.savefig(file_path.replace('.fits','.png'), format='png
                ',dpi=150)
302 
303         print("\n 1. Zoom to desired location.\n 2. Hover over
                location with mouse and hit spacebar, then click to
                display selected location.\n 3. Repeat above steps to
                reselect new location.\n 4. Hit enter and the last
                selected point will be saved.\n")
304         # click = fig.ginput(1, timeout=0, show_clicks=False)
305         click = fig.ginput(n=0, timeout=0, mouse_add=None,
                mouse_pop=None, mouse_stop=None)
306         click_x = click[-1][0]
307         click_y = click[-1][1]
308         # plt.savefig(file_path.replace('.fits','.png'), format='
                png',dpi=150)
309         x_dif = sources['x']-click_x
310         y_dif = sources['y']-click_y
311         r_dif = np.sqrt(np.power(x_dif,2)+np.power(y_dif,2))
312         closest_source_ind =np.argmin(r_dif)
313 
314         if r_dif[closest_source_ind] < 2: #pixels
315             print("grabbing closest detected source")
316             closest_source_x = sources['x'][closest_source_ind]
317             closest_source_y = sources['y'][closest_source_ind]
318         else: # use clicked location
319             print("closest detected source too far away, grabbing
                    clicked location")
```

```
320             closest_source_x =  click_x
321             closest_source_y =  click_y
322
323         selected_coords = w.pixel_to_world(closest_source_x,
               closest_source_y) # with SIP and distortion paper table
                lookup correction being applied
324         MPC_ra_format =  selected_coords.ra.to_string(unit=u.
               hourangle,sep=' ',pad=True,precision=2)
325         MPC_dec_format =  selected_coords.dec.to_string(unit=u.deg
               ,sep=' ',alwayssign=True,pad=True,precision=1)
326         print("Coordinates selected: ",MPC_ra_format,
               MPC_dec_format)
327
328         # selected_coords = w.wcs_pix2world(closest_source_x,
               closest_source_y,0) #doing only the basic wcslib
               transformation <--- can do this to by adding --no-tweak
                to astrometry.net command
329         # selected_coords = SkyCoord(ra=selected_coords[0], dec=
               selected_coords[1], unit=(u.degree, u.degree), frame='
               icrs')
330         # MPC_ra_format =  selected_coords.ra.to_string(unit=u.
               hourangle,sep=' ',pad=True,precision=2)
331         # MPC_dec_format =  selected_coords.dec.to_string(unit=u.
               deg,sep=' ',alwayssign=True,pad=True,precision=1)
332         # print("Coordinates selected: ",MPC_ra_format,
               MPC_dec_format)
333
334         selected_flux, selected_fluxerr, selected_flag = sep.
               sum_circle(data_sub, x = [closest_source_x], y = [
               closest_source_y],r = radius, err=bkg.globalrms, gain
               =1.0)
335
336         if sdds_filter == 'G':
337             selected_inst_mag = -2.5*np.log10(selected_flux)
338             cal_mag  =  linear_func(selected_inst_mag,*param)
339             selected_source_mag = '%.1f' % cal_mag
340         else:
341             selected_source_mag = '    ' # for now we only have
                   GAIA G-mags so can't callibrate for anything but
                   clear
342
343
```

```
344         # MPC_file.write('     '+target + '  '+'C'+year+' '+month
               +' '+day+'.'+day_fract+' '+MPC_ra_format+' '+
               MPC_dec_format+'             '+'   '+' '+sdds_filter+'
                    M28'+'\n')
345         MPC_file.write('  '+target + '  '+'C'+year+' '+month+' '+
               day+'.'+day_fract+' '+MPC_ra_format+' '+MPC_dec_format+
               '            '+selected_source_mag+' '+sdds_filter+'
                    M28'+'\n')
346
347
348 if __name__ == "__main__": main()
```

D Appendix D: Mookodi Reduction Script

```
    import matplotlib.pyplot as plt
import numpy as np
import os
import glob
from astropy.io import fits
import astropy.visualization
zscaler = astropy.visualization.ZScaleInterval()
import argparse


# read command line arguments
parser = argparse.ArgumentParser(prog="mookodi_photometry_reduction.py",
                                 description="-----------------
                                    Bias and Flat field reduction
                                    for Mookodi imaging data
                                    -----------------",
                                 epilog="
                                    Tmookodi_photometry_reduction.
                                    py \n"
                                        "Copyright (C) 2022 \n"
                                        "(N. Erasmus - SAAO). \n"
                                        "This program comes with
                                           ABSOLUTELY NO WARRANTY.
                                            \n"
                                        "This is free software and
                                            you are welcome to use
                                           , modify and
                                           redistribute it. \n")

#Usage: python mookodi_photometry_reduction.py --image_dir /home/Desktop/29June/Didymos --bias_dir /home/Desktop/29June/bias_frames/2x2/ --flat_dir /home/Desktop/flat_frames/2x2_r/
parser.add_argument('--image_dir', type=str, default='./science', action='store', help="Directory path of where science file(s) are located; <str>")
parser.add_argument('--bias_dir', type=str, default='./bias', action='store', help="Directory path of where bias file(s) are located; <str>")
parser.add_argument('--flat_dir', type=str, default='./flat', action='store', help="Directory path of where flat file(s) are
```

```
    located; <str>")
24
25 args = parser.parse_args()
26
27 # path = os.getcwd()+"/30June/"
28
29 data_file_path_list = sorted(glob.glob(args.image_dir+"/MKD_*.fits
       "))
30 bias_file_path_list = sorted(glob.glob(args.bias_dir+"/MKD_*.fits"
       ))
31 flat_file_path_list = sorted(glob.glob(args.flat_dir+"/MKD_*.fits"
       ))
32
33
34 fig = plt.figure()
35 fig.set_size_inches(5, 5)
36
37 ############################
38 #### create master bias ####
39 ############################
40 if bias_file_path_list == []:
41      print("no fits files in given bias folder")
42 else:
43     print("Found {} fits files in given bias folder".format(len(
          bias_file_path_list)))
44     bias_stack = []
45     for i in range(len(bias_file_path_list)):
46         fits_file = bias_file_path_list[i].split('/')[-1]
47         hdu1 = fits.open(bias_file_path_list[i])
48         data = hdu1[0].data
49         bias_stack.append(data)
50
51     master_bias = np.median(bias_stack,axis=0)
52     plt.imshow(master_bias,cmap='gray',vmin=zscaler.get_limits(
          master_bias)[0],vmax=zscaler.get_limits(master_bias)[1])
53     plt.show()
54     plt.clf()
55
56 ############################
57 #### create master flat ####
58 ############################
59 if flat_file_path_list == []:
60      print("no fits files in given flat folder")
```

```
61 else:
62     print("Found {} fits files in given flat folder".format(len(
          flat_file_path_list)))
63     flat_stack = []
64     for i in range(len(flat_file_path_list)):
65         fits_file = flat_file_path_list[i].split('/')[-1]
66         hdu1 = fits.open(flat_file_path_list[i])
67         data = hdu1[0].data
68         flat_stack.append(data-master_bias)
69 
70     master_flat = np.median(flat_stack,axis=0)
71     master_flat = master_flat/np.max(np.max(master_flat))
72     plt.imshow(master_flat,cmap='gray',vmin=zscaler.get_limits(
          master_flat)[0],vmax=zscaler.get_limits(master_flat)[1])
73     plt.show()
74     plt.clf()
75 
76 ############################
77 #### reduce science data ####
78 ############################ #
79 if data_file_path_list == []:
80      print("no fits files in given data folder")
81 else:
82     print("Found {} fits files in given data folder".format(len(
          data_file_path_list)))
83     for i in range(len(data_file_path_list)):
84         fits_file = data_file_path_list[i].split('/')[-1]
85         hdu1 = fits.open(data_file_path_list[i])
86         inst_sky_angle = float(hdu1[0].header['ROTANGLE'])-float(
              hdu1[0].header['ROTSKYPA'])
87         data = hdu1[0].data
88         reduced_data = np.divide((data-master_bias),master_flat)
89         reduced_data[reduced_data < 0] = 0
90         reduced_data[reduced_data > 2**16] = 2**16-1
91 
92         #if round(inst_sky_angle) == 0 or round(inst_sky_angle) ==
              -360:
93         #    final_data_hdu = fits.PrimaryHDU(np.fliplr(np.flipud(
             np.uint16(reduced_data))))  #rotate image by 180 deg
94         #elif round(abs(inst_sky_angle)) == 180:
95             #final_data_hdu = fits.PrimaryHDU(np.uint16(
                 reduced_data))
96         #else:
```

```
97              #print("---->>> Irregular sky angle of {}. So not
                   doing anything to rotation but field identification
                    might be tricky so beware!!!.".format(round(
                   inst_sky_angle)))
98          final_data_hdu = fits.PrimaryHDU(np.uint16(reduced_data))
               #rotate image by 180deg
99
100         final_data_hdu.header = hdu1[0].header
101
102         destination_path = data_file_path_list[i].replace("MKD","/
               red/MKDred")
103         folder = os.path.dirname(destination_path)
104         if not os.path.exists(folder): # if directory doesn't
               exist create it
105            os.makedirs(folder)
106
107         final_data_hdu.writeto(destination_path, output_verify='
               silentfix',overwrite=True)
```